Broadband emission processes of Active Galactic Nuclei

Master's Thesis in Physics
Presented by

Andrea Gokus

22.09.2017

Dr. Karl Remeis-Sternwarte Bamberg
Friedrich-Alexander-Universität Erlangen-Nürnberg

Betreuer: Prof. Dr. Jörn Wilms

Abstract

In my Master's Thesis I present two topics related to Active Galactic Nuclei (AGN). These objects are very luminous and emit across the whole electromagnetic spectrum. Radio-loud AGN feature jets, very long and collimated streams of matter, which are observable in all wavelengths as well. The visibility in the radio band is due to synchrotron radiation emitted by electrons. This emission process is the first main topic of this thesis and addressed in detail, covering the complete derivation from the Maxwell equations to the final, self-absorbed spectrum produced by electrons, which follow an energy dependent power-law distribution. As synchrotron radiation is discussed in many publications, but the equations do not always look the same at first sight, an elaborated comparison is conducted.

Numerical methods are necessary for the calculation of a spectrum if the electron distribution does not allow an analytical approximation for the radiation. For power-law distributed electrons one can either determine a numerical or an analytical solution, which is why I use a numeric integrator for the calculation of the spectra first and then compare the results with the analytic approximation of the integrals. Additionally I show problems, which arise from using numeric methods.

The second main topic of this work presents a systematic cross-correlation study of two X-ray satellites, *XMM-Newton* and *NuSTAR*. A good cross-calibration between different instruments is essential for multiwavelength observations, which help understanding astrophysical sources due to analyses in the complete spectral range. For the study, simultaneous observations of AGN are analysed using two different methods. The comparison of the photon indices, which describe the slope of the power-law, allows to detect differences in the calibration of both instruments. By simultaneously fitting both spectra in the overlapping energy band, one can determine the difference in the flux normalisation.

Zusammenfassung

In meiner Masterarbeit stelle ich zwei Themen vor, die beide im Zusammenhang mit Aktiven Galaxienkernen (AGN) stehen. AGNs sind sehr leuchtkräftige Objekte und emittieren Strahlung im gesamten elektromagnetischen Spektrum. Radio-laute AGNs besitzen sehr lange, kollimierte Materie-Ausströmungen, sogenannte Jets, die in allen Wellenlängen beobachtbar sind. Für die Emission im Radiobereich ist die, von Elektronen abgestrahlte, Synchrotronstrahlung verantwortlich. Dieser Strahlung gehe ich im ersten Teil der Arbeit auf den Grund und zeige, wie man von den Maxwell-Gleichungen zu einem selbstabsorbierten Synchrotronspektrum kommt, welches von Elektronen erzeugt wird, deren Energieverteilung einem Potenzgesetz entspricht. Da Synchrotronstrahlung zu den Grundlagen der Astrophysik gehört, wird sie in vielen Büchern diskutiert, jedoch sehen die Gleichungen auf den ersten Blick nicht immer gleich aus. Daher vergleiche ich die Formeln von vier unterschiedlichen Autoren.

Numerische Methoden sind nötig, wenn die Strahlung einer bestimmten Elektronenverteilung nicht analytisch bestimmt werden kann. Die Synchrotronstrahlung einer Verteilung der Elektronenenergie nach einem Potenzgesetz kann man sowohl numerisch als auch analytisch berechnen. Daher verwende ich für die Berechnung der Spektren erst einen numerischen Integrator und vergleiche dann das Ergebnis mit der analytischen Näherung der Formel. Zusätzlich zeige ich Probleme auf, die bei der Benutzung von numerischen Methoden auftreten.

Das zweite Thema dieser Arbeit behandelt die systematische Untersuchung der Kreuzkorrelation der beiden Röntgensatelliten *XMM-Newton* und *NuSTAR*. Eine möglichst gute Kreuzkorrelation zwischen den Beobachtungsinstrumenten ist unumgänglich für Multiwellenlängen-Kampagnen, mit deren Hilfe man astrophysikalische Objekte in allen Spektralbereichen analysieren und dadurch besser verstehen kann. Für die Analyse werden zwei unterschiedliche Methoden verwendet. Dabei werden die Photon Indizes, die die Steigung des unterliegenden Potenzgesetzes im Spektrum beschreiben, verglichen, damit man Unterschiede in der Kalibration beider Satelliten bestimmen kann. Desweiteren kann der Unterschied in der Fluss-Normalisierung bestimmt werden, indem man Spektren beider Satelliten im überlappenden Energieband fittet.

Contents

1 Active Galactic Nuclei 1
1.1 Historical overview . . . 1
1.2 The AGN zoo . . . 2
1.2.1 Radio-quiet AGN . . . 2
1.2.2 Radio-loud AGN . . . 4
1.3 The physics of AGN . . . 5
1.3.1 Unification paradigm for AGN . . . 5
1.3.2 Accretion . . . 7
1.3.3 Jets . . . 7
1.3.4 Radiative processes . . . 8

2 Theory of synchrotron radiation 11
2.1 Electromagnetic field of an accelerated charge . . . 11
2.2 Motion of a charged particle in a magnetic field . . . 13
2.3 Spectral distribution of synchrotron radiation of a single electron . . . 15
2.4 Radiation from an Ensemble of Electrons . . . 21
2.4.1 Emission coefficient . . . 21
2.4.2 Absorption coefficient . . . 23
2.4.3 Radiative transfer . . . 25
2.4.4 Concrete equations for a specific distribution . . . 25
2.5 Comparison with other formulae . . . 29
2.5.1 Emission coefficient formulae . . . 29
2.5.2 Absorption coefficient formulae . . . 32
2.5.3 Conclusions . . . 33

3 Numerical integration problems 35
3.1 Integration limits . . . 35
3.2 Difference between analytical and numerical solution . . . 36
3.3 Integration over distributed energy spectra . . . 36
3.4 Intensity spectrum . . . 37
3.5 Other integrators . . . 38

4 Systematic study of simultaneous observations of AGN by *XMM-Newton* and *NuSTAR* 39
4.1 Introduction . . . 39
4.2 The satellites *XMM-Newton* and *NuSTAR* . . . 39
4.3 Data . . . 40
4.3.1 Extraction . . . 40
4.3.2 Data Analysis . . . 41
4.4 Comparison with other studies . . . 50

4.5 Outlook 51

5 Summary 53

References 55

Acknowledgements 61

Chapter 1

Active Galactic Nuclei

Not long ago, in 1920, astronomers were having a dispute about the size of our universe. Harlow Shapley was of the opinion that nebulae, e.g. the Andromeda nebula, are located close to our own galaxy, the Milky Way, while Heber Curtis believed they are galaxies of their own. This Great Debate (also called Shapley-Curtis Debate) was a milestone for Astronomy. Due to the period-luminosity relationship for Cepheids found by Leavitt & Pickering (1912), it was possible to use variable Cepheid stars as standard candles to measure distances in the universe. Curtis was proven right after Hubble (1926) used Cepheids to measure distances to several nebulae and found them being too distant to belong to our galaxy.

Since then, many extragalactic sources have been discovered, one of them being active galaxies. Their cores, so called Active Galactic Nuclei (AGN), harbour a supermassive black hole which accretes matter and causes the central galactic region to be very luminous.

In this Chapter I will give a historical overview of the detection of AGN, discuss the different types of AGN and introduce the physics of AGN by following Beckmann & Shrader (2012) and Wilms & Kreykenbohm (2015).

1.1 Historical overview

Edward A. Fath (1909) was the first to find emission lines in a spectrum from the galaxy NGC 1068, which during that time was believed to be just a nebula inside the Milky Way. The emission lines were somewhat confusing, because if assuming the radiation comes only from stars, one would expect just absorption lines. The presence of emission lines implies hot gas, as for example in planetary nebulae. Years later, Carl Seyfert (1943) performed the first systematic study of emission lines in spiral galaxies. Those with a point-like and bright core showed a spectrum of strong emission lines in the normal galaxy spectrum. Some galaxies even showed very broad lines.

Surveys in the 1950s and 1960s discovered objects with strong, point-like radio emission, which were named quasars for being quasi-stellar radio sources. The biggest surveys were the "Third Cambridge Catalogue" (Edge et al., 1959), the "Revised Third Cambridge Catalogue" (Bennett, 1962) and the Parkes surveys (Bolton et al. (1964); Price & Milne (1965); Day et al. (1966)). However, AGN are not only bright in the radio spectral range. Zamorani et al. (1981) found AGN to be generally bright in the X-rays, while not all of them show strong radio emission.

Baade & Minkowski (1954) identified the optical counterparts to three radio sources, linking them to galaxies. The high luminosity of all these unexplained sources urged scientists to find an explanation for emission processes powerful enough to cause the observed brightness. The first step in the development of AGN physics was done by Lodewijk Woltjer (1959), who concluded that, due to the small size of the central regions of active galaxies, the cores must have huge masses of 10^8 solar masses ($M_\odot$) according to the normal mass-to-light ratios. Following this, Hoyle & Fowler (1963) suggested matter accretion on a stellar-type massive object via accretion to be the reason for the large energy output. The basic idea for our current understanding of AGN physics emerged when Salpeter (1964) and Zel'dovich & Novikov (1964) stated that the supermassive object is not a hypermassive star, but a supermassive black hole. Maarten Schmidt (1963) was the first to discover an extremely large distance to AGN objects when he found a redshift of $z = 0.158$ for the object 3C 273. Since then, many more AGN with higher redshifts have been detected. The currently most distant object of that type is the quasar ULAS J112001.48+064124.3 for which Mortlock et al. (2011) determined a redshift of $z = 7.1$.

Some AGN show jets. Before the Great debate in 1920, Curtis (1918) observed a long, aligned stream of matter which originates in the core of the nebula M87. For some years, the nature of the jet remained unclear, until radio observations showed a bright emission region distant to the core of M87 (in the radio referred to as 3C 274). Hogg et al. (1969) linked the radio emission with the optically bright spot in the jet. Over time, jets were found in more AGNs and can also be detected in other wavebands.

1.2 The AGN zoo

Since the first detection of AGN, they have been studied and observed in all frequencies and many different classes of AGN were found. In this section I will briefly introduce the variety of the AGN zoo.

The main distinction for AGN was introduced by Kellermann et al. (1989) when they discovered that, although all AGN emit radio signals, only a small percentage ($\approx 10\%$) of them shows strong radio emission. In a newer study, Kellermann et al. (2016) state a distribution of 20% radio-loud versus 80% radio-quiet AGN for low redshift objects ($0.2 < z < 0.3$). Using the ratio

$$R_{r-o} = \frac{F(6\,\mathrm{GHz})}{F(4400)\mathring{A}} \tag{1.1}$$

of the radio to the optical flux, AGN with $R_{r-o} = 10 - 1000$ are categorised as radio-loud and AGN with $0.1 < R_{r-o} < 1$ as radio-quiet. The strong radio emission from radio-loud AGN originates from the large scale jet structures, which are not present in radio-quiet AGN.

1.2.1 Radio-quiet AGN

First, let us have a look at the variety of radio-quiet AGNs, which can be divided in the classes of Seyfert galaxies, LINERs and QSOs.

1.2.1.1 Seyfert galaxies

The first AGN were studied by Carl Seyfert (1943). He investigated spiral galaxies with unusual bright cores and found strong emission lines in their spectra. Seyfert galaxies can be further distinguished in two classes based on the presence of broad optical lines (Khachikian & Weedman, 1974). In the spectra of Seyfert I galaxies exist broad lines as well as narrow forbidden lines (see

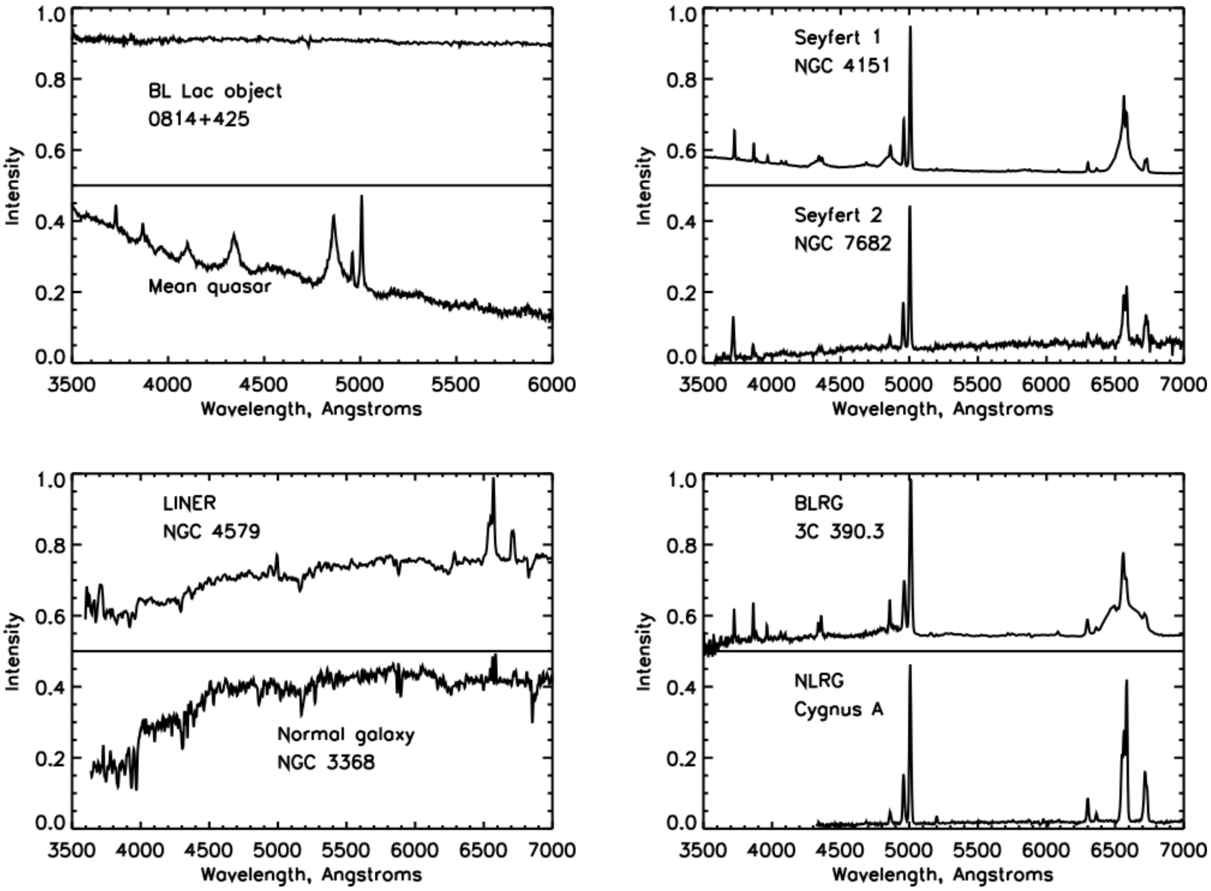

Figure 1.1: Comparison of different AGN spectra in the optical. The scaling is done such that the spectra fit together in one plot. (Credit: W. Keel, priv. comm.)

also Sect.1.3). Seyfert II galaxies lack those broad emission lines. In Fig. 1.1 a part of an optical spectrum is shown for both types in the upper right panel. However, intermediate classes were found as well (Osterbrock & Koski 1976; Osterbrock & Martel 1993), and are classified as, e.g., Sy 1.5, or Sy 1.9.

1.2.1.2 LINERs

Timothy Heckman (1980) identified Low-Ionisation Nuclear Emission Region (LINER) galaxies, which, apart from having a weaker continuum, resemble optical Seyfert II spectra. An example for a LINER spectrum is shown in Fig. 1.1 in the lower left panel, in comparison to a spectrum from a normal galaxy. Ho et al. (1997) found that nearly one-third of nearby galaxies feature LINER characteristics in their spectra. While some scientists (Heckman 1980; Ho et al. 1993) integrated LINERs into the AGN zoo, others presumed the emission lines to result from star formation (Terlevich & Melnick 1985; Shields 1992). Until today this open question is not solved yet. However, most LINERs close to us have old stellar populations and show very low star formation activity (Bendo & Joseph, 2004).

1.2.1.3 QSOs

Quasi-stellar objects (QSOs) are the radio-quiet counterparts to the radio-loud quasars. Studying over 2200 QSO spectra from the Sloan Digital Sky Survey (SDSS), Vanden Berk et al. (2001)

discovered that the average optical QSO spectrum is similar to Seyfert spectra. A QSO shows weaker narrow lines and weaker absorption from its host galaxy. The main difference to Seyfert galaxies is the higher luminosity of the central region, which outshines the host galaxy of the QSO.

1.2.2 Radio-loud AGN

AGN with a high radio to optical flux ratio (defined in Eq. 1.1) fall into the category of radio-loud AGN. Those AGN are further split into the categories of radio galaxies, quasars, whose spectra include optical lines, and blazars, which lack these lines.

1.2.2.1 Radio galaxies

After analysing a sample from the 3CR catalogue (Bennett, 1962), Fanaroff & Riley (1974) found a connection between the luminosity of a source and the apparent origin of its radio emission and introduced a classification based on the morphology of these sources. Radio galaxies labeled as Fanaroff-Riley type I (FR I) show compact radio emission close to the nucleus and are less luminous than Fanaroff-Riley type II (FR II) AGN, whose radio emission is mostly present in lobes far from the core. Figure 1.2 displays the difference between both types. While for FR I objects one can see two jets originating from the nucleus, FR II objects seem to only have a one-sided jet. The reason for this is relativistic beaming (see also Sect. 1.3).

In some radio galaxies, optical lines can be detected in the spectrum if the continuum is weak. These line features resemble very much the emission lines, which are observed in Seyfert galaxies. Therefore, radio galaxies can be also distinguished into broad-line radio galaxies (BLRG), if broad and narrow line types are present, or into narrow-line radio galaxies (NLRG), if only narrow lines are detectable. Two example spectra for these subclasses are shown in Fig. 1.1 in the lower right panel.

1.2.2.2 Quasars

Quasi-stellar radio sources (quasars) are the radio-loud counterparts of QSOs and the most luminous AGN, allowing them to be detectable at very high redshifts. A jet is their main source for the strong radio emission. Their optical spectra are populated by broad and narrow lines, similar to Seyfert galaxies (Smith 1975; Weedman 1977; Davidson & Netzer 1979). The spectrum of a mean quasar can be found in Fig. 1.1 in the upper left panel.

1.2.2.3 Blazars

While most AGN exhibit some continuum variability, blazars show large amplitude variations on time scales of minutes to years in their spectra (Ulrich et al., 1997). The first type of this AGN was found in 1929, when Hoffmeister (1929) discovered a highly variable object in the constellation Lacerta, which was then thought to be a star. Similar sources detected afterwards were classified as BL Lac type objects. Their spectrum shows nearly no emission lines, as can be seen in Fig. 1.1 in the upper left panel. A subclass of BL Lac objects are the highly polarised quasars (HPQ; Brinkmann et al. 1996; Scarpa & Falomo 1997), whose polarisation originates from synchrotron radiation in optically thin emitting regions(Smith et al., 1994). Other types of very variable AGN and therefore subclasses of blazars are optically violent variable (OVV) quasars, whose luminosity is especially variable in the optical and flat spectrum radio quasars (FSRQs).

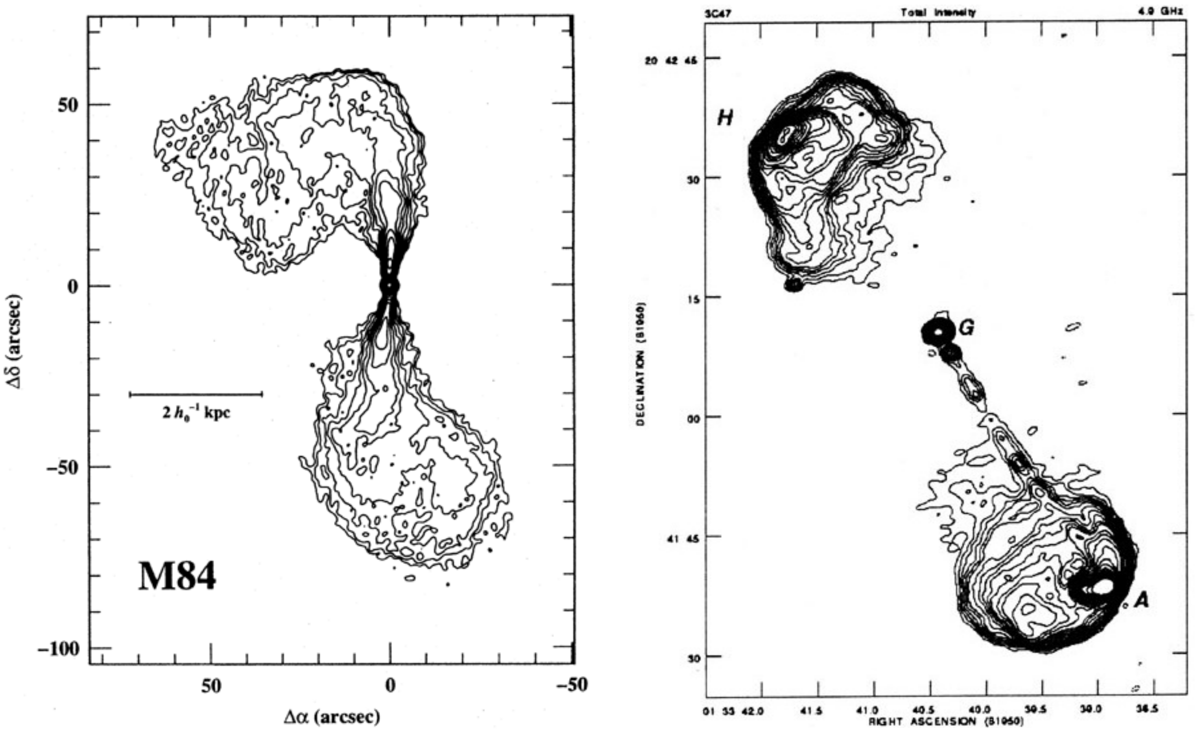

(a) M84, FR I (Laing & Bridle, 1987)

(b) 3C 47, FRII (Bridle et al., 1994)

Figure 1.2: Fanaroff-Riley type I (a) and type II (b). The darker the area is coloured, the stronger the emission coming from there.

The name blazar originates from the combination of the term BL Lac and quasar and characterises the "blazing" nature of these objects very well (see Sect. 1.3).

1.3 The physics of AGN

Studying large samples of AGN, e.g., by the SDSS (York et al. 2000; Richards et al. 2006), one find that, apart from the jet, most differences between AGNs can be traced back to the presence, absence or properties of specific optical emission lines. This lead to the assumption that all kinds of AGN arise from the same phenomenon. A unified scheme for AGN was first introduced by Antonucci (1993), stating that most differences are due to observational bias and AGN basically underlie the same physics.

1.3.1 Unification paradigm for AGN

The first step for a unification paradigm for AGN was made by Scheuer & Readhead (1979), who tried to combine similarities and differences of QSOs and quasars into one model. A suggestion for the unification of quasars and radio galaxies was made by Barthel (1989a,b). In addition, polarisation studies on radio galaxies revealed broad optical lines in polarised spectra which are not present in the total intensity spectra. This lead to the assumption that a toroidal obscuration exists, that reflects the polarised light and masks the region where broad lines are produced (Antonucci, 1984). From this assumption Antonucci & Miller (1985) concluded that AGN are the same objects, which we see from different angles.
Urry & Padovani (1995) finalised the unification scheme, shown in Fig. 1.3. The central engine,

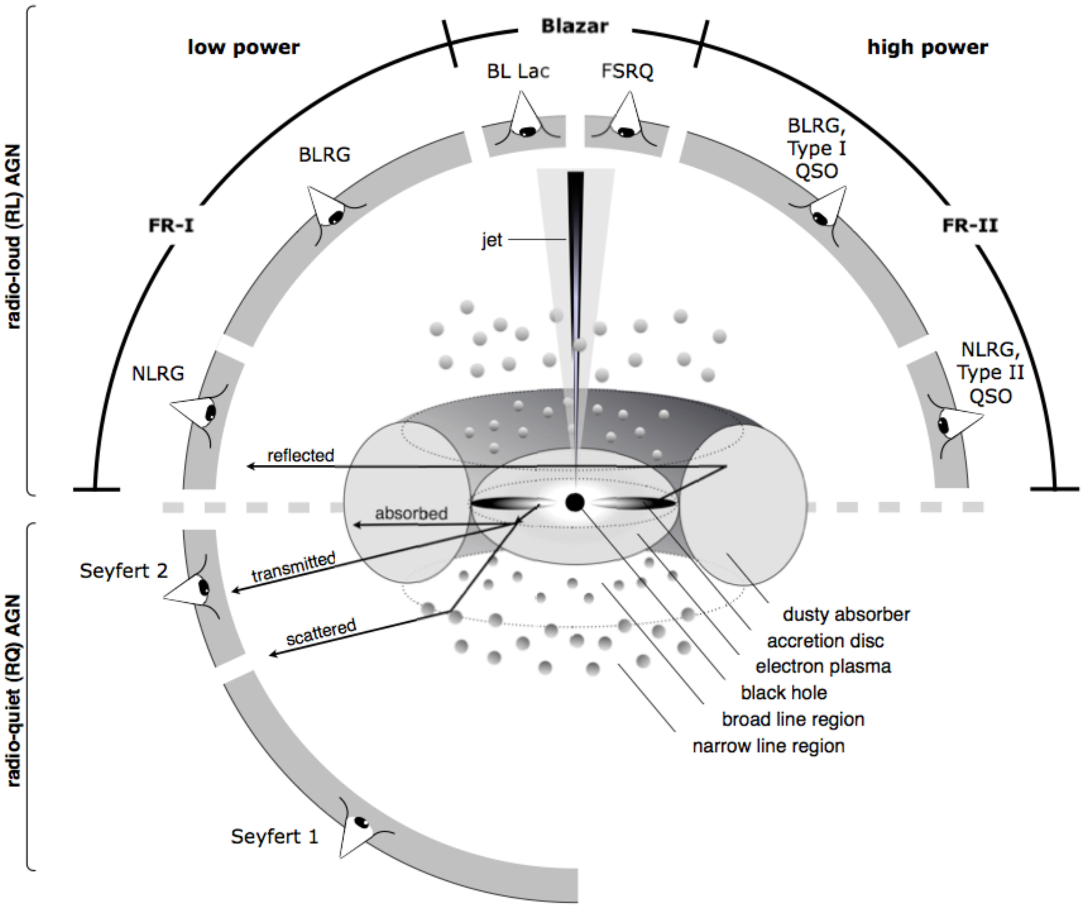
Blazar
low power
high power
BL Lac
FSRQ
BLRG
BLRG,
Type I
QSO
FR-I
FR-II
jet
NLRG
NLRG,
Type II
QSO
radio-loud (RL) AGN
reflected
absorbed
transmitted
scattered
Seyfert 2
radio-quiet (RQ) AGN
dusty absorber
accretion disc
electron plasma
black hole
broad line region
narrow line region
Seyfert 1

Figure 1.3: Unified scheme for AGN. The upper part includes a jet and shows how radio-loud AGN are classified differently depending on the inclination angle. Note that in the case of radio-loud AGN, a counterjet exists, but is not always seen due to the beaming effect. The lower part shows the same but for radio-quiet AGN, therefore not jet is present. Note that Beckmann & Shrader (2012) did not distinguish between radio-quiet and radio-loud quasars and combined these objects. Illustration by Beckmann & Shrader (2012).

a supermassive black hole with a mass of up to $10^{10}M_{\odot}$ (Ghisellini et al., 2010) is closely surrounded by an accretion disc. In the Broad Line Region (BLR) originate broad emission lines originate from allowed transitions, indicating a dense medium ($n > 10^{9}\mathrm{cm}^{-3}$; Osterbrock 1989; Baldwin et al. 2003). Their line widths are broadened due to the Doppler shift and are therefore a sign of high velocities of the emitting medium (up to 10^{4} km s^{-1}; Corbin 1995). Further out, a torus resides and blocks the view into the inner region of the system, including the BLR. If one looks at it from a large inclination angle, e.g., in the case of Seyfert II galaxies, one observes only narrow lines. These lines are emitted in the Narrow Line Region (NLR) and result from forbidden transitions, which are only possible in a medium with low density ($n \sim 10^{3} - 10^{6}\mathrm{cm}^{-3}$) The classification into radio-quiet and radio-loud AGN depends on their quantity of radio emission compared to optical flux (see Eq. 1.1) and the existence of a jet. In the case of radio galaxies, it is possible to study the jet's morphology. If the jet is pointed at us or we observe the source from a small inclination angle, it is called a blazar.

1.3.2 Accretion

It is generally accepted that the high luminosity of AGN is created by the accretion of matter onto a supermassive black hole. Gas, which come too close to the black hole and can not escape its gravitational potential, does not fall onto the black hole immediately, but forms an accretion disc due to the conservation of energy and momentum (Shakura & Sunyaev, 1973) and produces radiation. Viscosity inside the disc induces outward transport of angular momentum, allowing the accretion of matter. If matter trespasses the innermost stable orbit, it falls onto the black hole. Viscosity is very difficult to calculate theoretically (Pringle, 1981). One natural example being able to explain it are magneto-rotational instabilities (MRI), which are responsible for an increasing inhomogeneity of magnetic fields (Balbus & Hawley, 1991).
The Eddington luminosity defines the theoretical maximum luminosity of an accreting object based on the assumption of the gravitational force being equal to the radiation pressure. It is given as

$$L_{\mathrm{Edd}} = \frac{4\pi G M m_{\mathrm{p}} c}{\sigma_{\mathrm{T}}} = 1.3 \cdot 10^{38} \mathrm{erg s}^{-1} \frac{M}{M_{\odot}} \tag{1.2}$$

with the mass M of the black hole, the proton mass m_{p} and the Thomson cross-section σ_{T}. The efficiency η of accretion joins the luminosity and the mass accretion rate $\dot{M}$ of an object as

$$L = \eta \cdot \dot{M} c^2 \quad . \tag{1.3}$$

We can use Eq. 1.3 to find the maximum mass accretion rate needed to power an AGN emitting at Eddington limit:

$$\dot{M}_{\mathrm{max}} = \frac{L_{\mathrm{Edd}}}{\eta c^2} \quad . \tag{1.4}$$

For a typical efficiency of $\eta = 0.1$ (accretion is about 14 times more efficient than nuclear fusion), an accretion rate of $1-2\,M_{\odot}\,\mathrm{yr}^{-1}$ suffices to produce the observed luminosities of AGN (Lasota et al., 1996).

1.3.3 Jets

The theory of jet formation was largely influenced by Blandford & Znajek (1977) and Blandford & Payne (1982). The non-relativistic solution by Blandford & Payne (1982) involves a magnetic field, whose field lines are frozen in the accretion disc. Due to the rotation of the disc, magnetic tower form (see Fig. 1.4) and gas pressure in the magnetically dominating corona powers the outflow, allowing to extract momentum from the thin accretion disc. The jets stays collimated over long distances because of the toroidal component of the magnetic field.
In the theory of Blandford & Znajek (1977), energy extraction of a rapidly rotating black hole (Kerr black hole; Kerr 1963) is proposed. As the area close to a supermassive black hole is subject to strong gravitational pull, an effect called "frame-dragging" occurs, which distorts the spacetime metric and is able to helically twist the magnetic field lines. The interaction of two particles inside the ergosphere allows energy extraction from the black hole (Penrose, 1969) by the escaping particle. In the presence of a magnetic field, the escaped particles can be accelerated into the jet. Simulations in 2D and 3D are used to prove this theory and to determine the physical parameters, which are crucial for the launch of a jet (Kigure & Shibata 2005; McKinney 2006; McKinney et al. 2014).
If we look at radio-loud AGN from a low inclination angle, it is possible to measure apparent superluminal motion of the jet, as was discovered first by Cohen et al. (1971) and Whitney et al.

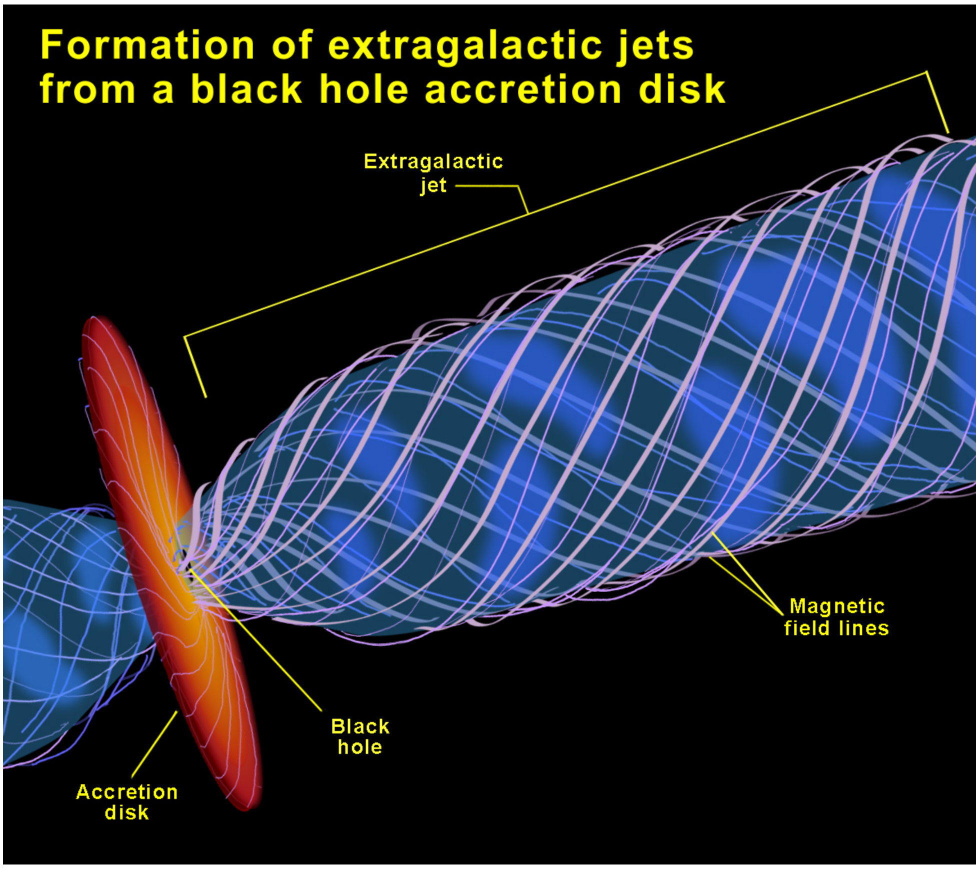
Formation of extragalactic jets from a black hole accretion disk
Extragalactic jet
Magnetic field lines
Black hole
Accretion disk

Figure 1.4: Schematic jet launch in an AGN. The light lines represent the magnetic field lines. ©NASA/ESA and Ann Feild (Space Telescope Science Institute) (www.spacetelescope.org)

(1971). This proved to be just a projection effect, which is intensified by the particles moving with $v \simeq c$. These relativistic velocities also create the special characteristic of blazars. The radiation coming from the particles in the jet is strongly confined into their direction of motion due to their high relativistic velocities (see Eq. 2.18 and Fig. 2.1 in Sect. 2.1). Therefore, the radiation seems to be boosted towards the observer. The same effect also causes the apparent absence of the counterjet, as we can see in FR II galaxies. The radiation from particles in the counterjet get boosted away in the opposite direction and the remaining flux into our direction is too low to be detected.

1.3.4 Radiative processes

AGN emit radiation over the whole electromagnetic spectrum. The radiation originating from thin accretion discs is thermal radiation peaking in the optical to UV range. The radiation from the jet is caused by synchrotron radiation and the inverse Compton effect or hadronic processes. The spectral energy distribution of blazars (see Fig. 1.5) typically shows two broad peaks in $\nu F(\nu)$ space. The first peak at lower energies is well known to result from synchrotron radiation by electrons. The peak in the γ-rays can be explained by either leptonic or hadronic processes and their relative involvements is yet to be determined (Abdo et al. 2011; Böttcher et al. 2013; Mannheim & Biermann 1992).
The leptonic model involves electrons and explains the high energy peak with the inverse Comp-

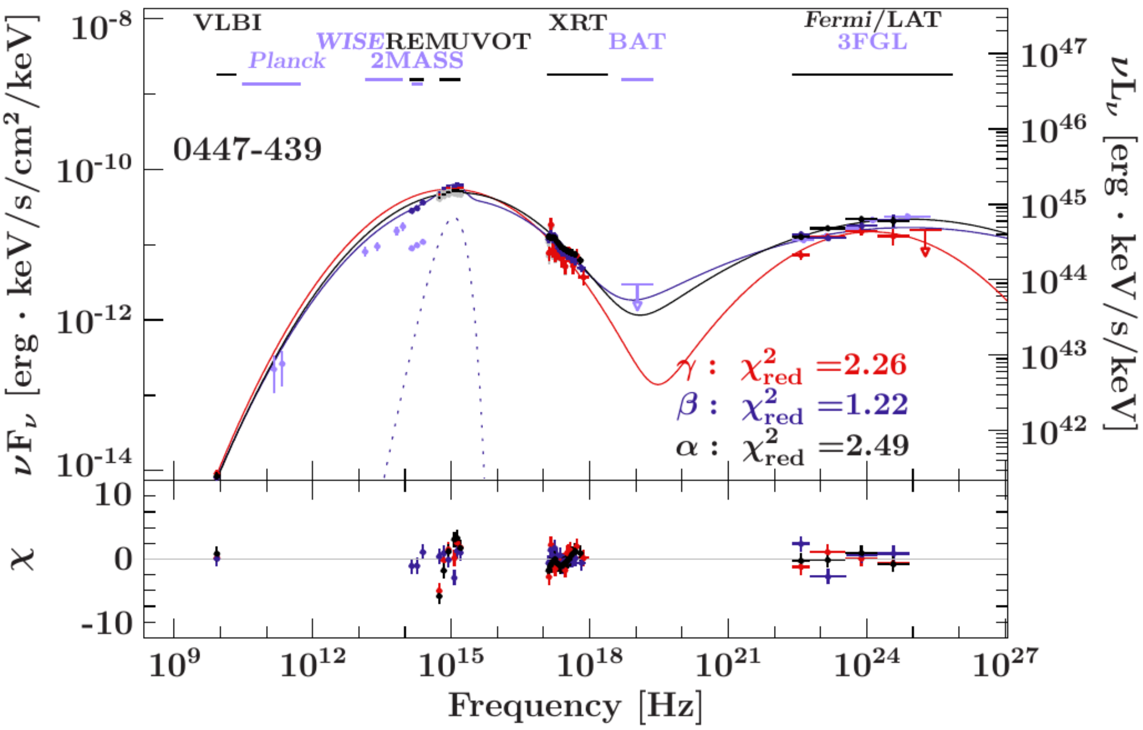

Figure 1.5: Broadband spectral energy distribution of PKS 0447-439. The model includes both peaks and an additional blackbody for present thermal excess. (Krauß et al., 2016)

ton effect, which describes an electron up-scattering a photon to higher energies. In the case of AGN jets, the seed photons for this process can originate from synchrotron radiation and get up-scattered by the same electrons, which emitted them before. This is called Synchrotron-Self-Compton (SSC; Ghisellini et al. 1985; Maraschi et al. 1992; Ghisellini & Madau 1996; Celotti et al. 1997). The seed photons can also come from an external source, e.g., the accretion disc or the cosmic microwave background (Dermer et al. 1992; Sikora et al. 1994; Tavecchio et al. 2000). The inverse Compton effect is then called External Compton (EC).

The hadronic model involves photon-hadron or hadron-hadron processes, as well as pair production (Mannheim, 1993a,b). The interaction of protons with low-energy photon produces pions, which decay and create γ-rays and neutrinos in this process (Mannheim & Biermann, 1989). The presence of hadronic elements in the jet can therefore be proven by the detection of very energetic neutrinos, which are produced in the collisions (Mannheim 1995; Krauß et al. 2015). Krauß et al. (2014) showed that the detection of two PeV neutrino events by the IceCube experiment (Aartsen et al., 2013) is in agreement with the expected neutrino flux for six blazars in the positional uncertainty region of the events.

Chapter 2

Theory of synchrotron radiation

Whenever charged particles move in or through a magnetic field, they get accelerated to another direction of motion. This change causes them to lose energy in terms of radiation. In the case of non-relativistic velocities, this emission is called cyclotron radiation. Particles moving with a relativistic speed emit so called synchrotron emission. Both emissions are special cases of bremsstrahlung. In nature we observe synchrotron radiation whenever there is hot plasma moving within a magnetic field as it is the case for AGN jets. Understanding the physics of synchrotron radiation is necessary to understand the processes happening in such astrophysical sources.

This chapter will be a detailed discussion of the theory of synchrotron radiation processes following *Radio Astrophysics* by Pacholczyk (1970) unless stated otherwise. In Sect. 2.1 we will derive a general expression for the radiation and show that the emission is strongly confined to a cone with an opening angle of $1/\gamma$. We will calculate the motion of a charged particle in a magnetic field in Sect. 2.2 and use this for the derivation of a mono-energetic spectrum for a single electron in Sect. 2.3. We will then compute the synchrotron radiation for an ensemble of electrons in Sect. 2.4 including the emission coefficient (Sect. 2.4.1), the absorption coefficient (Sect. 2.4.2) and the general solution of the radiative transfer equation (Sect. 2.4.3). Finally, in Sect. 2.4.4 we will find concrete equations for a power-law distribution of electrons.

2.1 Electromagnetic field of an accelerated charge

The Maxwell equations describe the properties and connection of electric and magnetic fields using charge and current densities Q and $\mathbf{j}$. They can be solved by retarded vector and scalar potentials $\mathbf{A}$ and φ

$$\mathbf{A}(\mathbf{R},t) = \frac{1}{c}\int R_0^{-1}\mathbf{j}(\mathbf{r}',t')\,\delta\left(t'-t+\frac{R_0(t')}{c}\right)\mathrm{d}\tau'\,\mathrm{d}t' \tag{2.1}$$

$$\varphi(\mathbf{R},t) = \int R_0^{-1}Q(\mathbf{r}',t')\,\delta\left(t'-t+\frac{R_0(t')}{c}\right)\mathrm{d}\tau'\,\mathrm{d}t' \tag{2.2}$$

with c being the speed of light, R_0 being the distance from the volume element of a charge or a current to the observer and $\mathbf{r}'$ being the radius vector of the volume element $d\tau$. From the δ-function we get the expression of the retarded time

$$t' = t - \frac{R_0(t')}{c} \quad . \tag{2.3}$$

Since we are looking at single particles moving very fast, we can write the charge and current densities using the δ-function as

$$\mathbf{j}(\mathbf{r}', t') = ec\boldsymbol{\beta}(t)\,\delta(\mathbf{R} - \mathbf{r}(t)) \quad \text{and} \tag{2.4}$$

$$Q(\mathbf{r}', t') = e\delta(\mathbf{R} - \mathbf{r}(t)) \quad , \tag{2.5}$$

with the electric charge e, and insert them into Eq. (2.1) and Eq. (2.2). For the integration over the δ-function we can use

$$\int f(x)\,\delta(g(x) - y)\,\mathrm{d}x = \left[\frac{f(x)}{\frac{\mathrm{d}g(x)}{\mathrm{d}x}}\right]_{g(x)=y} \tag{2.6}$$

where $g(x)$ equates to $t = t' + R_0(t')/c$ and $x = t'$. For $\mathbf{R_0}(t') = (R - r')\mathbf{R_0'^*}$, with $\mathbf{R_0'^*}$ as a unit vector for R_0, we find $\partial\mathbf{R_0}(t') = -c\boldsymbol{\beta}' \cdot \mathbf{R_0'^*}$. Using this, we get

$$\frac{\partial t}{\partial t'} = 1 - \boldsymbol{\beta}' \cdot \mathbf{R_0'^*} \tag{2.7}$$

and we can solve the integrals in Eq. (2.1) and Eq. (2.2):

$$\mathbf{A}(\mathbf{R}, t) = \frac{e\boldsymbol{\beta}'}{R_0'(1 - \boldsymbol{\beta}' \cdot \mathbf{R_0'^*})} \quad , \tag{2.8}$$

$$\varphi(\mathbf{R}, t) = \frac{e}{R_0'(1 - \boldsymbol{\beta}' \cdot \mathbf{R_0'^*})} \quad . \tag{2.9}$$

Those potentials are the Liénard-Wiechert potentials, which we can be used to calculate the field intensities **E** and **B**:

$$\mathbf{E} = -\frac{1}{c}\frac{\partial \mathbf{A}}{\partial t} - \nabla\varphi, \tag{2.10}$$

$$\mathbf{B} = \nabla \times \mathbf{A}. \tag{2.11}$$

It is necessary to differentiate the potentials with respect to the observer's coordinates and time. If we assume a large distance between observer and radiating particle, because we deal with astrophysical sources, we yield

$$\mathbf{E} = \frac{e}{R_0'}\frac{\mathbf{R_0'^*} \times [(\mathbf{R_0'^*} - \boldsymbol{\beta}') \times \dot{\boldsymbol{\beta}}']}{c(1 - \boldsymbol{\beta}' \cdot \mathbf{R_0'^*})^3} \quad , \tag{2.12}$$

$$\mathbf{B} = \mathbf{R_0'^*} \times \mathbf{E} \quad . \tag{2.13}$$

We can calculate the radiation of the moving charge by using the Poynting vector $\mathbf{S} = \mathbf{E} \times \mathbf{B}$, which describes the directional energy flux density of electromagnetic fields, and get

$$\widetilde{p_\Omega} = \frac{c}{4\pi}E^2 R_0^2 \quad . \tag{2.14}$$

By inserting Eq. (2.12) and calculating the terms, we can condense the result to

$$\widetilde{p_\Omega} = \frac{e^2}{4\pi c}\left(\frac{(\dot{\boldsymbol{\beta}}')^2}{(1-\boldsymbol{\beta}'\cdot\mathbf{R}_0'^{*})^4} + \frac{2(\mathbf{R}_0'^{*}\cdot\dot{\boldsymbol{\beta}}')(\boldsymbol{\beta}'\cdot\dot{\boldsymbol{\beta}}')}{(1-\boldsymbol{\beta}'\cdot\mathbf{R}_0'^{*})^5} + \frac{(\mathbf{R}_0'^{*}\cdot\dot{\boldsymbol{\beta}}')^2}{\gamma^2(1-\boldsymbol{\beta}'\cdot\mathbf{R}_0'^{*})^6}\right) \tag{2.15}$$

with the Lorentz factor γ. We can already see in this equation that the amount of radiation is not isotropically distributed but strongly dependent on the direction of the particle's velocity. The intensity becomes largest for a small value of $1-\boldsymbol{\beta}'\cdot\mathbf{R}_0'^{*}$. For a relativistic particle we can assume $\beta = v/c \approx 1$ and therefore approximate

$$\beta = \sqrt{\frac{1}{1-\frac{1}{\gamma^2}}} \simeq 1 - \left(\frac{1}{2\gamma^2}\right) \tag{2.16}$$

after Padmanabhan (2000) by using the Taylor expansion. As ψ is the angle between the particle velocity $\boldsymbol{\beta}'$ and the direction $\mathbf{R}_0'^{*}$ towards the observer and radiation is only observable if the particle is moving into the direction of the observer, we can use the Taylor expansion for $\psi \ll 1$ and derive

$$(1-\boldsymbol{\beta}'\cdot\mathbf{R}_0'^{*})^{-1} = (1-\beta\cos\psi)^{-1} \simeq \left[1-\left(1-\frac{1}{2\gamma^2}\right)\left(1-\frac{1}{2}\psi^2\right)\right]^{-1} = \frac{2\gamma^2}{1+\gamma^2\psi^2} \quad . \tag{2.17}$$

This term reaches its maximum value of $2\gamma^2$ for $\psi = 0$. However, if we want to know the angle in which most of the radiation is confined, we can calculate the full width half maximum:

$$\frac{2\gamma^2}{1+\gamma^2\psi^2} = \gamma^2 \quad \Rightarrow \quad \psi = \frac{1}{\gamma} \tag{2.18}$$

Therefore the majority of the radiation is emitted in the direction of motion in a cone with an opening angle that is proportional to $1/\gamma$. From Eq. (2.15) one can also derive an expression for the angular distribution of the radiation depending on the particle's velocity β. Two special cases are shown in Fig. 2.1. The first case is for a charged particle which velocity v is parallel to its acceleration a (see Fig. 2.1a). The radiation distribution over the angle ψ can be determined with

$$\widetilde{p_\Omega} \propto \frac{\sin^2(\psi)}{(1-\beta\cos(\psi))^6} \tag{2.19}$$

after Rybicki & Lightman (1979). The second case is a charged particle getting accelerated perpendicular to its direction of velocity. This is given by

$$\widetilde{p_\Omega} \propto \frac{1}{(1-\beta\cos(\psi))^4}\left[1-\frac{\sin^2\cos^2(\phi)}{\gamma^2(1-\beta\cos(\psi))^2}\right] \tag{2.20}$$

after Rybicki & Lightman (1979) with $\gamma = 1/\sqrt{1-\beta^2}$. ϕ is set to zero for convenience in Fig. 2.1b, because the radiation is maximum if the particle moves inside the same plane as the observer.

2.2 Motion of a charged particle in a magnetic field

In order to use the derived Eq. (2.12), Eq. (2.13), and Eq. (2.15), we need to derive an expression for the location and the velocity for each radiating particle. Since we are looking at a charged particle moving along a magnetic field, we can use the Lorentz equation

$$\frac{d\mathbf{p}}{dt} = e\mathbf{E} + \frac{e}{c}\mathbf{v}\times\mathbf{B} \tag{2.21}$$

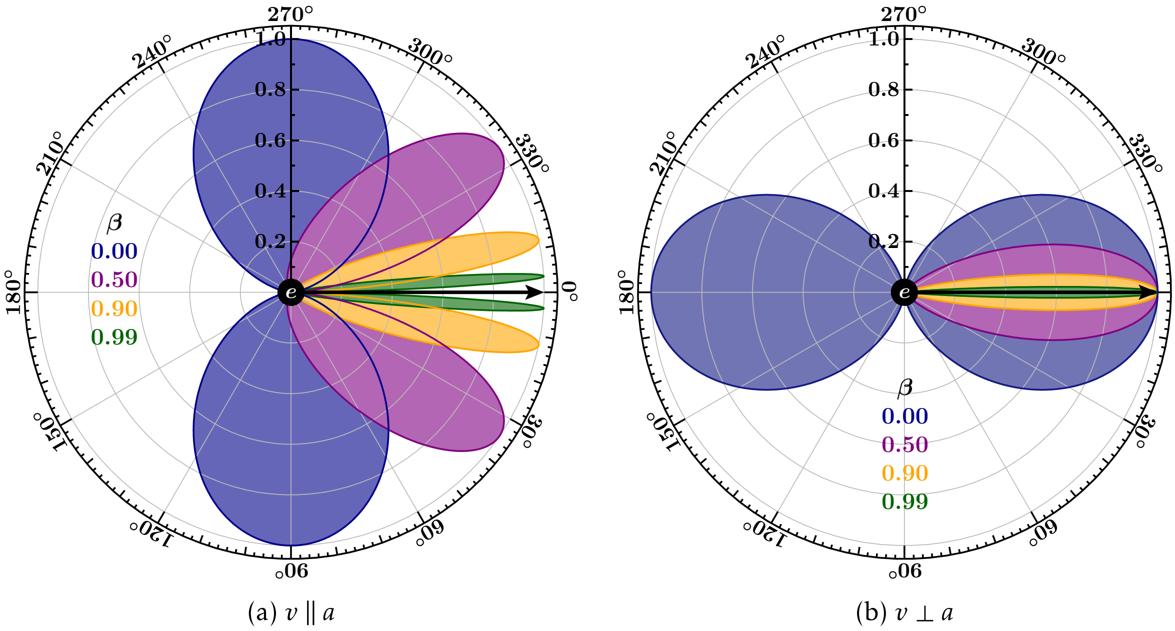

(a) $v \parallel a$ (b) $v \perp a$

Figure 2.1: Angular distribution of radiation for different velocities β of a moving electron. Note that the size of the cones does not allow to compare the different radiation strengths as they are not normalised.

with the particle's momentum $\mathbf{p}$, its velocity $\mathbf{v}$ and its charge e. While the electrostatic force $e\mathbf{E}$ works along the electric field lines, the magnetic force does not perform any work because it is always perpendicular to the particle's velocity. We can assume that there is no external electric field present and the magnetic field is uniform. Additionally we can express the momentum $\mathbf{p}$ via its relativistic relation with energy $\mathcal{E}$ as

$$\mathbf{p} = \frac{\mathcal{E}\mathbf{v}}{c^2} \tag{2.22}$$

in order to get rid of $\mathbf{p}$ and derive Eq. (2.21) with a dependence on $\mathbf{v}$. Eq. (2.21) then reduces to

$$\frac{\mathcal{E}}{ec}\frac{d\mathbf{v}}{dt} = \mathbf{v} \times \mathbf{B} \tag{2.23}$$

and because no work is done through the Lorentz force, we can assume that the particle's energy $\mathcal{E}$ does not change over time. Although there are energy losses due to radiation, the loss term can be neglected in comparison with the Lorentz force. Since we have the freedom of orientation for our coordinate system, we can define the magnetic field to be directed along the z axis. Further, we can multiply $i = \sqrt{-1}$ to the second component of each vector on both sides and adding it to the first component. On the left side of Eq. (2.23) we then have

$$\frac{\mathcal{E}}{ec}\frac{\mathrm{d}\mathbf{v}}{\mathrm{d}t} = \frac{\mathcal{E}}{ec}\frac{d}{dt}\begin{pmatrix} v_x + iv_y \\ v_y \\ v_z \end{pmatrix} \quad . \tag{2.24}$$

On the right side we execute the cross product and apply the same procedure as on the left side, resulting in

$$\mathbf{v} \times \mathbf{B} = \begin{pmatrix} (v_y - iv_x)B \\ -v_x B \\ 0 \end{pmatrix} \quad . \tag{2.25}$$

Taking only the first components of both vectors, we can now derive

$$\frac{\mathrm{d}}{\mathrm{d}t} v_x + i v_y = -i \frac{ecB}{\mathcal{E}} (v_x + i v_y) = -i\omega_B(v_x + i v_y) \tag{2.26}$$

with the gyrofrequency

$$\omega_B = \frac{ecB}{\mathcal{E}} = \frac{eB}{\gamma mc} = \frac{\omega_G}{\gamma} \quad . \tag{2.27}$$

Performing the integration, we get for the velocity of a particle

$$v_x + i v_y = v_{0\perp} \exp[-i(\omega_B t + \alpha)] = v_{0\perp}[\cos(\omega_B t + \alpha) - i \sin(\omega_B t + \alpha)] \tag{2.28}$$

with constants $v_{0\perp}$ and α, which are defined by the initial conditions. We can also write

$$v_x = v_{0\perp} \cos(\omega_B t + \alpha) \quad , \tag{2.29}$$

$$v_y = -v_{0\perp} \sin(\omega_B t + \alpha) \quad . \tag{2.30}$$

When we integrate over Eq. (2.29) and Eq. (2.30), respectively, we gain the formulas to describe the location of a particle by

$$x = r_B \sin(\omega_B t + \alpha) + x_0 \quad \text{and} \tag{2.31}$$

$$y = r_B \cos(\omega_B t + \alpha) + y_0 \quad , \tag{2.32}$$

with $r_B = v_{0\perp}/\omega_B$ being the radius of gyration. Since we know $dv_z/dt = 0$ from Eq. (2.24) and Eq. (2.25), we know for the location in z direction which is parallel to the magnetic field that

$$z = v_{0||} t + z_0 \quad . \tag{2.33}$$

From these results we are able to state that the motion of a charged particle in a magnetic field is a superposition of two simple movements. The first on is the circular motion in a plane perpendicular to the field defined by a circular frequency ω_B and the radius r_B. The second motion is unaffected by the magnetic field since it is parallel to the field. Therefore the superposition creates a helical trajectory, which in vector notation is

$$\mathbf{r}(t) = \frac{c\beta \sin\theta}{\omega_B} (-\mathbf{l} \cos(\omega_B t) + \mathbf{l}_2 \sin(\omega_B t)) + \mathbf{l}_3 t c\beta \cos\theta. \tag{2.34}$$

$\mathbf{l}, \mathbf{l}_2, \mathbf{l}_3$ form a Cartesian coordinate system in which the magnetic field $\mathbf{B}$ is parallel to $\mathbf{l}_3$. θ is the angle between the magnetic field and the direction of the particle's velocity. β is the particle's velocity in units of the speed of light c.

2.3 Spectral distribution of synchrotron radiation of a single electron

Since we want to calculate the spectrum of synchrotron radiation by electrons, we have to look at the spectral distribution by using the Fourier analysis on the electric vector of the emitted radiation. First we start again with the trajectory of the electron, which we derived in the previous subsection. However, since we are investigating electrons which have the charge $-e$, Eq. (2.34) changes slightly, because negatively charged particles move counter-clockwise in a magnetic field due to the Lorentz force. Therefore we can describe the electron's trajectory with

$$\mathbf{r}(t') = \frac{c\beta\sin\theta}{\omega_B}\left(\mathbf{l}\cos(\omega_B t') + \mathbf{l}_2\sin(\omega_B t')\right) + \mathbf{l}_3 tc\beta\cos\theta \tag{2.35}$$

and the electron's velocity $\boldsymbol{\beta}'$ and its acceleration $\dot{\boldsymbol{\beta}}'$ with

$$\boldsymbol{\beta}' = \beta\mathbf{n} = \beta\sin\theta[-\mathbf{l}\sin(\omega_B t') + \mathbf{l}_2\cos(\omega_B t')] + \mathbf{l}_3\cos\theta \quad , \tag{2.36}$$

$$\dot{\boldsymbol{\beta}}' = \beta\omega_B\mathbf{l}_3\times\mathbf{n} \quad . \tag{2.37}$$

If we assume that the observer of the radiation is located in the $\mathbf{l}_2\mathbf{l}_3$ plane, we can write for the direction toward the observer

$$\mathbf{k} = \mathbf{l}_2\sin(\theta-\psi) + \mathbf{l}_3\cos(\theta-\psi) \quad . \tag{2.38}$$

ψ is the angle between $\mathbf{k}$, the direction of the observer, and $\mathbf{n}$, the direction of the electron's velocity, but only when $\mathbf{n}$ is also within the $\mathbf{l}_2\mathbf{l}_3$ plane. Otherwise the angle between both vectors is called η. Because of the electron's circular movement and the characteristic of synchrotron radiation being emitted by the particle only in the direction of motion, the observer detects pulses of radiation. The period of these pulses is

$$T = \frac{2\pi}{\omega_B}(1-\beta_{||}\cos\vartheta) = \frac{2\pi}{\omega_B}(1-\beta\cos\theta\cos\vartheta) \tag{2.39}$$

with ϑ being the angle between $\mathbf{k}$ and $\mathbf{B}$. As we are talking about synchrotron radiation from astrophysical sources here, we can assume a very relativistic electron, meaning $\beta = 1$. Because of the relation between angle ψ and the Lorentz factor γ in Eq. (2.18), we know that the radiation cone of a highly relativistic electron is very narrow. Since we can only detect radiation if the electron's direction of motion shows in the same direction of the observer, we can say $\vartheta \approx \theta$. With those further simplifications we can write

$$T \approx \frac{2\pi}{\omega_B}(1-\beta\cos^2\theta) \approx \frac{2\pi}{\omega_B}\sin^2\theta \quad . \tag{2.40}$$

The whole radiation geometry is shown in Fig. 2.2. As the radiation $\mathbf{E}(t)$ is periodic, we can express $\mathbf{E}(t)$ as a Fourier series of monochromatic waves of frequencies $n\cdot\omega_B/\sin^2\theta$ and write

$$\mathbf{E}(t) = \sum_{-\infty}^{\infty}\mathbf{E}_n\exp\left(-\frac{\omega_B}{\sin^2\theta}nt\right) \quad , \tag{2.41}$$

with the corresponding wave amplitudes

$$\mathbf{E}_n(\mathbf{R}) = \frac{\omega_B}{2\pi\sin^2\theta}\int_0^{\frac{2\pi\sin^2\theta}{\omega_B}}\mathbf{E}(t)\exp\left(i\frac{\omega_B}{\sin^2\theta}nt\right)\mathrm{d}t \tag{2.42}$$

for which $\mathbf{E}_n^{\dagger} = -\mathbf{E}_{-n}$. The emission of one particle into a solid angle $d\Omega = 1$ received in a unit of time $dt = 1$ by an observer at distance $\mathbf{R}$ can be calculated by

$$\widetilde{p}_{n\Omega} = \frac{c}{4\pi}\langle|\mathbf{E}(t)|^2\rangle R^2 \quad . \tag{2.43}$$

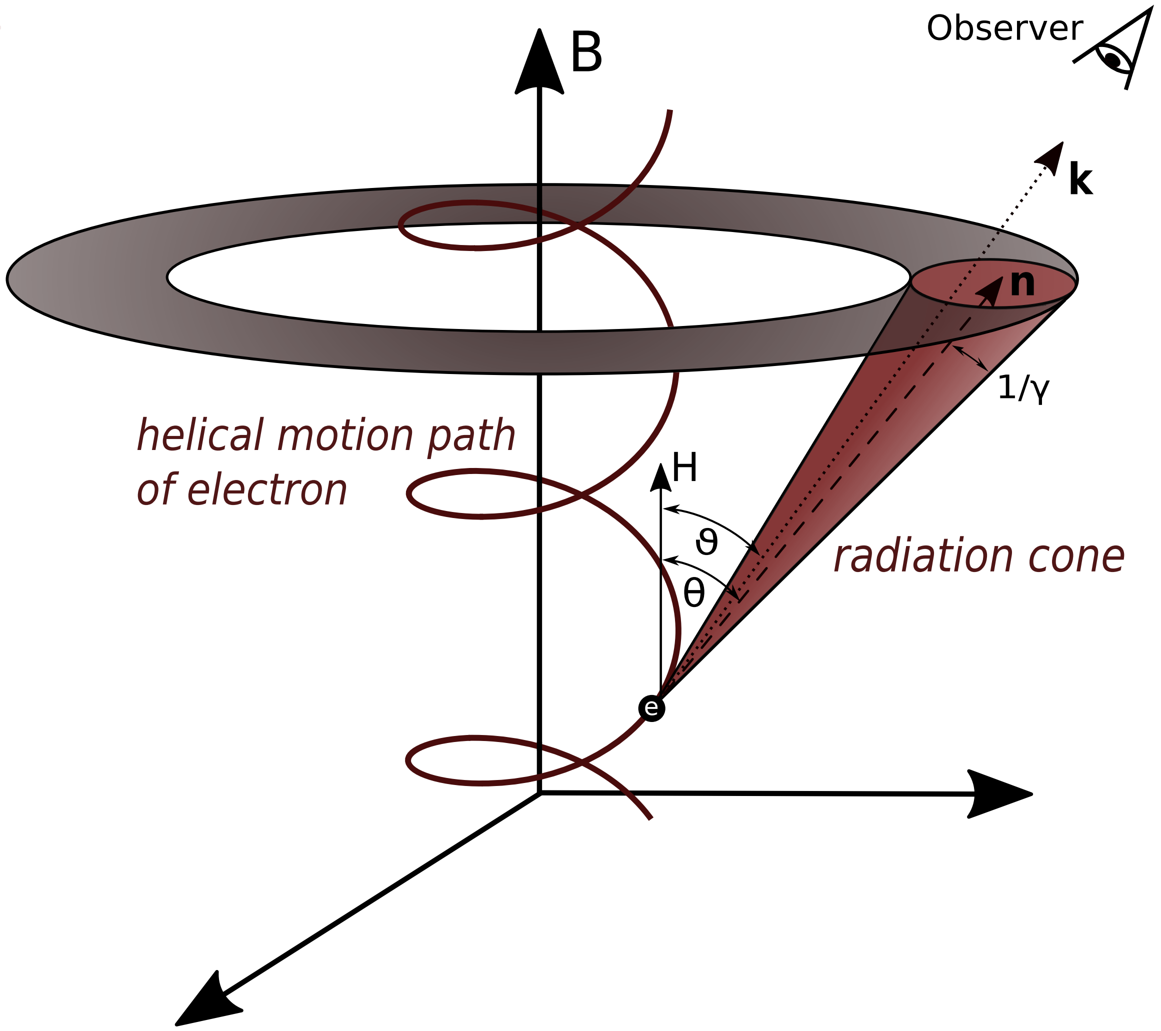

Figure 2.2: Synchrotron radiation geometry for a single electron. **n** shows the momentarily velocity direction of the electron, while **k** points toward the observer.

We can also write this as

$$\frac{4\pi}{cR^2}\widetilde{p}_{n\Omega} = E_0^2 + 2\sum_{n=1}^{\infty}|\mathbf{E}_n|^2 \quad . \tag{2.44}$$

Taking the electric far field of the electron (Eq. 2.12) for $\mathbf{E}(\mathbf{t})$ of Eq. (2.42) and substituting the time t by the retarded time $t' = t - R_0(t')/c$ (Eq. 2.3), we can write for the wave amplitude

$$\mathbf{E}_n(\mathbf{R}) = \frac{\omega_B}{2\pi\sin^2\theta}\int_0^{\frac{2\pi\sin^2\theta}{\omega_B}} \mathbf{E}(t')\exp\left[in\frac{\omega_B}{\sin^2\theta}\left(t' + \frac{R_0(t')}{c}\right)\right]\frac{\partial t}{\partial t'}\,\mathrm{d}t' \quad . \tag{2.45}$$

We can make further assumptions by setting the origin of the reference system close to the electron. The distance to the observer $\mathbf{R}$ is very large compared to the electron radius r in the case for astrophysical objects. We can use that knowledge for the expression of $\mathbf{R_0}(t') = \mathbf{R} - \mathbf{r}(t)$ which we can form into $R_0(t') = R - \mathbf{r}(t')\cdot\mathbf{R_0}'^{*} = R - \mathbf{r}\cdot\mathbf{k}$, because $\mathbf{R}^{*} \approx \mathbf{R_0}'^{*} = \mathbf{k}$ since both $\mathbf{R_0}'^{*}$ and $\mathbf{k}$

point towards the observer. These assumptions help writing Eq. (2.45) more explicit as

$$\begin{aligned}\mathbf{E}_n(\mathbf{R}) =& \frac{\omega_B}{2\pi\sin^2\theta}\frac{e}{cR}\exp\left(in\frac{\omega_B}{\sin^2\theta}\frac{R}{c}\right)\cdot \\ &\cdot\int_0^{\frac{2\pi\sin^2\theta}{\omega_B}}\frac{\mathbf{k}\times[(\mathbf{k}-\boldsymbol{\beta}')\times\dot{\boldsymbol{\beta}}']}{c(1-\boldsymbol{\beta}'\cdot\mathbf{k})^2}\cdot\exp\left(in\frac{\omega_B}{\sin^2\theta}(t'-\frac{\mathbf{k}\cdot\mathbf{r}}{c})\right)\mathrm{d}t' \quad .\end{aligned} \tag{2.46}$$

In order to solve this equation we need to simplify the integral, which is done by again only considering the case of a highly relativistic electron. This means $\gamma \gg 1$ and therefore $1/\gamma \approx 0$ which allows to perform a Taylor expansion for $\beta = \sqrt{1-1/\gamma^2}$. If we neglect higher order terms of $1/\gamma$ from the fourth term on, we have

$$\beta = 1 - \frac{1}{2\gamma^2} \quad . \tag{2.47}$$

We can now this expression for β on other parts of the equation where it is involved, i.e., in

$$1-\boldsymbol{\beta}'\cdot\mathbf{k} = \frac{1}{2\gamma^2}\left(1+\gamma^2\eta^2-\frac{\eta^2}{2}\right) \approx \frac{1}{2\gamma^2}(1+\gamma^2\eta^2) \quad . \tag{2.48}$$

The term $\eta^2/2$ can be neglected against γ since $\eta \ll \gamma$. For other simplifications we just assume $\beta = 1$ and try to simplify the expressions for $\boldsymbol{\beta}'$, $\mathbf{k}-\mathbf{n}$, and η^2. We can use the fact that the gyrofrequency ω_B is very small since it is dependent on $1/\gamma$ (Eq. 2.27) and therefore for $\sin\chi$ and $\cos\chi$ with $\chi = \omega_B t' \ll 1$ we can use the small angle approximation. We also assume that the angle ψ between $\mathbf{k}$ and $\mathbf{n}$ (when both directions are in the same plane) is very small, so the small angle approximation can be applied for $\sin\psi$ and $\cos\psi$ as well. If we write the vector components in the explicit notation, we can derive the following expressions

$$\boldsymbol{\beta}' = \beta\omega_B\mathbf{l_3}\times\mathbf{n} = -\omega_B\sin\theta\,\mathbf{l} - \omega_B\chi\sin\theta\,\mathbf{l_2} \quad , \tag{2.49}$$

$$\mathbf{k}-\mathbf{n} = \chi\sin\theta\,\mathbf{l} - \psi(\mathbf{l_2}\cos\theta - \mathbf{l_3}\sin\theta) = \chi\sin\theta\mathbf{l} - \psi\mathbf{m} \quad , \quad \text{and} \tag{2.50}$$

$$\eta^2 = \chi^2\sin^2\theta + \psi^2 \quad . \tag{2.51}$$

Now we can use all of the simplified expressions to calculate the complex components of Eq. (2.46). We can derive

$$\mathbf{k}\times[(\mathbf{k}-\boldsymbol{\beta}')\times\dot{\boldsymbol{\beta}}'] = \frac{1}{2}\omega_B\sin\theta\left[\mathbf{l}\left(\frac{1}{\gamma^2}+\psi^2-\chi^2\sin^2\theta\right)+\mathbf{m}2\chi\psi\sin\theta\right] \quad , \tag{2.52}$$

$$1-\boldsymbol{\beta}'\cdot\mathbf{k} = \frac{1}{2}\left(\frac{1}{\gamma^2}+\psi^2+\chi^2\sin^2\theta\right) \quad , \tag{2.53}$$

and for the argument in the e-function

$$\frac{\omega_B}{\sin^2\theta}\left(t'-\frac{\mathbf{k}\cdot\mathbf{r}}{c}\right) = \frac{1}{\sin^2\theta}\left[\frac{\chi}{2\gamma^2}(1+\gamma^2\psi^2)+\frac{\chi^3}{6}\sin^2\theta\right] \quad . \tag{2.54}$$

When we insert Eq. (2.52), Eq. (2.53), and Eq. (2.54) in Eq. (2.46), we get

$$\begin{aligned}\mathbf{E}_n(R) = {} & \frac{\omega_B}{\pi \sin^2\theta}\frac{e}{cR}\exp\left(in\frac{\omega_B}{\sin^2\theta}\frac{R}{c}\right)\cdot \\ & \cdot\int_{-\infty}^{+\infty}\exp\left[in\frac{1}{\sin^2\theta}\left[\frac{\chi}{2\gamma^2}(1+\gamma^2\psi^2)+\frac{\chi^3}{6}\sin^2\theta\right]\right]\cdot \\ & \cdot\frac{\mathbf{l}\left(\frac{1}{\gamma^2}+\psi^2-\chi^2\sin^2\theta\right)+\mathbf{m}2\chi\psi\sin\theta}{\left(\frac{1}{\gamma^2}+\psi^2+\chi^2\sin^2\theta\right)^2}\sin\theta\,\mathrm{d}\chi\end{aligned} \tag{2.55}$$

in which we already used the substitution of $t' = \chi/\omega_B$. We can abbreviate the function by introducing the expressions

$$w = \frac{1}{\gamma}\sqrt{1+\gamma^2\psi^2} \quad , \quad s = \frac{n}{2\sin^3\theta} \quad , \quad \text{and} \quad u = \chi\sin\theta \quad . \tag{2.56}$$

The integration over *chi* changes to an integration over u and we can write the wave amplitude as

$$\begin{aligned}\mathbf{E}_n(R) = {} & \frac{e}{\pi cR}\frac{\omega_B}{\sin^2\theta}\exp\left(in\frac{\omega_B}{\sin^2\theta}\frac{R}{c}\right)\cdot \\ & \cdot\int_{-\infty}^{+\infty}\exp\left[is\left(w^2u+\frac{1}{3}u^3\right)\right]\frac{\mathbf{l}(w^2-u^2)+\mathbf{m}2u\psi}{(w^2+u^2)^2}\,\mathrm{d}u \quad .\end{aligned} \tag{2.57}$$

Since there is one part of the integral which is parallel to **l** and the other one parallel to **m**, we can solve the integral separately in respect to each vector. Their derivation is described in Westfold (1959) and yields

$$\int_{-\infty}^{+\infty}\exp\left[is\left(w^2u+\frac{1}{3}u^3\right)\right]\cdot\frac{w^2-u^2}{(w^2+u^2)^2}\,\mathrm{d}u = \frac{2}{\sqrt{3}}sw^2K_{2/3}\left(\frac{2}{3}sw^3\right) \quad , \quad \text{and} \tag{2.58}$$

$$\int_{-\infty}^{+\infty}\exp\left[is\left(w^2u+\frac{1}{3}u^3\right)\right]\cdot\frac{2u}{(w^2+u^2)^2}\,\mathrm{d}u = i\frac{2}{\sqrt{3}}swK_{1/3}\left(\frac{2}{3}sw^3\right) \quad , \tag{2.59}$$

with the Bessel functions $K_{1/3}$ and $K_{2/3}$. We can shorten the argument in the the Bessel functions by defining

$$y = \frac{2}{3}sw^3 = \frac{n}{3\gamma^3\sin^3\theta}(1+\gamma^2\psi^2)^{3/2} \quad . \tag{2.60}$$

Inserting Eq. (2.58), Eq. (2.59) and Eq. (2.60) into Eq. (2.57), by writing the factor s, w, u and y out, only leaving the factor y in the argument of the Bessel functions, we get for the wave amplitude

$$\begin{aligned}\mathbf{E}_n(R) = {} & n\frac{e}{\sqrt{3}\pi cR}\frac{\omega_B}{\sin^5\theta}\exp\left(in\frac{\omega_B}{\sin^2\theta}\frac{R}{c}\right)\cdot \\ & \cdot\left[\mathbf{l}\frac{1}{\gamma^2}(1+\gamma^2\psi^2)K_{2/3}(y)+i\mathbf{m}\frac{\psi}{\gamma}\sqrt{1+\gamma^2\psi^2}\,K_{1/3}(y)\right] \quad .\end{aligned} \tag{2.61}$$

We can see from this equation that the radiation from a single electron is elliptically polarised since the nth harmonic of the electric vector has a linear part in direction **l** and a circular part in direction **m**, because $\mathbf{m} = \mathbf{l}_2\cos\theta - \mathbf{l}_3\sin\theta$. The average power $\widetilde{p}_{n\Omega}\,d\Omega$ (given in Eq. 2.43) can now be parted in the two polarisation states ($\widetilde{p}_{n\Omega} = \widetilde{p}^{(1)}_{n\Omega} + \widetilde{p}^{(2)}_{n\Omega}$), because $\mathbf{E}_n^{(1)} \parallel \mathbf{l}$ and $\mathbf{E}_n^{(2)} \parallel \mathbf{m}$. The direction dependent power equations are

$$\widetilde{p}^{(1)}_{n\Omega} = \frac{c}{2\pi}|\mathbf{E}_n^{(1)}|^2 R^2 = n^2 \frac{e^2\omega_B^2}{6\pi^3 c \sin^{10}\theta}\,\frac{1}{\gamma^4}\,(1+\gamma^2\psi^2)^2\, K^2_{2/3}(y) \quad , \tag{2.62}$$

$$\widetilde{p}^{(2)}_{n\Omega} = \frac{c}{2\pi}|\mathbf{E}_n^{(2)}|^2 R^2 = n^2 \frac{e^2\omega_B^2}{6\pi^3 c \sin^{10}\theta}\,\frac{1}{\gamma^2}\,\psi^2(1+\gamma^2\psi^2)^2\, K^2_{1/3}(y) \quad . \tag{2.63}$$

We are still dependent on the discrete harmonic number n for the spectrum. However, the main assumption for our calculations was the ultra-relativistic nature of the electrons, meaning a large value for the Lorentz factor γ. Then the relevant region where most of the energy is emitted, lies in the higher-order harmonics and we are allowed to consider this spectrum to be practically continuous and can use the frequency ν which is defined as

$$\nu = n\,\frac{\omega_B}{2\pi\sin^2\theta} \quad . \tag{2.64}$$

We can express the critical frequency ν_c at which most radiation is emitted, as

$$\nu_c = \frac{3}{4\pi}\,\omega_B \sin\theta\gamma^3 \tag{2.65}$$

and rephrase Eq. (2.62) and Eq. (2.63) by using

$$x = \frac{\nu}{\nu_c} \quad , \quad y = \frac{x}{2}(1+\gamma^2\psi^2)^{3/2} \quad . \tag{2.66}$$

In order to write it as a continuous spectrum, we need to attend to $\widetilde{p}^{(i)}_{\nu\Omega} = \widetilde{p}^{(i)}_{n\Omega}\,\mathrm{d}n/\mathrm{d}\nu$, which yields

$$\widetilde{p}^{(1)}_{\nu\Omega} = \frac{3e^2}{4\pi^2 c}\,\frac{\omega_B}{\sin^2\theta}\,\gamma^2(1+\gamma^2\psi^2)^2 x^2 K^2_{2/3}(y) \quad \text{,and} \tag{2.67}$$

$$\widetilde{p}^{(2)}_{\nu\Omega} = \frac{3e^2}{4\pi^2 c}\,\frac{\omega_B}{\sin^2\theta}\,\gamma^4\psi^2(1+\gamma^2\psi^2)^2 x^2 K^2_{1/3}(y) \quad . \tag{2.68}$$

When an electron stirs the radial distance dR to the observer in the time $dt' = c/\beta_r\, dR$, it moves with velocity β, and $\beta_r = \beta\cos\theta\cos\vartheta \approx \beta\cos^2\theta$ is the projection of the mean translational velocity of the particle onto the distance R. While the observer lies within the emission cone, the particle moves toward the observer and therefore the time difference between the beginning and the end of the pulse is shorter than in the electron's frame of reference. This effect is called relativistic beaming or also Doppler boosting. Using Eq. (2.3) for the retarded time, we can determine the time in which the observer receives the emitted radiation by the particle which is given by

$$\mathrm{d}t = (1-\beta_r)\,\mathrm{d}t' \approx (1-\cos^2\theta)\,\mathrm{d}t' = \sin^2\theta\,\mathrm{d}t' \quad . \tag{2.69}$$

Following that we can write for the emitted energy per particle in dt' and the received energy by the observer at a unit surface in dt

$$\frac{1}{R^2}\,\widetilde{p}_{\nu\Omega}\,\mathrm{d}t = \frac{1}{R^2}\,\widetilde{p}_{\nu\Omega}\sin^2\theta\,\mathrm{d}t' = \frac{1}{R^2}\,p_{\nu\Omega}\,\mathrm{d}t' \tag{2.70}$$

with $p_{\nu\Omega} = \widetilde{p}_{\nu\Omega}\sin^2\theta$ being the power emitted per frequency ν by the electron within a unit solid angle. The total power emitted by the electron can then be computed by integrating over all frequencies and the full solid angle. As the radiation is the same as the electron energy loss rate, we can write the connection

$$p = \int\!\!\int p_{\nu\Omega}\,\mathrm{d}\nu\,\mathrm{d}\Omega = -\frac{\mathrm{d}E}{\mathrm{d}t} \quad . \tag{2.71}$$

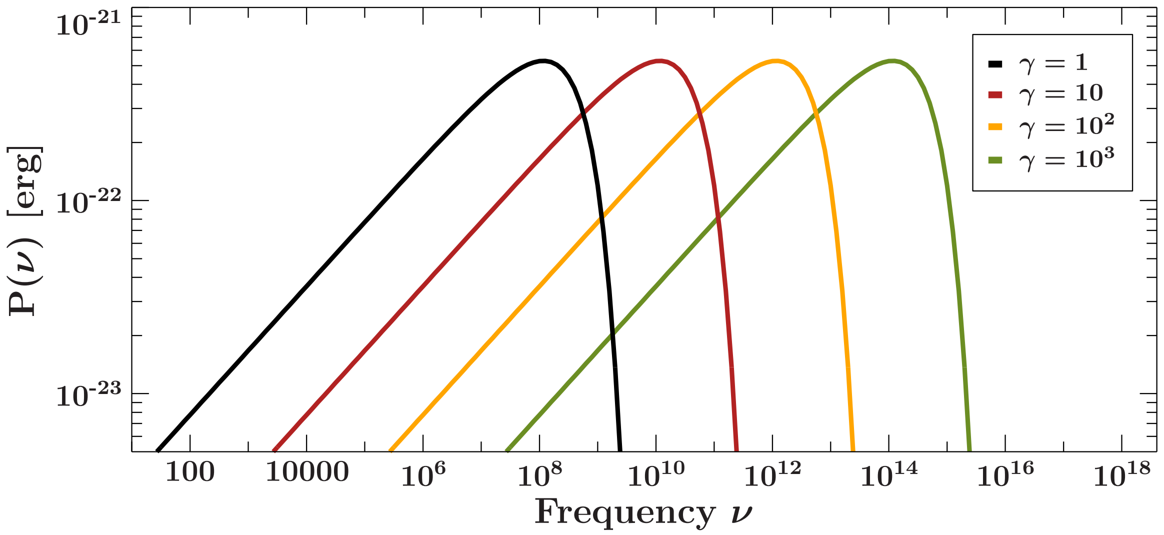

Figure 2.3: Mono-energetic synchrotron emission spectra of electrons with different Lorentz factors γ. Because $\gamma = E/mc^2$, the Lorentz factor is a measure for the energy and the spectra above differ in energy.

2.4 Radiation from an Ensemble of Electrons

In the previous section we could describe a spectrum for a single electron, which depends on its energy. In nature however, we find many electrons emitting synchrotron together in plasma. This section deals with the emission from an electron distribution, synchrotron self-absorption and how to get a final self-absorbed synchrotron spectrum for a power-law distribution.

2.4.1 Emission coefficient

As we normally have many electrons emitting synchrotron radiation in a certain volume $d\tau = R^2 \mathrm{d}R\mathrm{d}\Omega$, we need to consider an electron distribution $N(E,\mathbf{m},\mathbf{R},t)\ \mathrm{d}E\mathrm{d}\widetilde{\Omega}\mathrm{d}\tau$. It is defined by an energy range from E to $E + \mathrm{d}E$ while the particles are moving in directions $\mathbf{m}$ within $d\widetilde{\Omega}$. As we already know from the previous chapter, the observer will only detect radiation from the electrons which move periodically in his direction since the angle in which most of the emission is confined, is proportional to $1/\gamma$. In order to simplify the expression for $N(E,\mathbf{m},\mathbf{R},t)$ we can assume the synchrotron radiation coming from a stationary cloud of electrons. Then, the emission coefficient of a uniform distribution of electrons within a stationary region is

$$\varepsilon_\nu^{(i)} = \int_{4\pi}\int_0^\infty N(E,\mathbf{k})\, p_{\nu\Omega}^{(i)}\, \mathrm{d}\Omega\, \mathrm{d}E \quad , \tag{2.72}$$

provided that the particles are in vacuum. $p_{\nu\Omega}^{(i)}$ is the emitted radiation per electron depending on the direction and the frequency of the electron for a given polarisation (i) (Eq. 2.67 and 2.68). If we assume an isotropic velocity distribution within the electron population, we have

$$\varepsilon_\nu^{(i)} = \frac{1}{4\pi}\int_0^\infty N(E)\left(\int_{4\pi} p_{\nu\Omega}^{(i)}\, \mathrm{d}\Omega\right)\mathrm{d}E = \frac{1}{4\pi}\int_0^\infty N(E)\, p_\nu^{(i)}\, \mathrm{d}E \quad . \tag{2.73}$$

Since the radiation of each electron is strongly confined within a narrow angle and therefore the total emission of an ensemble of electrons is anisotropic, we can limit the integration to the region of the shaded ring (see Fig. 2.2). The limit allows to substitute $\mathrm{d}\Omega$ by $\mathrm{d}\Omega \cong 2\pi \sin\vartheta\, \mathrm{d}\psi$ and to change the integration limits for the integration over ψ from $(-1/\gamma, 1/\gamma)$ to $(-\infty, +\infty)$ because we know that nearly all of the radiation is confined in the cone and consequently an integration over the total space has no effect on the result. Applying those assumptions, we can write

$$p_\nu^{(i)} = \int_{4\pi} p_{\nu\Omega}^{(i)}\, \mathrm{d}\Omega \cong 2\pi \sin\vartheta \int_{-\infty}^{\infty} p_{\nu\Omega}^{(i)}\, \mathrm{d}\psi \quad . \tag{2.74}$$

For $p_\nu^{(1)}$ and $p_\nu^{(2)}$ we get respectively

$$p_\nu^{(1)} = \frac{3e^2}{2\pi c}\,\omega_B \sin\vartheta \gamma^2 x^2 \int_{-\infty}^{\infty} (1+\gamma^2\psi^2)^2 \left[K_{2/3}\left(\frac{x}{2}\sqrt{(1+\gamma^2\psi^2)^3}\right)\right]^2 \mathrm{d}\psi \quad , \tag{2.75}$$

$$p_\nu^{(2)} = \frac{3e^2}{2\pi c}\,\omega_B \sin\vartheta \gamma^2 x^2 \int_{-\infty}^{\infty} \gamma^2\psi^2(1+\gamma^2\psi^2) \left[K_{1/3}\left(\frac{x}{2}\sqrt{(1+\gamma^2\psi^2)^3}\right)\right]^2 \mathrm{d}\psi \quad . \tag{2.76}$$

The integrals over $K_{1/3}$ and $K_{2/3}$ have been solved by Westfold (1959) and yield

$$\int_{-\infty}^{\infty} (1+\gamma^2\psi^2)^2 \left[K_{2/3}\left(\frac{x}{2}\sqrt{(1+\gamma^2\psi^2)^3}\right)\right]^2 \mathrm{d}\psi = \frac{\pi}{\sqrt{3}\gamma x}\left[\int_x^{\infty} K_{5/3}(z)\,\mathrm{d}z + K_{2/3}(x)\right] \quad \text{, and} \tag{2.77}$$

$$\int_{-\infty}^{\infty} \gamma^2\psi^2(1+\gamma^2\psi^2) \left[K_{1/3}\left(\frac{x}{2}\sqrt{(1+\gamma^2\psi^2)^3}\right)\right]^2 \mathrm{d}\psi = \frac{\pi}{\sqrt{3}\gamma x}\left[\int_x^{\infty} K_{5/3}(z)\,\mathrm{d}z - K_{2/3}(x)\right] \tag{2.78}$$

with the Bessel functions $K_{5/3}$ and $K_{2/3}$. For a shorter writing, we can define

$$F(x) = x\int_x^{\infty} K_{5/3}(z)\,\mathrm{d}z \quad , \quad \text{and} \quad G(x) = xK_{2/3} \tag{2.79}$$

with $x = \nu/\nu_c$ (see Fig. 2.4 and Fig. 2.5). Using Eq. (2.79) and the connection between ω_B, γ, B (Eq. 2.27) we can write in a general way

$$p_\nu^{(i)} = \int_{4\pi} p_{\nu\Omega}^{(i)}\,\mathrm{d}\Omega \cong \frac{\sqrt{3}e^3}{2mc^2} B \sin\vartheta \left[F(x) \pm G(x)\right] \quad . \tag{2.80}$$

Inserting Eq. (2.80) into Eq. (2.73), we can now determine the emission coefficients $\varepsilon_\nu^{(i)}$ for a distribution of electrons and can write

$$\varepsilon_\nu^{(i)} = \frac{1}{2}\frac{\sqrt{3}e^3}{4\pi mc^2} B \sin\vartheta \int_0^{\infty} N(E)\left[F(x) \pm G(x)\right]\mathrm{d}E \quad . \tag{2.81}$$

Since x is connected to the energy E, the integration needs to be performed over $F(x)$ and $G(x)$ as well. For the total emission coefficient $\varepsilon_\nu = \varepsilon_\nu^{(1)} + \varepsilon_\nu^{(2)}$ we get

$$\varepsilon_\nu = \frac{\sqrt{3}e^3}{4\pi mc^2} B \sin\vartheta \int_0^{\infty} N(E)F(x)\,\mathrm{d}E \quad . \tag{2.82}$$

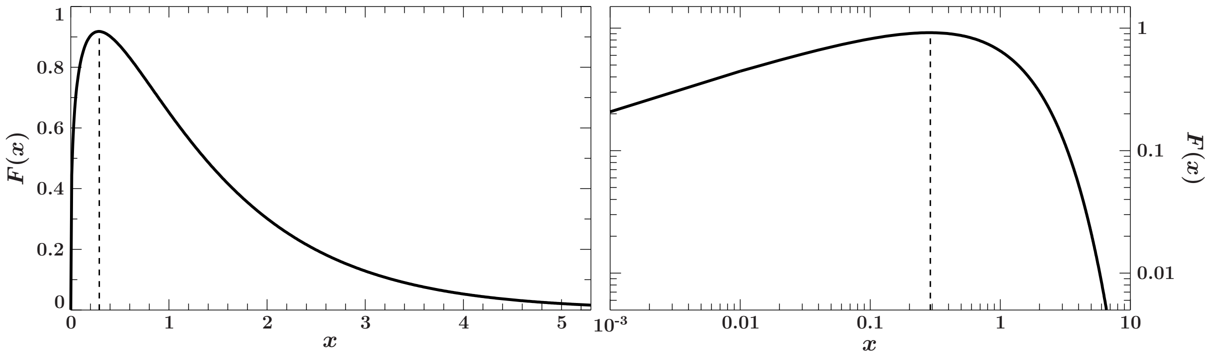

Figure 2.4: $F(x)$ plotted linearly (left) and logarithmically (right). The maximum at $x = 0.29$ is marked with the dashed line.

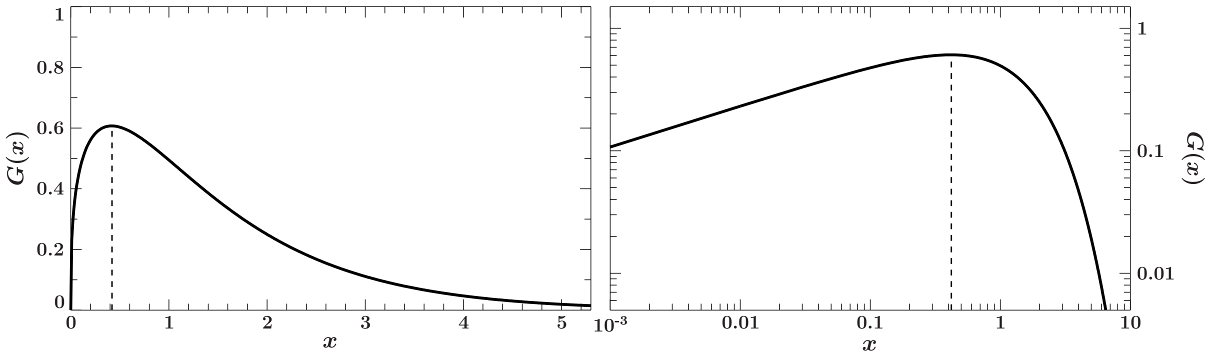

Figure 2.5: $G(x)$ plotted linearly (left) and logarithmically (right). The maximum at $x = 0.42$ is marked with the dashed line.

2.4.2 Absorption coefficient

Not all of the synchrotron emission reaches the observer due to absorption. We can describe the absorption and the stimulated emission by transitions between two energy states E and $E + h\nu$, initiated by photons with energy $h\nu = \hbar kc$. Because photons get created and destroyed during the transitions, we have a constant change in photon numbers and can express the net change of the number density in the momentum space during a unit of time as

$$[B_{21}^{(i)} N(\mathbf{p} + \hbar\mathbf{k}) - B_{12}^{(i)} N(\mathbf{p})]\, I_\nu^{(i)} \tag{2.83}$$

with $B_{21}^{(i)}$ and $B_{21}^{(i)}$ the Einstein coefficients and radiation intensity $I_\nu^{(i)}$ of polarisation (i) and the electron distribution function $N(\mathbf{p})$ in momentum space. From the definition of the intensity we can derive an expression for the absorption coefficient such as

$$\mathrm{d}I = \kappa I \,\mathrm{d}s \quad \Leftrightarrow \quad \kappa_\nu^{(i)} \equiv \frac{1}{I_\nu^{(i)}} \frac{\mathrm{d}I_\nu^{(i)}}{\mathrm{d}s} \tag{2.84}$$

with s being the path length along the line of sight. Knowing the number of photons can be expressed as $N_{ph} = I_\nu / h\nu$ and the definition of the net change (Eq. 2.83), we can write κ as

$$\kappa_\nu^{(i)} = \int [B_{12}^{(i)} N(\mathbf{p}) - B_{21}^{(i)} N(\mathbf{p} + \hbar\mathbf{k})]\, h\nu \,\mathrm{d}\mathbf{p} \quad . \tag{2.85}$$

The probability for photon absorption per unit time is (Lang, 1999)

$$P_{nm} = B_{nm} U_\nu \tag{2.86}$$

with B_{nm} being an Einstein coefficient and U_ν being the energy density which is connected to the brightness B_ν via $U_\nu = 4\pi/c\, B_\nu$. Assuming equilibrium we can use the relation (Lang, 1999)

$$A_{mn} = \frac{8\pi h\nu^3}{c^3} B_{mn} \tag{2.87}$$

from the Einstein correlations originating from the probability definition in Eq. (2.86). As Pacholczyk (1970) uses another definition for the absorption probability, which is $P_{nm} = B_{nm}B_\nu$, the relation of the Einstein correlations becomes

$$B_{12}^{(i)} = B_{21}^{(i)} = A^{(i)} \frac{c^2}{h\nu^3} \quad , \tag{2.88}$$

which differs from Eq. (2.87) by a factor of $c/8\pi$. The difference comes from the relation between U_ν and B_ν and the photon spin factor, which equals 2. Now we can replace $B_{12}^{(i)}$ and $B_{21}^{(i)}$ and write

$$\kappa_\nu = \int [N(\mathbf{p}) - N(\mathbf{p} + \hbar\mathbf{k})] \frac{c^2}{h\nu^3} A^{(i)} h\nu \,\mathrm{d}\mathbf{p} \quad . \tag{2.89}$$

We can express the electron distribution function $N(\mathbf{p})$ in spherical coordinates as $N(p,\theta,\varphi)$ with θ being the azimuthal and φ being the polar angle leading to express $d\mathbf{p}$ as $p^2\,\mathrm{d}p\, d\Omega$. As we can assume an isotropic distribution for the electrons, we know $\int N(p,\theta,\varphi)\,\mathrm{d}\Omega = N(p)$ and can write the absorption coefficient as

$$\kappa_\nu^{(i)} = \frac{1}{4\pi} \int \left[N(p) - N\left(p + \frac{h\nu}{c}\right)\right] \frac{c^2}{\nu^2} \left[\int A^{(i)}\,\mathrm{d}\Omega \right] p^2\,\mathrm{d}p \quad . \tag{2.90}$$

As the momenta of the electrons are very high due to $\beta \approx 1$, we can assume (for the significant transitions) $h\nu/c \ll p$ and therefore write

$$N\left(p + \frac{h\nu}{c}\right) - N(p) \cong \frac{h\nu}{c}\frac{\mathrm{d}N}{\mathrm{d}p} \quad . \tag{2.91}$$

Using this assumption, Eq. (2.90) changes to

$$\kappa_\nu^{(i)} = -\frac{hc}{4\pi\nu} \int p^2 \frac{\mathrm{d}N}{\mathrm{d}p} \left[\int A^{(i)}\,\mathrm{d}\Omega \right] \mathrm{d}p \quad . \tag{2.92}$$

In order to achieve expressing the absorption coefficient in terms of the energy, we take the relation $E = cp$ and rephrase Eq. (2.92) by using

$$N(E)\,\mathrm{d}E = N(p)\,p^2\,\mathrm{d}p \quad , \tag{2.93}$$

which leads to

$$\kappa_\nu^{(i)} = -\frac{hc^2}{4\pi\nu} \int E^2 \frac{\mathrm{d}}{\mathrm{d}E}\left(\frac{N(E)}{E^2}\right) \int A^{(i)}\,\mathrm{d}\Omega\,\mathrm{d}E \quad . \tag{2.94}$$

Because $A^{(i)}$ is the Einstein coefficient for spontaneous emission, it can be associated with $p_{\nu\Omega}^{(i)}$ via

$$\int A^{(i)}\,\mathrm{d}\Omega = \frac{1}{h\nu} \int p_{\nu\Omega}^{(i)}\,\mathrm{d}\Omega = \frac{p_\nu^{(i)}}{h\nu} \tag{2.95}$$

with $p_\nu^{(i)}$ from Eq. (2.80). Finally the whole expression of the absorption coefficient for both polarisations is

$$\kappa_\nu^{(i)} = -\frac{c^2}{8\pi\nu^2} \frac{\sqrt{3}e^3}{mc^2} B \sin\vartheta \int_0^\infty E^2 \frac{\mathrm{d}}{\mathrm{d}E}\left(\frac{N(E)}{E^2}\right) [F(x) \pm G(x)]\,\mathrm{d}E \quad . \tag{2.96}$$

As the total absorption coefficient is defined as $\kappa_\nu = 1/2(\kappa_\nu^{(1)} + \kappa_\nu^{(2)})$, we have

$$\kappa_\nu = -\frac{c^2}{8\pi\nu^2}\frac{\sqrt{3}e^3}{mc^2} B\sin\vartheta \int_0^\infty E^2 \frac{\mathrm{d}}{\mathrm{d}E}\left(\frac{N(E)}{E^2}\right) F(x)\,\mathrm{d}E \quad . \tag{2.97}$$

2.4.3 Radiative transfer

Now that we have an emission and an absorption coefficient, we can combine both physical quantities in the radiative transfer equation, allowing us to calculate the self-absorbed synchrotron spectrum. This subsection's discussion is based on *Radiative Processes in Astrophysics* by Rybicki & Lightman (1979).
The radiative transfer equation is

$$\frac{\mathrm{d}I_\nu}{\mathrm{d}s} = -\kappa_\nu I_\nu + \varepsilon_\nu \quad , \tag{2.98}$$

which describes the change in intensity alongside the travel path of the ray and allows to derive the intensity of a certain radiation in an emitting and absorbing medium. We define the source function S_ν as the ratio of the emission coefficient to the absorption coefficient at frequency ν,

$$S_\nu = \frac{\varepsilon_\nu}{\kappa_\nu} \quad . \tag{2.99}$$

Additionally we substitute the optical depth τ_ν for s by stating

$$\mathrm{d}\tau_\nu = \kappa_\nu \mathrm{d}s \quad . \tag{2.100}$$

Equation 2.98 then becomes

$$\frac{\mathrm{d}I_\nu}{\mathrm{d}\tau_\nu} = -I_\nu + S_\nu \quad . \tag{2.101}$$

The formal solution of the radiative transfer equation is

$$I_\nu(\tau_\nu) = I_\nu(0)\exp(-\tau_\nu) + \int_0^{\tau_\nu} S_\nu \exp(-(\tau_\nu - \tau_\nu'))\,\mathrm{d}\tau_\nu' \quad . \tag{2.102}$$

Assuming no incident radiation ($I_\nu(0) = 0$) and a constant source function S_ν, the analytic solution is

$$I_\nu(\tau_\nu) = S_\nu(1 - \exp(-\tau_\nu)) \quad . \tag{2.103}$$

We can now retrieve the intensity spectrum for any electron distribution, if the emission and the absorption coefficients are known.

2.4.4 Concrete equations for a specific distribution

In the case of AGN we deal with a power-law distribution of electrons, $N(E) = N_0 \cdot E^{-p}$ with N_0 being the constant number density of electrons. In order to derive the whole synchrotron spectrum we need to calculate the concrete emission and absorption coefficients.
The emission for a power-law distribution is given by

$$\varepsilon_\nu = \frac{\sqrt{3}}{4\pi}\frac{e^3}{mc^2} B\sin\vartheta\, N_0 \int_0^\infty E^{-p} F(x)\,\mathrm{d}E \quad . \tag{2.104}$$

In order to solve the integral, it is necessary to express energy E via x. As x is defined as ν/ν_c and ν_c is connected to E, it follows

$$x = \frac{4\pi m^3 c^5 \nu}{B \sin\theta E^2} \quad \Longleftrightarrow \quad E = \sqrt{\frac{4\pi m^3 c^5 \nu}{B \sin\vartheta}}\, x^{-1/2} \quad . \tag{2.105}$$

$\mathrm{d}E$ has to be adapted as well and via calculating $\mathrm{d}E/\mathrm{d}x$ we get

$$\mathrm{d}E = -\frac{1}{2}\sqrt{\left(\frac{4\pi m^3 c^5 \nu}{B \sin\vartheta}\right)}\, x^{-3/2}\,\mathrm{d}x \quad . \tag{2.106}$$

The minus sign is logically correct since the integral limits swap places when integrating over x instead of E. Replacing E and $\mathrm{d}E$, the equation becomes

$$\varepsilon_\nu = \frac{\sqrt{3}}{4\pi}\frac{e^3}{mc^2} B \sin\vartheta \frac{N_0}{2} \int_0^\infty \left(\left(\frac{4\pi m^3 c^5 \nu}{B \sin\vartheta}\right)^{1/2} x^{-1/2}\right)^{-p} F(x) \left(\frac{4\pi m^3 c^5 \nu}{B \sin\vartheta}\right)^{1/2} x^{-3/2}\,\mathrm{d}x \quad . \tag{2.107}$$

After combining the terms appropriately and inserting the true content of $F(x)$, we have

$$\varepsilon_\nu = \frac{\sqrt{3}}{4\pi}\frac{e^3}{mc^2} B \sin\vartheta \frac{N_0}{2} \left(\frac{4\pi m^3 c^5 \nu}{B \sin\vartheta}\right)^{-(p-1)/2} \int_0^\infty x^{(p-1)/2} \int_x^\infty K_{5/3}(z)\,\mathrm{d}z\,\mathrm{d}x \quad . \tag{2.108}$$

Calculating the analytic solution for the integral only, we get, after Westfold (1959),

$$\int_0^\infty x^{(p-1)/2} \int_x^\infty K_{5/3}(z)\,\mathrm{d}z\,\mathrm{d}x = 2^{(p-3)/2}\,\Gamma\left(\frac{3p-1}{12}\right)\Gamma\left(\frac{3p+7}{12}\right)\frac{p+7/3}{p+1} \quad . \tag{2.109}$$

The integral goes over all single monochromatic spectra, which are power-law distributed as well (see Fig. 2.6), because of Eq. (2.105). The final equation giving the complete emission of our initial electron distribution is

$$\varepsilon_\nu = \frac{\sqrt{3} e^3 N_0 (B \sin\vartheta)^{(p+1)/2}}{16\pi mc^2} \left(\frac{2\pi m^3 c^5}{3e}\,\nu\right)^{-(p-1)/2} \frac{p+7/3}{p+1}\,\Gamma\left(\frac{3p-1}{12}\right)\Gamma\left(\frac{3p+7}{12}\right) \quad . \tag{2.110}$$

The absorption for the power-law distribution is given by

$$\kappa_\nu = -\frac{c^2}{2\nu^2}\frac{\sqrt{3}e^3}{4\pi m^3 c^5} B \sin\vartheta \int_0^\infty E^2 \frac{\mathrm{d}}{\mathrm{d}E}\left(\frac{N_0 E^{-p}}{E^2}\right) F(x)\,\mathrm{d}E \quad . \tag{2.111}$$

First we need to perform the derivative, which is

$$\frac{\mathrm{d}}{\mathrm{d}E}\left(\frac{N_0 E^{-p}}{E^2}\right) = -(p+2)\,N_0\,E^{-p-3} \quad , \tag{2.112}$$

then we translate E to x (Eq. 2.105), and finally we can insert the actual meaning of $F(x)$. This results in

$$\kappa_\nu = \frac{c^2}{4\nu^2}\frac{\sqrt{3}e^3 N_0}{4\pi m^3 c^5} (B \sin\vartheta)^{(p+2)/2} (p+2) \left(\frac{4\pi m^3 c^5}{3e}\,\nu\right)^{-p/2} \int_0^\infty x^{p/2} \int_x^\infty K_{5/3}(z)\,\mathrm{d}z\,\mathrm{d}x \quad . \tag{2.113}$$

The integral can be solved in the same way as in Eq. (2.109) with the only difference of having p instead of $p-1$, which gives us

$$\int_0^\infty x^{p/2} \int_x^\infty K_{5/3}(z)\,\mathrm{d}z\,\mathrm{d}x = 2^{(p-2)/2}\,\Gamma\left(\frac{3p+2}{12}\right)\Gamma\left(\frac{3p+10}{12}\right)\frac{p+10/3}{p+2} \quad . \tag{2.114}$$

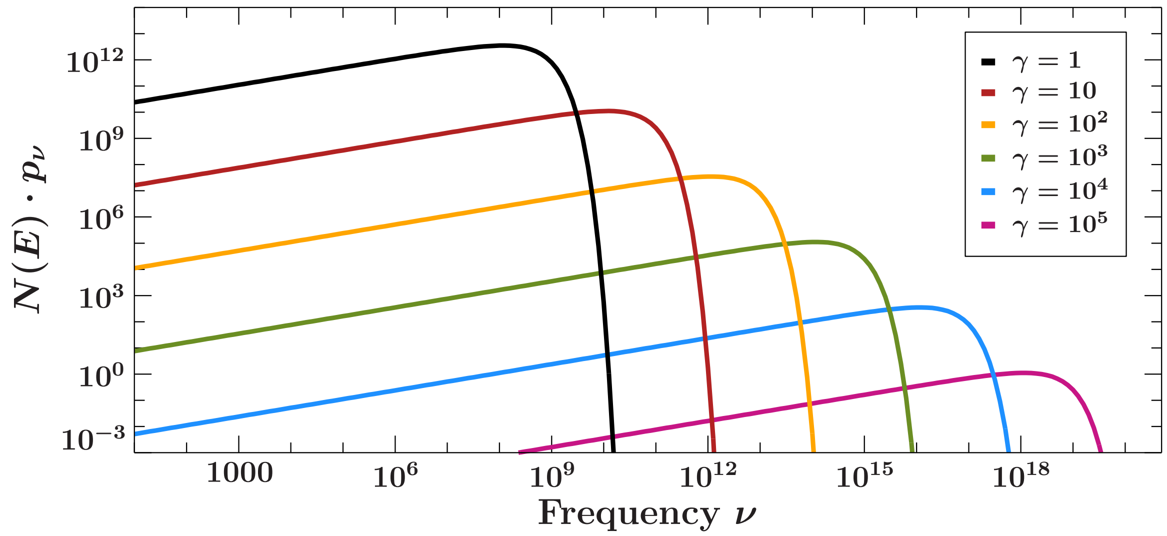

Figure 2.6: Mono-energetic emission spectra for single electrons of a power-law distribution, shown for different different Lorentz factors γ.

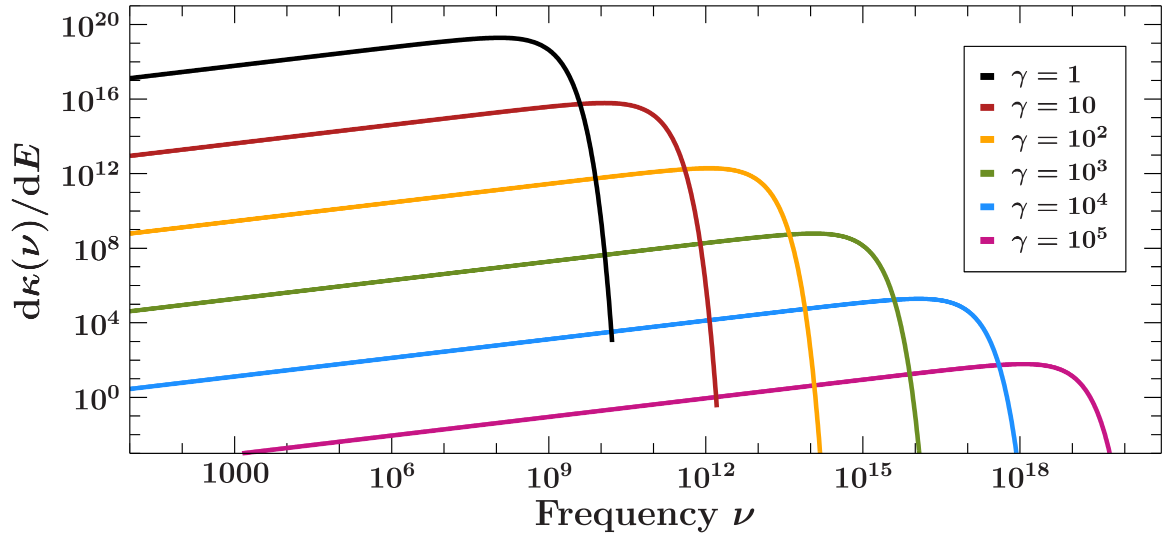

Figure 2.7: Mono-energetic absorption spectra for single electrons of a power-law distribution, shown for different Lorentz factors γ.

The integral again goes over all individual absorption spectra from the electrons of the power-law distribution. Single spectra are shown in Fig. 2.7. In comparison to the emission spectra, one can see that the absorption spectra are steeper, since the range of the y-axis is much larger. The final equation for the complete absorption is

$$\kappa_\nu = \frac{\sqrt{3}e^3}{32\pi m} N_0 \left(B\sin\vartheta\right)^{(p+2)/2} \left(p+\frac{10}{3}\right)\Gamma\left(\frac{3p+2}{12}\right)\Gamma\left(\frac{3p+10}{12}\right)\left(\frac{3e}{2\pi m^3 c^5}\right)^{p/2} \nu^{-(p+4)/2} \quad . \tag{2.115}$$

The source function (Eq. 2.99) needed for deriving the complete spectrum of the electron population, is given by

$$S_\nu = \frac{\varepsilon_\nu}{\kappa_\nu} = \frac{(B\sin\vartheta)^{-1/2}}{c^2}\left(\frac{2\pi m^3 c^5}{3e}\right)^{1/2}\Gamma\left(\frac{3p-1}{12}\right)\Gamma\left(\frac{3p+7}{12}\right)\left(\Gamma\left(\frac{3p+2}{12}\right)\Gamma\left(\frac{3p+10}{12}\right)\right)^{-1}\nu^{5/2}. \tag{2.116}$$

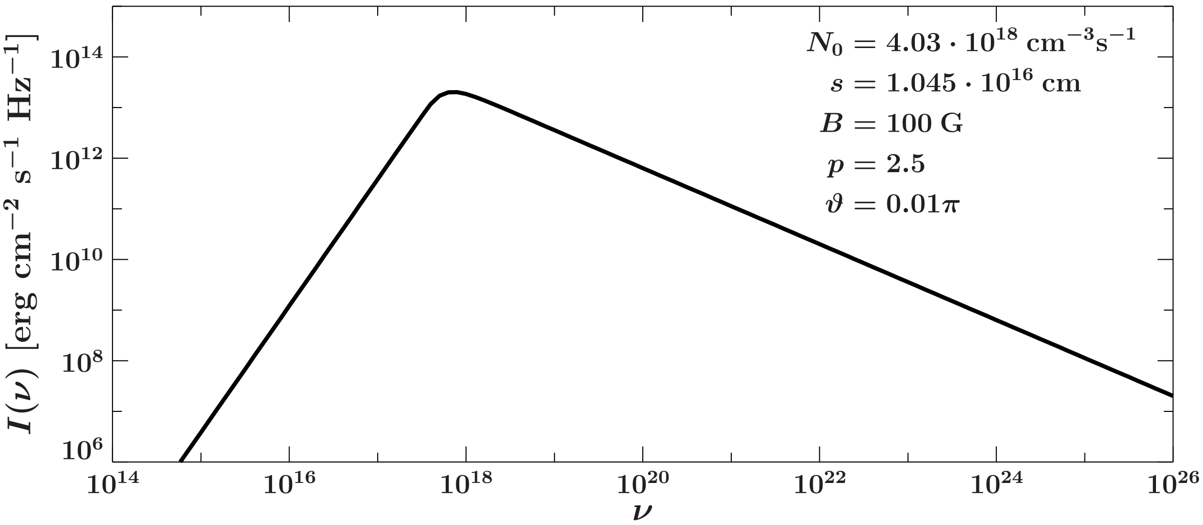

Figure 2.8: Intensity $I(\nu)$ of synchrotron radiation originating at the jet base over Frequency ν.

We can now insert the concrete source function into the formal solution of the radiative transfer equation (Eq. 2.102) and obtain the self-absorbed synchrotron spectrum (see Fig. 2.8). This spectrum shows the intensity of the jet base, which is close to the supermassive black hole. For the calculation, estimations are needed for the parameters N_0, s and B. For a magnetic field B in a jet base, I assumed 100 Gauss after Martí-Vidal et al. (2015), who analysed the Faraday rotation for the AGN PKS 1830 − 211. The size of the jet base of M87 was measured by Doeleman et al. (2012), who derived a size of 5.5 ± 0.4 Schwarzschild radii for the diameter of the jet base. Knowing the approximate mass of the supermassive black hole in M87, Doeleman et al. (2012) computed a Schwarzschild radius of $R_S = (1.9 \pm 0.12) \cdot 10^{15}$ cm, which yields the diameter of the jet base to be $s = 1.045 \cdot 10^{16}$ cm. I used this value for the slab size of the emitting region. In order to estimate the electron density, I assume that 10% of the accreted material gets transfered into the jets, meaning 5% of the material per jet. Using the Bondi accretion rate of $\dot{M} = 0.1 M_\odot\,\mathrm{yr}^{-1}$, we can calculate the number of electrons per volume as

$$N_0 = \frac{0.05\dot{M}}{m_e \cdot A_J \cdot \mathrm{cm}} = \frac{0.05 \cdot 0.1 \cdot M_\odot}{m_e \cdot \pi (2.75 R_S)^2 \cdot \mathrm{cm}} = 4.03 \cdot 10^{18}\,\mathrm{cm}^{-3}\mathrm{s}^{-1} \quad . \tag{2.117}$$

Note that the radius of the jet base is needed to calculate the area of the slice through the jet at this position, which is why we insert $2.75 R_S$. We see in the spectrum (Fig. 2.8) that the peak is in the X-ray regime and no radio emission. This is due to the large magnetic field strength which deflects the moving electrons strongly.

If we go much further out, the magnet field decreases alongside the jet as well as the electron density. However, some regions, so called knots, are especially bright in the radio regime. The calculated intensity spectrum for such a knot is shown in Fig. 2.9. The frame conditions used in this calculation are proposed by Lucchini et al. (2017) for a radio knot in the source B3 0727+490. We see that both spectra cover a broad spectral range. The shape of both spectra is the same, because we took the same value for the slope parameter p for the jet base and the radio knot scenario.

The big difference between both spectra is the position of the peak. While the peak is in the X-ray regime for the spectrum originating at the jet base, the radio knot peaks in the radio regime (see Fig. 2.10 for an overview of the electromagnetic spectrum). We expect this behaviour, because the peak moves to lower frequencies for weaker magnetic fields. The intensity is much lower for

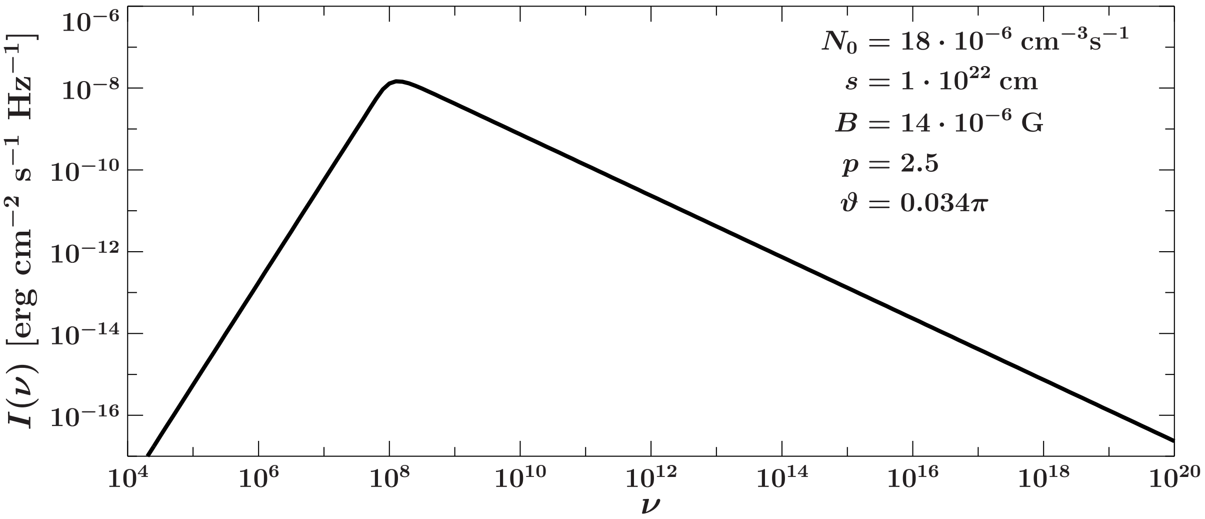

Figure 2.9: Intensity $I(\nu)$ of synchrotron radiation originating in a radio knot over Frequency ν.

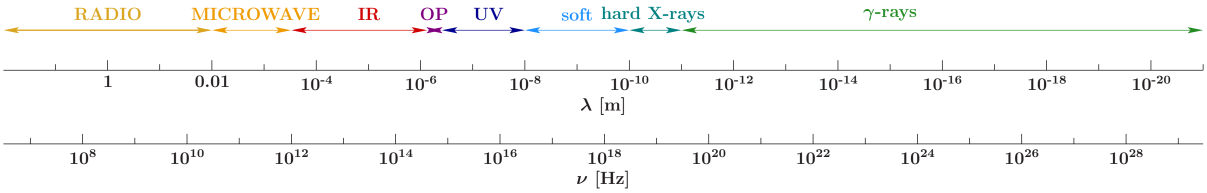

Figure 2.10: Overview over the complete electromagnetic spectrum in wavelength λ and frequency ν. (Plot adapted from F. Krauß & C. Müller.)

the knot spectrum, due to the very small electron density compared to the electron density at the jet base.

For a power-law distribution, we could solve the equations for the emission coefficient ε_ν (Eq. 2.110) and the absorption coefficient κ_ν (Eq. 2.115) analytically. However, other electron distributions might be possible, for which an analytical solution can not be found. Then, a numerical approach is necessary. In Chapt. 3 I will display the difficulties of the numerical calculation and compare the analytically computed emission spectrum with the numerical solution.

2.5 Comparison with other formulae

Many books and articles about the theory of synchrotron radiation are available. It is necessary to compare my results to those and also worth having a look whether they are all in agreement among themselves. Next to Pacholczyk (1970), which I followed in the previous sections, I chose the derivations from Blumenthal & Gould (1970), Padmanabhan (2000), and Rybicki & Lightman (1979), because they are definitive books and keep explicit equations at hand.

2.5.1 Emission coefficient formulae

First I want to compare my derived equation (Eq. 2.110) for the emission coefficient of power-law distributed electrons.

2.5.1.1 Comparison with Pacholczyk

The emission coefficient in Pacholczyk (1970), Eq. 3.50, is given as

$$\varepsilon_\nu = c_5(\gamma)\, N_0\, (H \sin\vartheta)^{(\gamma+1)/2} \left(\frac{\nu}{2c_1}\right)^{(1-\gamma)/2} \tag{2.118}$$

with the constants c_1, introduced in Eq. 3.28, c_3, introduced in Eq. 3.39 and c_5, introduced in Eq. 3.49. The constants are

$$c_1 = \frac{3e}{4\pi m^3 c^5} \quad , \tag{2.119}$$

$$c_3 = \frac{\sqrt{3}}{4\pi}\,\frac{e^3}{mc^2} \quad \text{and} \tag{2.120}$$

$$c_5(\gamma) = \frac{1}{4}\, c_3\, \Gamma\left(\frac{3\gamma-1}{12}\right)\Gamma\left(\frac{3\gamma+7}{12}\right)\cdot\left(\frac{\gamma+7/3}{\gamma+1}\right) \quad . \tag{2.121}$$

If we insert these constants in Eq. (2.118), we obtain

$$\varepsilon_\nu = \frac{\sqrt{3} e^3 N_0 (H\sin\vartheta)^{(\gamma+1)/2}}{16\pi mc^2}\, \frac{\gamma+7/3}{\gamma+1}\, \Gamma\left(\frac{3\gamma-1}{12}\right)\Gamma\left(\frac{3\gamma+7}{12}\right)\left(\frac{2\pi m^3 c^5}{3e}\,\nu\right)^{-(\gamma-1)/2} \quad . \tag{2.122}$$

The equation is the same as my derived Eq. (2.110) apart from two differences. As notation for the magnetic field, Pacholczyk (1970) uses H. I chose to label the magnetic field in all equations as B, because the Lorentz equation is defined with the magnetic field B. Labeling it H could lead to confusion with the magnetising field H. Pacholczyk (1970) also uses a different variable for the exponent in the electron energy spectrum. He introduces the power-law distribution of electrons as $N(E) = N_0 E^{-\gamma}$. I chose to use p instead of γ in order to avoid mistaking the exponent with the Lorentz factor γ.

2.5.1.2 Comparison with Padmanabhan

The equation for the synchrotron emission given by Padmanabhan (2000), Eq. 6.279, is

$$P(\omega)_{\text{tot}} = \frac{\sqrt{3} q^3 C B \sin\alpha}{2\pi mc^2 (p+1)}\, \Gamma\left(\frac{3p-1}{12}\right)\Gamma\left(\frac{3p+19}{12}\right)\left(\frac{m^3 c^5 \omega}{3qB\sin\alpha}\right)^{-(p-1)/2} \quad . \tag{2.123}$$

Padmanabhan (2000) uses slightly different notations for some parameters, so note that q is the electron's charge, C is the constant number density of electrons and α is the inclination angle. Compared to Eq. (2.110), Padmanabhan (2000) calculated the emission spectrum as a function of the angular frequency ω. Since the frequency ν is connected to the angular frequency via $\omega = 2\pi\nu$, we can show that

$$\left(\frac{2\pi m^3 c^5}{3e}\,\nu\right)^{-(p-1)/2} = \left(\frac{m^3 c^5}{3q}\,\omega\right)^{-(p-1)/2} , \tag{2.124}$$

if we replace ω with ν. While I pulled B and $\sin\vartheta$ out of the braket with the exponent $-(p-1)/2$, Padmanabhan (2000) left it in there. One can easily show that

$$B\sin\vartheta \left(\frac{1}{B\sin\vartheta}\right)^{-(p-1)/2} = (B\sin\vartheta)^{(p+1)/2} \quad . \tag{2.125}$$

Additionally, Eq. (2.123) does not include the factor $p + 7/3$, but the argument in one of the two Γ-functions is $(3p + 19)/12$ instead of $(3p + 7)/12$ like in Eq. (2.110). We can show how these are connected and that both equations yield the same, by using $x \cdot \Gamma(x) = \Gamma(x + 1)$:

$$\left(p + \frac{7}{3}\right) \cdot \Gamma\left(\frac{3p+7}{12}\right) = \frac{12}{3}\frac{(3p+7)}{12} \cdot \Gamma\left(\frac{3p+7}{12}\right) = 4 \cdot \Gamma\left(\frac{3p+7}{12} + 1\right) = 4 \cdot \Gamma\left(\frac{3p+19}{12}\right) \quad . \tag{2.126}$$

Applying this equation in Eq. (2.110), we should get the same equation. However, I get a factor of 1/4 in the formula, while Eq. (2.123) shows a factor of 1/2. The reason for this could not be found.

2.5.1.3 Comparison with Rybicki & Lightman

Rybicki & Lightman (1979) show their equation for the total power for power-law distributed electrons in Eq. 6.36, which is

$$P(\omega)_{\text{tot}} = \frac{\sqrt{3} q^3 C B \sin\alpha}{2\pi m c^2 (p+1)} \Gamma\left(\frac{p}{4} + \frac{19}{12}\right) \Gamma\left(\frac{p}{4} - \frac{1}{12}\right) \left(\frac{mc}{3qB\sin\alpha}\,\omega\right)^{-(p-1)/2} . \tag{2.127}$$

The equation resembles Eq. (2.123) very much in terms of parameter nominations and the arguments in the Γ-functions, but there is a main difference in the argument of the bracket with the exponent of $-(p - 1)/2$. While in Eq. (2.110), Eq. (2.118) and Eq. (2.123) we have a factor of m^3c^5, in the equation by Rybicki & Lightman (1979), Eq. (2.127), there is only mc . To explain this, one has to look further back to where the electron distribution is chosen. One can either choose a power-law distribution with the basis being the Lorentz factor γ or the energy E. However, you cannot directly equate $N(E)$ and $N(\gamma)$, but you have to state

$$N(E)\,\mathrm{d}E = N(\gamma)\,\mathrm{d}\gamma \quad \Longleftrightarrow \quad N(E) = N(\gamma)\,\frac{\mathrm{d}\gamma}{\mathrm{d}E} \quad . \tag{2.128}$$

With this equation, we can convert the distributions into one another and we find for a distribution depending on the energy E that

$$\begin{aligned} N(\gamma) &= N_0\,(\gamma m c^2)^{-p}\,\frac{\mathrm{d}}{\mathrm{d}\gamma}(\gamma m c^2) = \\ &= N_0\,(mc^2)^{-p}\,\gamma^{-p}\,mc^2 = \\ &= N_0\,(mc^2)^{1-p}\,\gamma^{-p} \\ &= N_0\,(m^2c^4)^{(1-p)/2}\,\gamma^{-p} \quad . \end{aligned} \tag{2.129}$$

Because Rybicki & Lightman (1979) used $N(\gamma)$ and Padmanabhan (2000), Pacholczyk (1970) and me used $N(E)$, we need to consider Eq. (2.129) in a direct comparison. This means, Eq. (2.127) needs to contain an additional factor of $(m^2c^4)^{(1-p)/2}$, which for the significant part of the equation yields

$$(m^2c^4)^{(1-p)/2}\left(\frac{mc}{3qB\sin\alpha}\,\omega\right)^{-(p-1)/2} = \left(\frac{m^3c^5}{3qB\sin\alpha}\,\omega\right)^{-(p-1)/2} . \tag{2.130}$$

Already being noticed in the previous comparison with Padmanabhan (2000), we find a pre-factor of 1/2 instead of 1/4 in Eq. (2.110) and Eq. (2.118).

2.5.1.4 Comparison with Blumenthal & Gould

Another concrete equation for the synchrotron emission, given by Blumenthal & Gould (1970), Eq. 4.58, is

$$\frac{\mathrm{d}W}{\mathrm{d}\nu\mathrm{d}t} = \frac{\sqrt{3}ke^3B}{4\pi mc^2(p+1)}\Gamma\left(\frac{3p-1}{12}\right)\Gamma\left(\frac{3p+19}{12}\right)\left(\frac{2\pi mc}{3eB\sin\alpha}\,\nu\right)^{-(p-1)/2}\int N(\alpha)(\sin\alpha)^{(p+1)/2}\,\mathrm{d}\Omega_\alpha . \tag{2.131}$$

Note that k marks the constant number density of electrons. Since they use an electron distribution dependent on γ, similar to Rybicki & Lightman (1979), the pre-factor of $(m^2c^4)^{(1-p)/2}$ has to be considered in a comparison with Eq. (2.110). They derive also a factor of 1/2 more, compared to Rybicki & Lightman (1979) and Padmanabhan (2000).
Equation 2.131 by Blumenthal & Gould (1970) includes an integral over the pitch angle and differs from the other equations in that way. The reason for this is that they integrate over the complete solid angle for the pitch angle, while the others make the same assumption described in Eq. (2.74). The assumption relates to the fact that most of the emission is confined into a small angled cone and the integration over the pitch angle can be limited to a ring (see shaded ring in Fig. 2.2).

2.5.2 Absorption coefficient formulae

After we compared the solutions for the synchrotron emission of a power-law distribution of electrons, we also take a look at the equations for the absorption of such a distribution. We will compare my result in Eq. (2.115) with equations from the same authors as in the previous section, namely Pacholczyk (1970),Blumenthal & Gould (1970), Padmanabhan (2000), and Rybicki & Lightman (1979).

2.5.2.1 Comparison with Pacholczyk

The average absorption coefficient by Pacholczyk (1970), Eq. 3.52, is

$$\kappa_\nu = c_6(\gamma)\, N_0\, (H\sin\vartheta)^{(\gamma+2)/2}\left(\frac{\nu}{2c_1}\right)^{-(\gamma+4)/2} \tag{2.132}$$

with the constants c_1, introduced in Eq. 3.28, c_3, introduced in Eq. 3.39 and c_5, introduced in Eq. 3.51. The constants are

$$c_1 = \frac{3e}{4\pi m^3c^5} \quad , \tag{2.133}$$

$$c_3 = \frac{\sqrt{3}}{4\pi}\frac{e^3}{mc^2} \quad \text{and} \tag{2.134}$$

$$c_6(\gamma) = \frac{1}{32}\left(\frac{c}{c_1}\right)^2 c_3\left(\gamma+\frac{10}{3}\right)\Gamma\left(\frac{3\gamma+2}{12}\right)\Gamma\left(\frac{3\gamma+10}{12}\right) \quad . \tag{2.135}$$

If we insert these constants in Eq. (2.118), we obtain

$$\kappa_\nu = \frac{\sqrt{3}e^3}{32\pi m}N_0\,(H\sin\vartheta)^{(p+2)/2}\left(p+\frac{10}{3}\right)\Gamma\left(\frac{3p+2}{12}\right)\Gamma\left(\frac{3p+10}{12}\right)\left(\frac{3e}{2\pi m^3c^5}\right)^{p/2}\nu^{-(p+4)/2} \tag{2.136}$$

The notation differences for H/B and γ/p have already been discussed in Sect. 2.5.1.1. Equation 2.136 agrees with Eq. (2.115).

2.5.2.2 Comparison with Padmanabhan

Padmanabhan (2000) does not give a concrete equation for the synchrotron absorption coefficient, which they call α_ν. Instead, he derives the proportionality of the frequency ν in Eq. 6.293 as

$$\alpha_\nu \propto \frac{1}{\nu^2} \int \frac{\mathrm{d}\mathcal{E}}{\mathcal{E}} N(\mathcal{E})\, F(\nu/\mathcal{E}) \propto \frac{1}{\nu^2} \int \frac{\mathrm{d}x}{x} \left(\frac{\nu}{x}\right)^{p/2} F(x) \propto \nu^{-\frac{1}{2}(p+4)} \quad . \tag{2.137}$$

From that, we can only conclude, that Padmanabhan (2000) and Eq. (2.110) concur in the exponent of the Frequency ν.

2.5.2.3 Comparison with Rybicki & Lightman

The absorption coefficient given by Rybicki & Lightman (1979), Eq. 6.53, is

$$\alpha_\nu = \frac{\sqrt{3}q^3}{8\pi m} \left(\frac{3q}{2\pi m^3 c^5}\right)^{p/2} C\,(B \sin\alpha)^{(p+2)/2}\, \Gamma\left(\frac{3p+2}{12}\right) \Gamma\left(\frac{3p+22}{12}\right) \nu^{-(p+4)/2}. \tag{2.138}$$

In order to show that Eq. (2.115) and Eq. (2.138) are the same, we can again use $x \cdot \Gamma(x) = \Gamma(x+1)$ and show that

$$\left(p + \frac{10}{3}\right) \cdot \Gamma\left(\frac{3p+10}{12}\right) = \frac{12}{3} \frac{(3p+10)}{12} \cdot \Gamma\left(\frac{3p+10}{12}\right) = 4 \cdot \Gamma\left(\frac{3p+10}{12} + 1\right) = 4 \cdot \Gamma\left(\frac{3p+22}{12}\right) \quad . \tag{2.139}$$

Applying this on Eq. (2.115), the factor becomes 1/8 and we can see, that Eq. (2.138) and Eq. (2.115) are the same, since the notation differences for C/N_0, q/e, and α/ϑ have already been discussed in Sect. 2.5.1.3.

2.5.2.4 Comparison with Blumenthal & Gould

Blumenthal & Gould (1970) do not derive the synchrotron absorption in their paper.

2.5.3 Conclusions

The direct comparison shows that the equations derived by Blumenthal & Gould (1970), Padmanabhan (2000), Pacholczyk (1970), and Rybicki & Lightman (1979) are in accordance with each other, apart from a factor of 1/2, which is present for the emission equations by Pacholczyk (1970), Blumenthal & Gould (1970), and the equation I derived in this chapter.

Chapter 3 Numerical integration problems

In the previous chapter, we only calculated synchrotron spectra for powerlaw distributed electrons (Sect. 2.4.4). If another distribution is assumed, there might not exist an analytic solution and a numerical approach must be used. Since the analytic solution of synchrotron radiation is known for a powerlaw distribution, we can use the analytical and the numerical calculation for a comparison, in order to check whether both are in agreement. In this chapter, I will show the difficulties in the numerical calculation for synchrotron spectra and compare the analytically computed emission spectrum with the numerical solution. Calculations are performed by routines written in C. The GNU Scientific Library[1] (GSL) is used for specific functions, e.g., the Bessel functions, and the numerical methods.

3.1 Integration limits

Numerical integration is needed whenever we have a function or a curve, whose integral we want to know, but can not determine the antiderivative. The integration tool I used in my work is the QAG adaptive integration[2], which divides the integration region into subintervals and in each step bisects the subintervals with the largest estimated error. Consequently, the subintervals are not equidistant, but allocate around local difficulties in the integrand.

Synchrotron radiation is emitted on a very broad spectral range, that is over several magnitudes, which causes problems in the numerical integration. The integration has to be executed over all single monoenergetic electron spectra, meaning from spectra of electrons with minimum energy ($\gamma = 1$) to ultrarelativistic electrons ($\gamma \gg 1$). Figure 3.1 shows numerically calculated emission spectra for different upper integration limits in γ. What we can see there is a sudden drop in the spectra which shifts to higher frequencies with increasing integration limit. This seems plausible, because if we only include electrons, e.g., with $\gamma \leq 10^3$ in the integral, the integration tool ignores all monoenergetic spectra with greater Lorentz factors and the spectrum drops to zero.

---

[1] https://www.gnu.org/software/gsl/

[2] https://www.gnu.org/software/gsl/manual/html_node/QAG-adaptive-integration.html#QAG-adaptive-integration

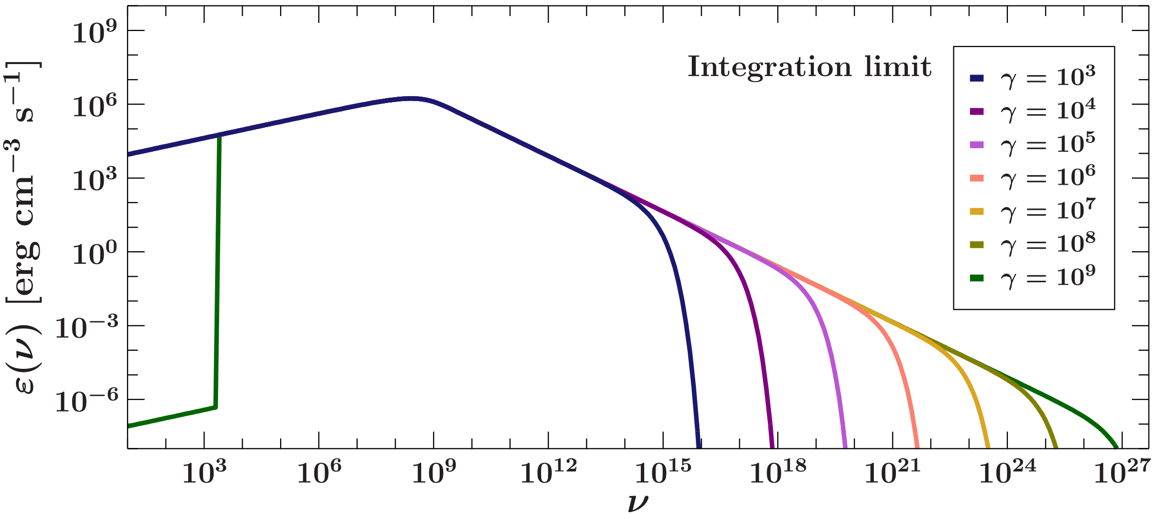

Figure 3.1: Emission spectra with different integration limits. These spectra were calculated using Eq. (2.104) and the parameter values of $N_0 = 4.03 \cdot 10^{18}\,\mathrm{cm}^{-3}\mathrm{s}^{-1}$, $B = 100\,\mathrm{Gs}$, $p = 2.5$, and $\vartheta = 0.1\pi$.

Another problem becomes visible for the integration up to very high Lorentz factors. Setting the upper limit to $\gamma = 10^9$, we can observe a kink at around $\nu = 10^3$ Hz. This feature occurs due to a limitation in the number of subintervals. A solution to this problem can be a logarithmic ν-scale in the equation, which minimises the broad spectral range, but is not easily conducted for all equations.

3.2 Difference between analytical and numerical solution

Plotting the numerically and analytically calculated emission spectra together reveals some differences, see Fig. 3.2. First, we see the analytic approximation continuing as a powerlaw when we go from high to low frequencies. The numerical result for the chosen set of parameters, however, has a maximum at around 10^9 Hz and the spectrum decreases again for lower frequencies. The reason for the different behaviour is that the analytic approximation does not take into account that there is a minimum electron energy, respectively a minimum Lorentz factor $\gamma = 1$. What we see as a maximum in the numerical solution coincides with the peak of the monoenergetic spectrum with $\gamma = 1$. For the low frequency range, the analytical approximation is therefore not correct.
Additionally, for frequencies $\nu > 10^9$ Hz, the analytic approximation and the numerical result do not unite, but there an offset of $\varepsilon_{\mathrm{ana}}/\varepsilon_{\mathrm{num}} = 0.424$ is present. The reason for this is not clear yet.

3.3 Integration over distributed energy spectra

Another numerical problem occurs if we take our integrated emission spectrum and plot it over all single monoenergetic spectra of the powerlaw distribution. We expect the single spectra to be covered by the complete spectrum, but we actually observe the spectrum for the lowest energetic electrons to be above the total spectrum, see Fig. 3.3. The reason for this is not clear yet.

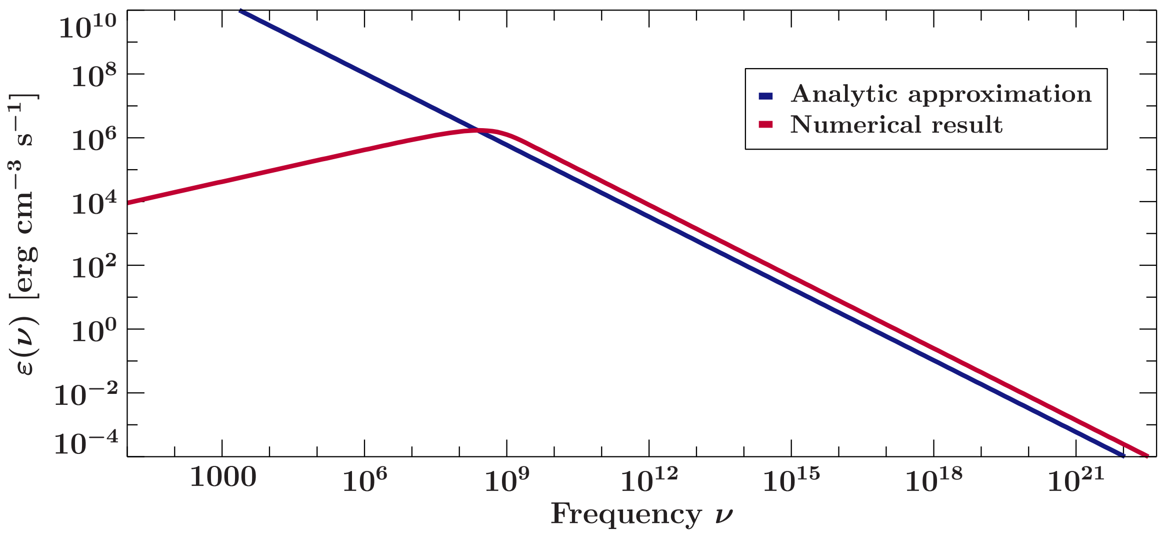

Figure 3.2: Comparison of numeric and analytic solution for the emission coefficent. The spectra were calculated using Eq. (2.110) for the analytical approximation and Eq. (2.104) for the numerical result. The parameter values are $N_0 = 4.03 \cdot 10^{18}$ cm^{-3}s^{-1}, $B = 100$ Gs, $p = 2.5$, and $\vartheta = 0.1\pi$.

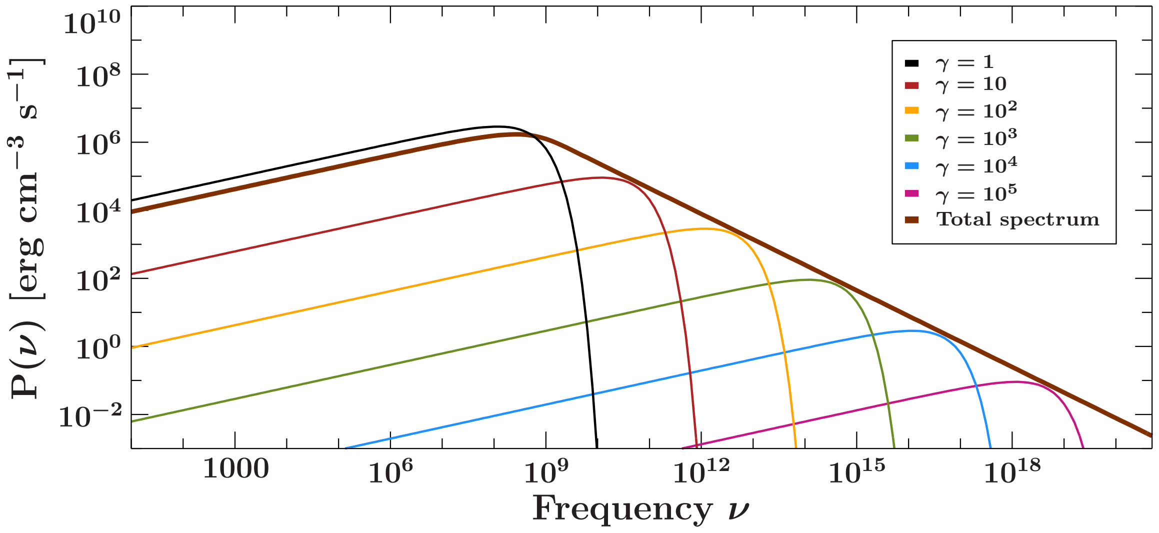

Figure 3.3: Integrated emission spectrum over the distributed monoenergetic spectra. For the integrated emission spectrum Eq. (2.104) was used. The parameter values are $N_0 = 4.03 \cdot 10^{18}$ cm^{-3}s^{-1}, $B = 100$ Gs, $p = 2.5$, and $\vartheta = 0.1\pi$.

3.4 Intensity spectrum

Calculating the self-absorbed synchrotron spectrum, one can solve the equation for the intensity (Eq. 2.102) analytically in case of a constant source function S_ν. Otherwise a numerical integration is necessary. When I derived the intensity spectrum both ways, I found that the analytical approach fails at high frequencies $\nu > 10^{19}$ Hz and the numerical approach at low frequencies $\nu < 10^{13}$ Hz for the chosen parameters. The spectra are shown in Fig. 3.4 and Fig. 3.5. The reason for the weird feature at $\nu = 10^{19}$ Hz in the analytically computed spectrum is still unsettled. The sudden drop to zero at $\nu = 10^{13}$ Hz in the numerically computed spectrum is probably due to

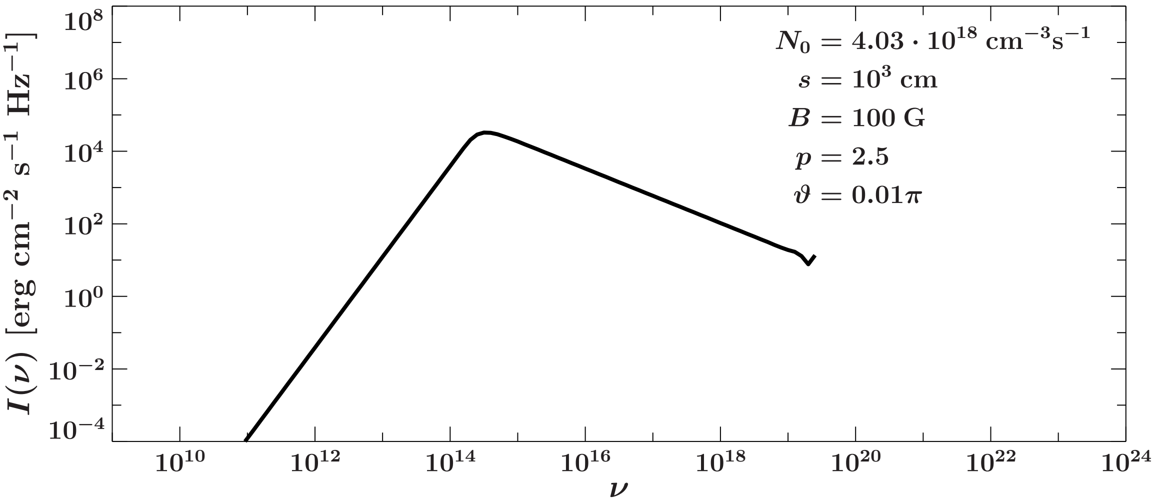

Figure 3.4: Analytically calculated intensity spectrum using Eq. (2.103).

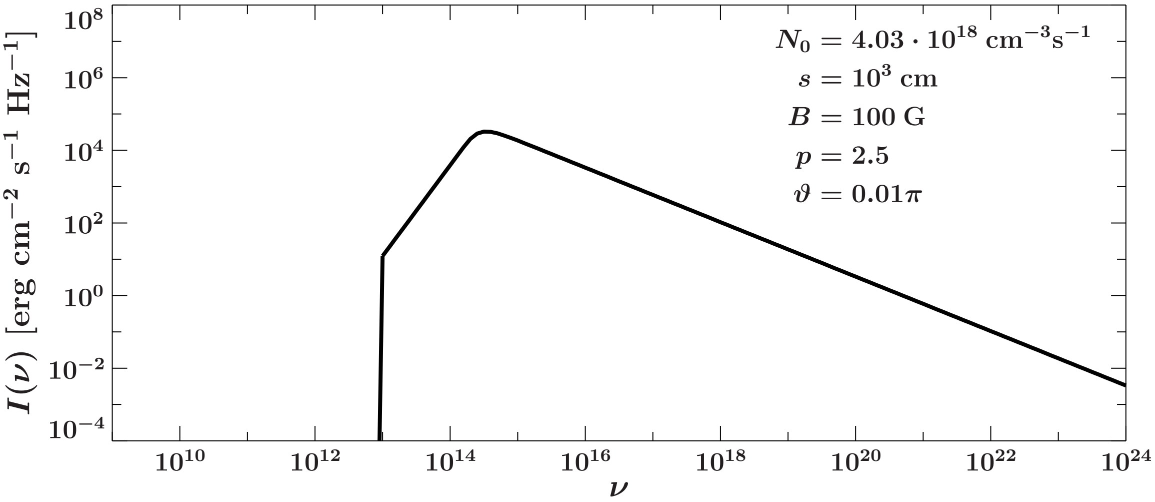

Figure 3.5: Numerically calculated intensity spectrum using Eq. (2.102).

the very small integrand $\exp(-(\tau_\nu - \tau'_\nu))$.

3.5 Other integrators

In the GSL, other numerical integrators are available next to the QAG algorithm. Several integrators are written for specific cases, e.g., singularities, infinite intervals, or oscillatory functions. A non-adaptive integrator is included in the GSL as well, but provides inferior results. The main problem for the numerical integration is probably the large orders of magnitude on the x range, which could be solved by adapting the equation in such a way that it is dependent on $\log\nu$ rather than ν.

Chapter

4 Systematic study of simultaneous observations of AGN by *XMM-Newton* and *NuSTAR*

4.1 Introduction

Performing simultaneous observations with different satellites allows us to study energetic sources like X-ray binaries or active galactic nuclei (AGN) in a broader emission regime. As radiation is rarely confined to only a small emission range, we can get better insights in the behaviour of those sources by combining data from all over the spectrum. When studying accreting objects in the X-rays, emission features in the region of the iron K α line (6.4 keV) are important for the analysis of relativistic line broadening near black hole systems. However, good results can only be found when the underlying continuum is well known which requires knowledge about the spectrum in the hard X-rays. Additionally, relativistic reflection effects which range from the lowest energies (1 keV) up to the Compton hump (30 keV) cannot be observed with only one instrument so far. Simultaneous observations in different energy ranges therefore improve the study of energetic sources, variable sources in particular. In order to gain good and reliable results from a simultaneous observation it is necessary to have a very good cross-calibration between the involved satellites. Since a perfect calibration is not possible to achieve, calibration uncertainties introduce discrepancies in the data analysis and impact the determination of astrophysical values. The aim of the work presented in this chapter was to help improving the cross-calibration between *XMM-Newton* and *NuSTAR* by analyzing as many simultaneously performed observations of AGN as there were publicly available at the end of June 2016. This work was a project performed at the European Space Astronomy Center (ESAC) under the supervision of Norbert Schartel and Maria Santos-Lleo.

4.2 The satellites *XMM-Newton* and *NuSTAR*

The X-ray satellite *XMM-Newton* (Jansen et al., 2001) was launched by the European Space Agency (ESA) in 1999. It observes soft X-rays in an energy range from 0.2 to 12 keV with two Reflection Grating Spectrometers (RGSs) and three European Photon Imaging Cameras

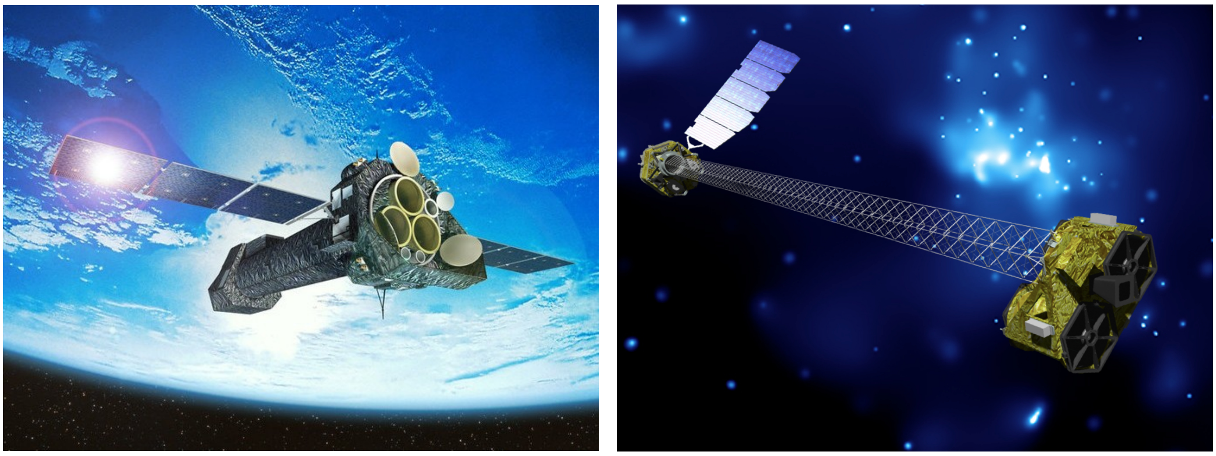

(a) *XMM-Newton* ©ESA - D. Ducros (www.esa.int)

(b) *NuSTAR* ©NASA/JPL-Caltech (www.jpl.nasa.gov)

Figure 4.1: The satellites *XMM-Newton* and *NuSTAR*

(EPICs), namely MOS-1, MOS-2 and PN, which are each at the end of one Wolter type 1 telescope. Additionally, there is an Optical Monitor (OM), a 30 cm mirror telescope, which allows simultaneous observations of an X-ray source in the optical and UV range.

NASA's *Nuclear Spectroscopic Telescope Array* (*NuSTAR*; Harrison et al., 2013) launched in 2012, is the first focusing high-energy instrument in space and observes an energy range from 3 to 79 keV. It has two semiconductor detectors, the Focal Plane Modules A and B (FPMA, FPMB), on which the hard X-rays are focused by using Wolter type 1 approximation optics. Artist's impressions of the satellites in space are shown in Fig. 4.1a and Fig. 4.1b. The main advantage for combining *XMM-Newton* and *NuSTAR* in simultaneous observations is their observational energy overlap between 3 and 12 keV (see Fig. 4.2) which allows for direct comparison of the spacecrafts' calibrations. The instruments of the spacecrafts used in this analysis were the EPIC-pn of *XMM-Newton* and FPMA and FPMB of *NuSTAR*. Since it is necessary to have a good Signal-to-Noise Ratio (S/N) X-ray spectrum, some observations had to be neglected from the available sample. The final data set includes 16 observations from 10 sources (see Table 4.1).

4.3 Data

4.3.1 Extraction

The data was extracted with the standard pipelines. The observations by *XMM-Newton* were extracted using *XMM-Newton* Science Analysis System (SAS) version 15.0.0 aiming to achieve a maximum S/N. Data from the *NuSTAR* spacecraft was extracted using the *NuSTAR* Data Analysis Software (NUSTARDAS) package (v.1.4.1), using nupipeline and the calibration database CALDB20150316 for creating cleaned and calibrated data products. In order to create strictly simultaneous observational data, we used the FTOOL mgtime to merge the gti-files from the observations of both spacecrafts into a common one which was then applied to all observations presented here. All spectra have been binned for a higher S/N ratio. While for the EPIC-pn spectra we used a constant S/N ratio factor of 10 for binning, for the FPM spectra we constantly binned 10 channels together. The complete data set used in this work is given in Table 4.1.

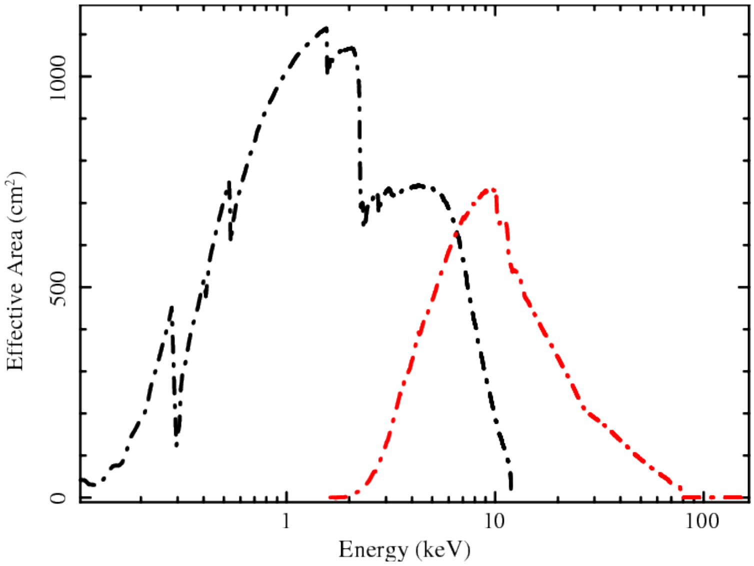

Figure 4.2: Comparison of the effective areas of *XMM-Newton* EPIC-pn camera (black) and *NuSTAR* FPMA (red)

4.3.2 Data Analysis

All spectra were analysed with xspec 12.8.2 using the `wilm` abundances (Wilms et al., 2000) and the `vern` cross sections (Verner et al., 1996). Two different approaches were used to gather information about the differences in the *XMM-Newton* and the *NuSTAR* calibration.

Method 1 includes fitting an EPIC-pn spectrum with a physical model, then applying the model without further change of the parameters to the *NuSTAR* data in order to compare how well the model for the *XMM-Newton* data fits to the *NuSTAR* spectrum.

Method 2 involves simultaneously fitting spectra from EPIC-pn and FPMA/FPMB, respectively, from 3 to 10 keV and retrieving a cross-normalisation constant as well as differences in the power-law indices of the best fit. All errors are 90% confidence unless stated otherwise.

4.3.2.1 Method 1: Comparison of ratios

In Method 1 the ratio of data points to a model are used. The first step is finding a physical, well fitting model for the *XMM-Newton* spectrum. This model is then applied to the *NuSTAR* spectrum without fitting the model again. The comparison of the *NuSTAR* data with the model is done by the ratios, which are directly obtained from xspec.

Whether the observation of a source was used for this method can be seen in the column *Method* of Table 4.1. The applied physical models for each source are given in Table 4.2. Each model contains a power-law (`pegpwrlw` or `bknpower` for a broken power-law). For galactic absorption we used `tbnew_feo`[1] a simple version of the new version of `tbabs` (Wilms et al., 2000). For a source showing relativistic reflection, we applied the `relxill` model (García et al., 2014). `relxill` includes a primary spectrum, which originates in a corona surrounding the accretion disc and is also a power-law, as well as it takes into account the reflection onto the accretion disc. In that way, we can see relativistically broadened emission lines, particularly the iron K α line. In case of the presence of a warm absorber or an extensive soft excess in the spectra, we included the model `warmabs` or a simple blackbody (`bbody`), respectively.

---

[1] http://pulsar.sternwarte.uni-erlangen.de/wilms/research/tbabs/

Source	Instrument	ObsID	Start Time	End Time	Method
3C 120	EPIC-pn	0693781601	2013-02-06 12:39	2013-02-08 00:51	1, 2
	FPM	60001042002	2013-02-06 12:46	2013-02-06 23:51	1, 2
3C 273	EPIC-pn	0414191001	2012-07-16 11:59	2012-07-16 22:48	1, 2
	FPM	10002020001	2012-07-14 00:06	2012-07-19 23:36	1, 2
Ark 120	EPIC-pn	0693781501	2013-02-18 11:40	2013-02-19 23:54	1, 2
	FPM	60001044002	2013-02-18 10:46	2013-02-20 09:36	1, 2
Centaurus A	EPIC-pn	0724060601	2013-08-07 12:27	2013-08-07 15:47	2
	FPM	60001081002	2013-08-06 13:01	2013-08-07 16:06	2
Fairall 9	EPIC-pn	0741330101	2014-05-09 02:20	2014-05-10 17:37	1, 2
	FPM	60001130002	2014-05-09 02:16	2014-05-09 23:01	1, 2
		60001130003	2014-05-09 23:01	2014-05-11 15:26	1
HE 1136-2304	EPIC-pn	0741260101	2014-07-02 07:44	2014-07-03 14:24	1, 2
	FPM	80002031002	2014-07-02 08:16	2014-07-02 22:31	1, 2
		80002031003	2014-07-02 22:31	2014-07-04 10:01	1, 2
MCG-6-30-15	EPIC-pn	0693781201	2013-01-29 12:08	2013-01-31 01:25	1, 2
	FPM	60001047002	2013-01-29 11:16	2013-01-30 00:11	1, 2
	EPIC-pn	0693781301	2013-01-31 12:01	2013-02-02 01:18	1, 2
	FPM	60001047003	2013-01-30 00:11	2013-02-02 00:41	1, 2
	EPIC-pn	0693781401	2013-02-02 12:02	2013-02-03 01:37	1, 2
	FPM	60001047005	2013-02-02 10:51	2013-02-03 02:41	1, 2
Mrk 915	EPIC-pn	0744490401	2014-12-02 13:08	2014-12-04 02:38	1, 2
	FPM	60002060002	2014-12-02 13:56	2014-12-03 18:46	1, 2
	EPIC-pn	0744490501	2014-12-07 07:46	2014-12-08 03:01	1
	FPM	60002060004	2014-12-07 06:51	2014-12-08 12:46	1
NGC 4593	EPIC-pn	0740920401	2015-01-02 04:46	2015-01-02 11:59	1
	FPM	60001149006	2015-01-02 03:21	2015-01-02 16:36	1
	EPIC-pn	0740920601	2015-01-06 15:01	2015-01-06 23:52	1, 2
	FPM	60001149010	2015-01-06 15:26	2015-01-07 02:31	1, 2
Swift J2127.4+5654	EPIC-pn	0693781701	2012-11-04 17:34	2012-11-06 07:12	1, 2
	FPM	60001110002	2012-11-04 17:21	2012-11-05 18:06	1, 2
		60001110003	2012-11-05 18:06	2012-11-06 08:01	1, 2
	EPIC-pn	0693781801	2012-11-06 17:26	2012-11-08 07:04	1, 2
	FPM	60001110005	2012-11-06 17:56	2012-11-08 07:06	1, 2
	EPIC-pn	0693781901	2012-11-08 17:18	2012-11-09 13:17	1, 2
	FPM	60001110007	2012-11-08 16:51	2012-11-09 13:41	1, 2

Table 4.1: All observations included in the data sample. The spectra were studied using two different methods; the column Method shows whether a source was included in both analysation methods or just one.

As an example, simultaneous spectra from EPIC-pn, FPMA and FPMB are shown in Fig. 4.3 (Ark 120) and Fig. 4.4 (Swift J2127.4+5654). For all models the *NuSTAR* spectra show discrepancies, since the models were fitted to data from the *XMM-Newton* satellite. This approach allows comparing the difference between both spacecrafts indirectly by looking at the ratios. Note that the comparison between EPIC-pn and the FPM detectors does not allow to make a statement about the correlation between the MOS and the FPM detectors. In the ratio plots a slope is visible (e.g. see Fig. 4.3 and Fig. 4.4), causing the FPMA/FPMB values to be higher than the values of EPIC-pn up to 7 keV.

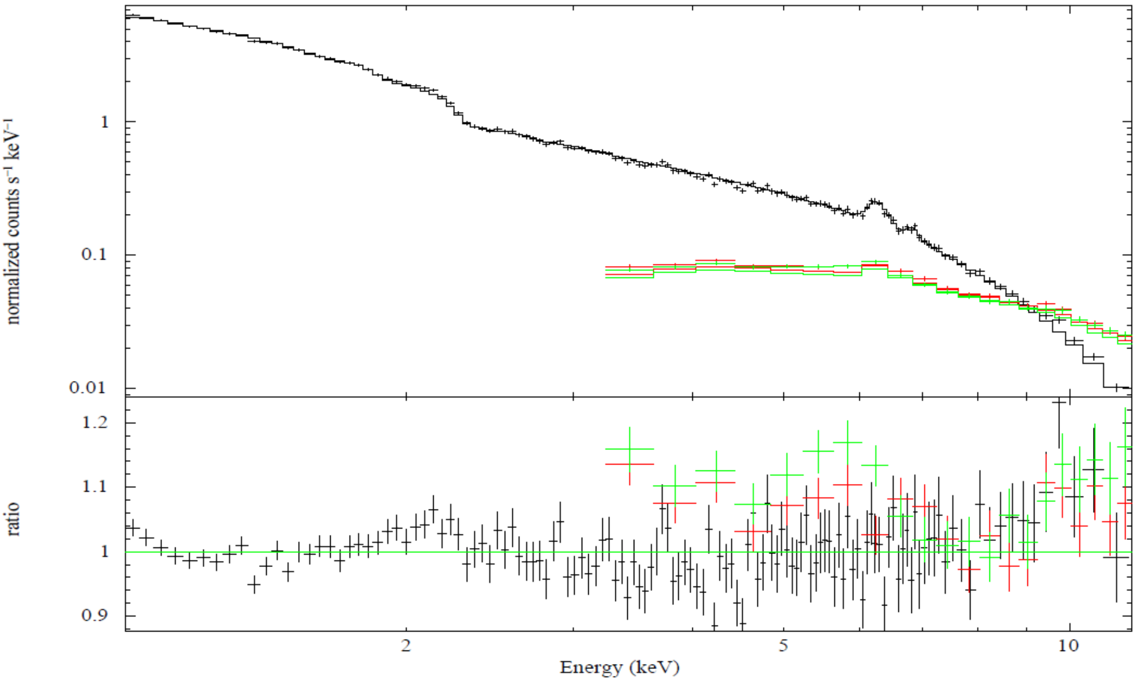

Figure 4.3: Fitted EPIC-pn spectrum (black) of Ark 120 with spectra from both detectors of *NuSTAR* (FPMA: red, FPMB: green) in the upper window. In the lower window ratio values for model vs. data are given for each spectrum.

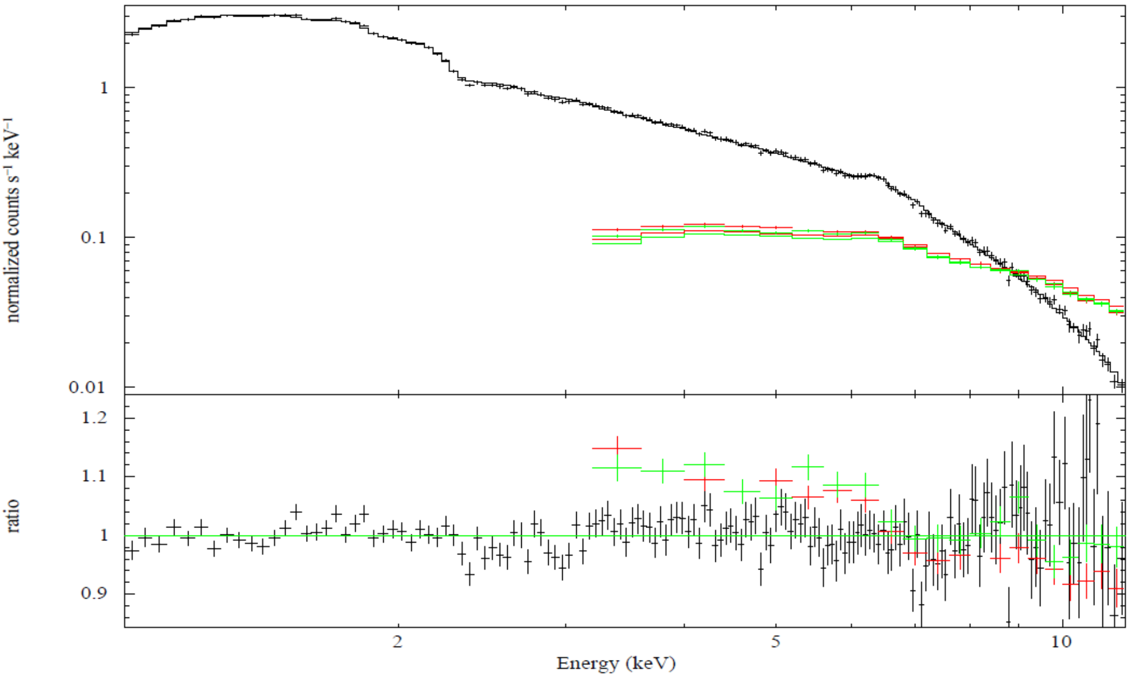

Figure 4.4: Fitted EPIC-pn spectrum (black) of Swift J2127.4+5654 with spectra from both detectors of *NuSTAR* (FPMA: red, FPMB: green) in the upper window. In the lower window ratio values for model vs. data are given for each spectrum.

Source	Model	Reference
3C 120	tbnew_feo×(relxill+zgauss+zgauss)	Lohfink et al. (2013)
3C 273	tbnew_feo×bknpower	Stuhlinger et al. (2004)
Ark 120	tbnew_feo×(bbody+relxill+zgauss+zgauss)	Matt et al. (2014)
Centaurus A	tbnew_feo×(pegpwrlw+zgauss)	Fürst et al. (2016)
Fairall 9	relxill+zgauss	Lohfink et al. (2012)
HE 1136-2304	tbnew_feo×(relxill+zgauss)	Parker et al. (2016)
MCG-6-30-15	tbnew_feo×warmabs(relxill+zgauss)	Wilms et al. (2001)
Mrk 915	warmabs×tbnew_feo×(relxill+zgauss)	Severgnini et al. (2015)
NGC 4593	tbnew_feo×(pegpwrlw+zgauss+zgauss)	Brenneman et al. (2007)
Swift J2127.4+5654	tbnew_feo×(bbody+relxill+zgauss)	Marinucci et al. (2014)

Table 4.2: Models applied on EPIC-pn spectra in Method 1

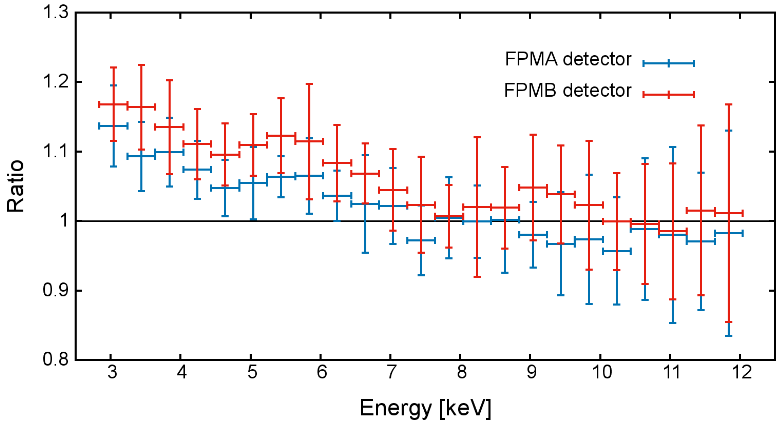

(a) Mean ratio values

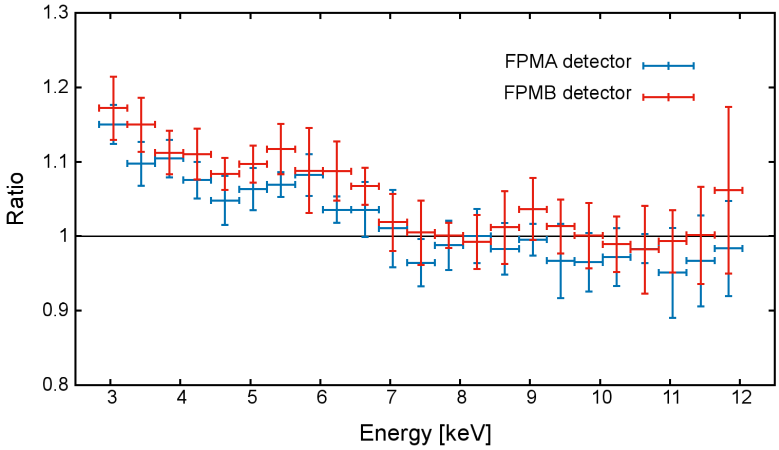

(b) Median ratio values

Figure 4.5: Ratios from FPM spectra compared to best fit to EPIC-pn spectra

In order to get rid of systematics caused by the different models and sources, and to see whether this slope is present in all spectra, we merged all of the ratio plots together in one plot. Figure 4.5a shows the calculated mean values with the according standard deviation, while Fig. 4.5b shows the median with the median absolute deviation. In both plots the ratios unveil deviations between the FPM spectra and the model in the energy range from 3 to 7 keV.

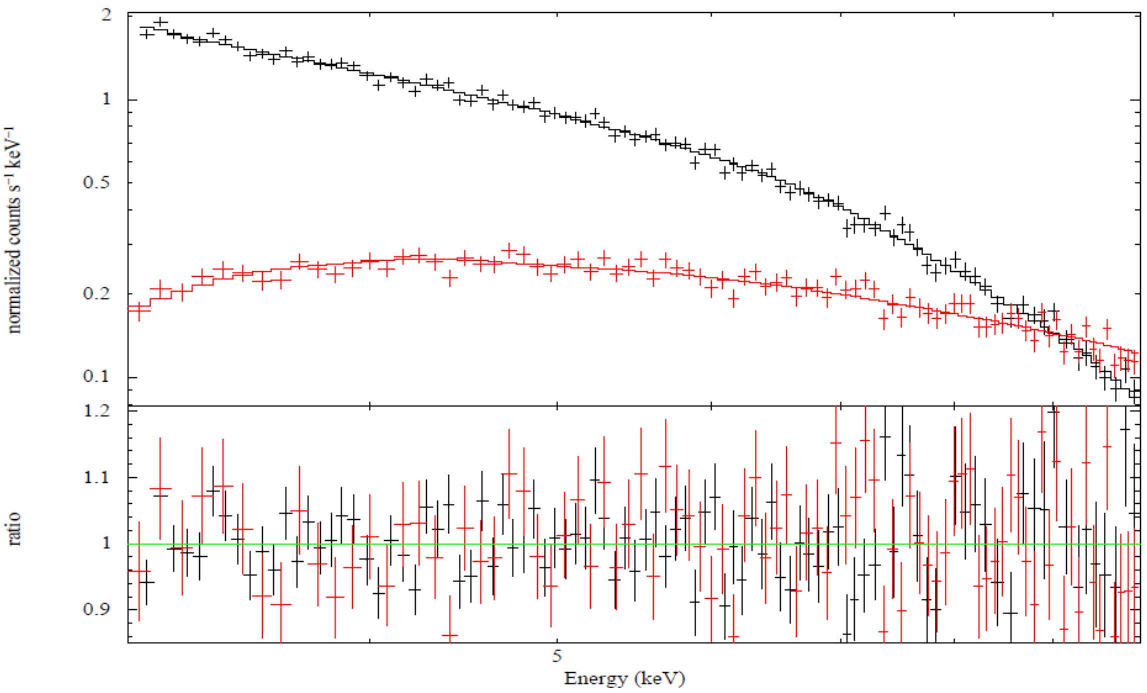

Figure 4.6: Simultaneously fitted EPIC (black) and FPMA (red) spectra of 3C 273. In the lower window the ratio values for model vs. data are given for both fits.

4.3.2.2 Method 2: Simultaneous fitting

Simultaneous fitting in the common energy band can be used to compare different instruments directly. An approach can be adding a cross-normalisation constant to the model, which depicts the difference in flux normalisation. The other way is to compare the photon indices, Γ (the value of the power-law slope), for fitting the same model simultaneously to both spectra and allow only this parameter to vary.
All observations used for this method can be found in the column *Method* of Table 4.1. All fits were done from 3 to 10 keV simultaneously for two detectors each (EPIC-pn & FPMA, EPIC-pn & FPMB) per source. We also fitted the spectra from both FPM detectors simultaneously to check whether there are significant discrepancies between them.
The models used for the sources are shown in Table 4.3. They do not differ much from the models from method 1, but some are kept simpler, because executing the fit in a smaller energy range did not require a blackbody anymore to describe the soft excess which is present below 2 keV. Two example spectra for simultaneous fits are shown in Fig. 4.6 (3C 273) and Fig. 4.7 (MCG–6 – 30 – 15).

The first task is to compare the flux normalisations by using a cross-normalisation constant. A source specific model was fitted to the EPIC-pn spectrum while keeping the same parameters for the FPM spectra (similar to Method 1). In addition to the models shown in Table 4.3 a constant, c, was added and set to 1 for the EPIC-pn spectra, but kept free for the FPM spectra. This cross-normalisation constant represents the difference in the flux normalisations of both instruments. The mean value for this constant is given in Table 4.4). The error was derived through error propagation of the uncertainties determined in the fit. The mean value is fairly close to 1, but a look at the distributions for both FPM detectors (see Fig. 4.8a and Fig. 4.8b) reveals some scattering around the mean value. A difference between the FPM detectors is

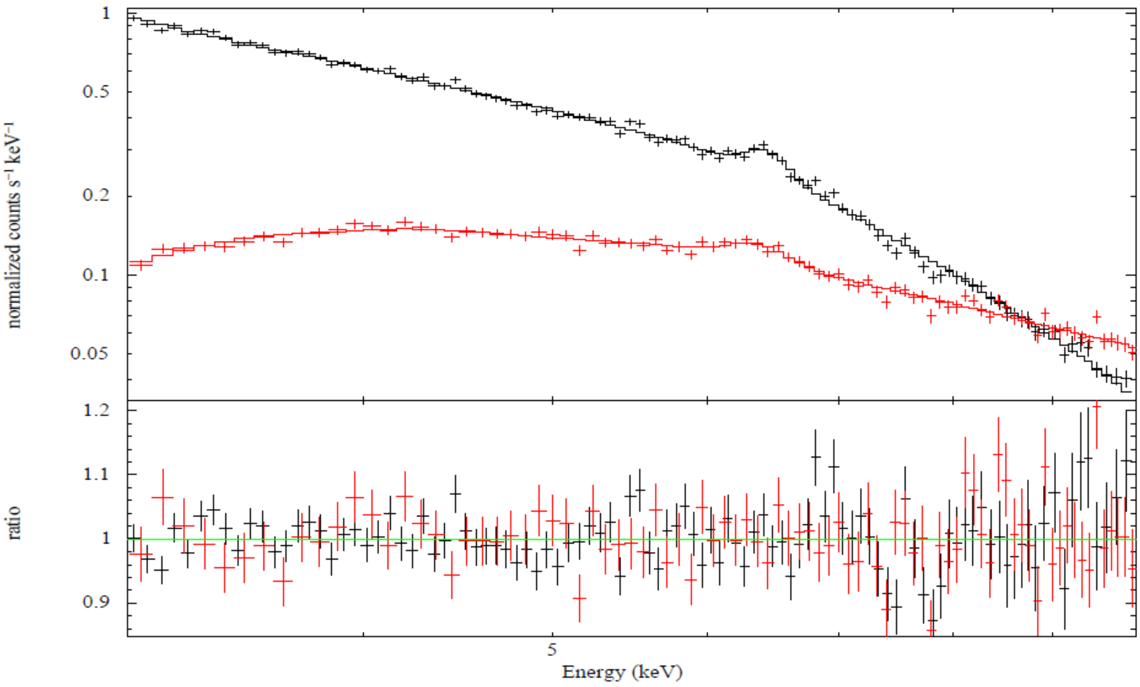

Figure 4.7: Simultaneously fitted EPIC (black) and FPMA (red) spectra of MCG−6 − 30 − 15. In the lower window the ratio values for model vs. data are given for both fits.

Source	Model	Reference
3C 120	tbnew_feo×(relxill+zgauss+zgauss)	Lohfink et al. (2013)
3C 273	tbnew_feo×pegpwrlw	Stuhlinger et al. (2004)
Ark 120	tbnew_feo×(relxill+zgauss+zgauss)	Matt et al. (2014)
Centaurus A	tbnew_feo×(pegpwrlw+zgauss)	Fürst et al. (2016)
Fairall 9	relxill+zgauss	Lohfink et al., 2012
HE 1136-2304	tbnew_feo×(relxill+zgauss)	Parker et al. (2016)
MCG-6-30-15	tbnew_feo×(relxill+zgauss)	Wilms et al. (2001)
Mrk 915	warmabs×tbnew_feo×(relxill+zgauss)	Severgnini et al. (2015)
NGC 4593	tbnew_feo×(pegpwrlw+zgauss)	Brenneman et al. (2007)
Swift J2127.4+5654	tbnew_feo×(relxill+zgauss)	Marinucci et al. (2014)

Table 4.3: Models applied on EPIC-pn and FPM spectra in Method 2

	c
EPIC-pn/FPMA	1.004 ± 0.034
EPIC-pn/FPMB	1.041 ± 0.034
FPMA/FPMB	1.034 ± 0.019

Table 4.4: Cross-normalisation constants, c, for FPMA and FPMB.

detectable.

Apart from three observations all derived constants lie within the 90% error region for both FPM detectors. The three exceptions are observation 11, 13 and 14 which belong to Centaurus A, Mrk 915 and HE1136-2304 respectively. While obs. 14 is inside the error region accounting its errors, obs. 11 and 13 are definitely off. In the case of Centaurus A, being a close and bright

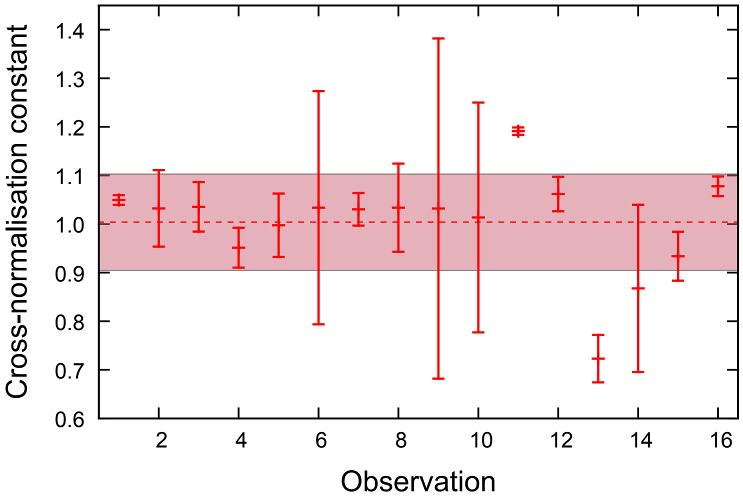

(a) Constants for FPMA.

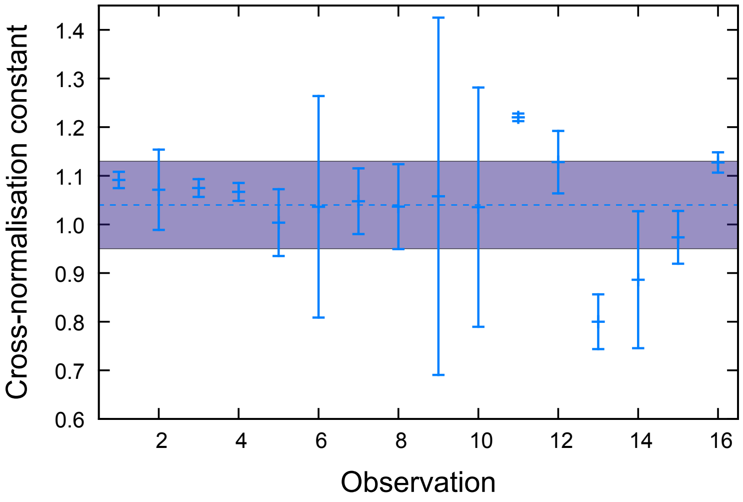

(b) Constants for FPMB.

Figure 4.8: Cross-normalisation constant distributions of FPMA and FPMB for all observations. The dashed line marks the mean value and the 90% error region is coloured.

	c
EPIC-pn/FPMA	1.020 ± 0.017
EPIC-pn/FPMB	1.062 ± 0.018

Table 4.5: Cross-normalisation constants, c, for reduced sample.

source, this offset can be explained with pile up effects being present even though we tried avoiding those in the extraction by excluding the innermost region of the source. For Mrk 915 we have no explanation for the low cross-normalisation in this source. Additionally, observation 6, 9 and 10 have large errors exceeding the 1σ region which makes those results less trustworthy. Excluding these observations (6, 9, 10, 11, 13 and 14), we get larger cross-normalisation constants (see Table 4.5).

Another task was comparing the photon indices for different sources in order to test the

	$\Delta\Gamma$
EPIC-pn-FPMA	0.142 ± 0.025
EPIC-pn-FPMB	0.133 ± 0.025
FPMA-FPMB	0.027 ± 0.004

Table 4.6: Mean values for $\Delta\Gamma$.

	x_0	σ
EPIC-pn/FPMA	0.128 ± 0.006	0.046 ± 0.012
EPIC-pn/FPMB	0.136 ± 0.060	0.112 ± 0.196

Table 4.7: Parameters for a Gaussian fit to the distribution of $\Delta\Gamma$ in a histogram. Note that here, the error σ is just 68% confidence.

calibration of both instruments. For an ideal cross-calibration between both satellites, those values should be the same. In Fig. 4.9 a direct comparison of the photon indices Γ for *XMM-Newton* and *NuSTAR* is shown. We observe a general offset which shows that the FPMA/FPMB spectra have steeper power law slopes than spectra from EPIC-pn. This seems to be present in all observations. In a more direct comparison, Fig. 4.10 presents $\Delta\Gamma$ from 14 observations of 8 sources over flux, showing there is no correlation with flux and therefore no pile-up effects present. The mean differences for EPIC-pn-FPMA, EPIC-pn-FPMB and FPMA-FPMB are shown in Table 4.6. The observation from Centaurus A was excluded from this sample, because it shows a much higher discrepancy between the slopes in *XMM-Newton* and *NuSTAR* data which might be due to pile up. Note that $\Delta\Gamma$ is much smaller for the comparison between both FPM detectors than between the two satellites.

Another way to look at the results is via a distribution in a histogram. The difference $\Delta\Gamma$ is shown for all 16 observations in Fig. 4.11a and Fig. 4.12a. For both histograms we used a bin size of $\Delta\Gamma = 0.01$ in order to get a clearer overview of the distribution. Since the value at $\Delta\Gamma = 0.4$ (from spectra of Centaurus A) is clearly aside the other results and was already excluded in the calculation of the mean $\Delta\Gamma$ (see Table 4.6), we ignored it. Figure 4.11b shows the remaining columns. In order to look at the normal distribution fitted to that data, we excluded also the two observations which had $\Delta\Gamma > 0.2$ (Mrk 915 and NGC 4593). The remaining data was fitted by a normal distribution of $f(x) = A \cdot \exp(-((x - x_0)/\sigma)^2)$. The same was done for the FPMB detector (see Fig. 4.12). Values with $\Delta\Gamma > 0.2$ were excluded again, which concerned again the observation of Centaurus A.

The parameters x_0 and σ of the Gaussian fit are shown in Table 4.7 for both histograms. Note that here, σ is only a 68% confidence error. While the fit delivers good results for the comparison of EPIC-pn and FPMA, it is more problematic in case of the EPIC-pn-FPMB comparison. There the uncertainties on both parameters are too large to give reasonable constraints, because the values are more spread than in the comparison with FPMA. Over all we find very similar results for the histogram approach as in Table 4.6. The difference of the photon index Γ between the EPIC-pn and FPM spectra indicates a principal, energy dependent mis-calibration in either, or in both of the two instruments.

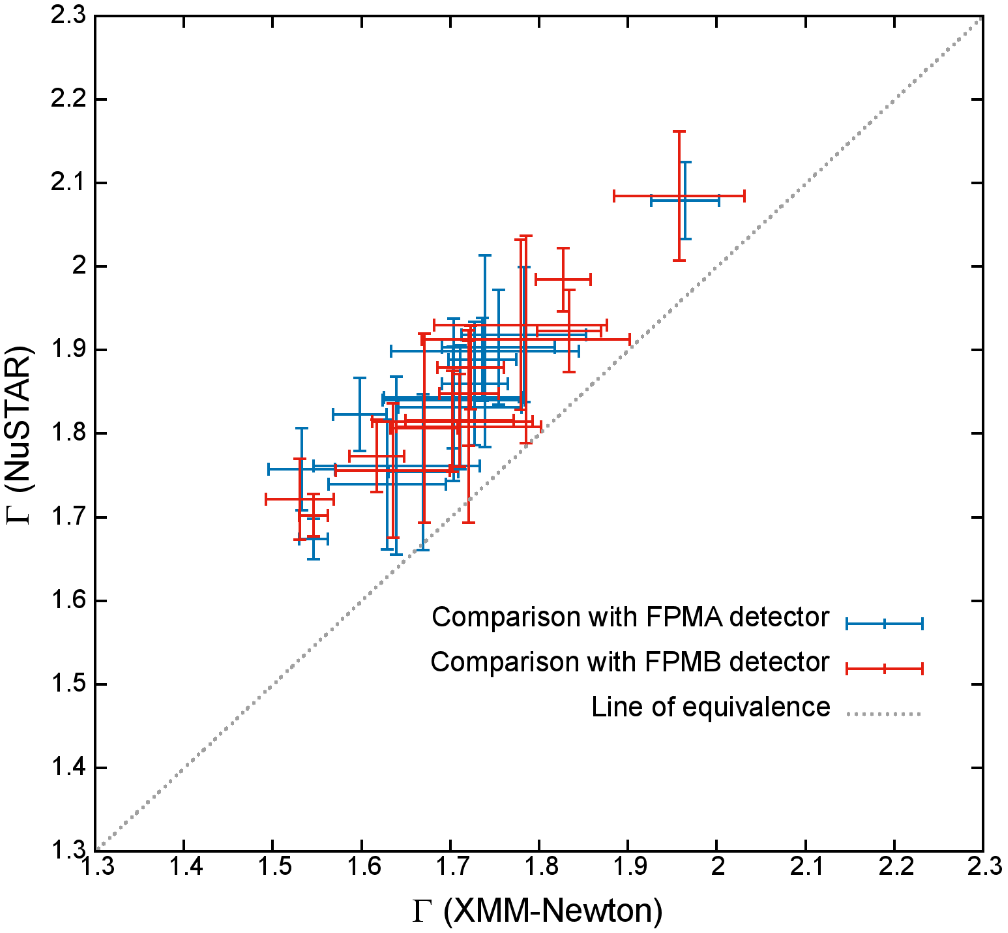

Figure 4.9: Direct comparison of photon indices Γ for *XMM-Newton* and *NuSTAR*. The ideal case would be that the data points are on the line of equivalence which is not observed.

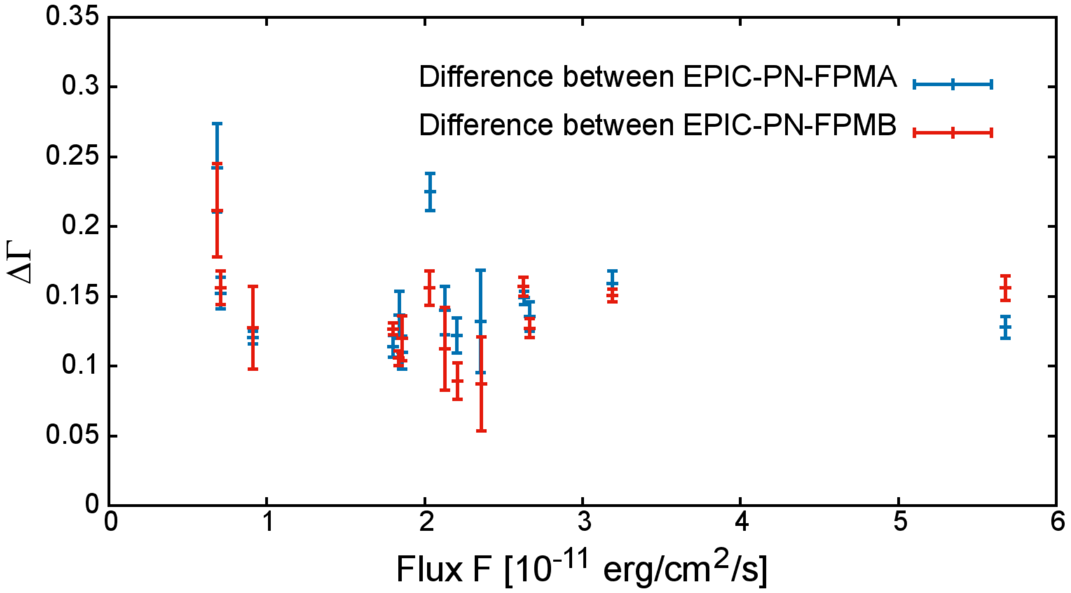

Figure 4.10: Individual ΔΓ over flux of source.

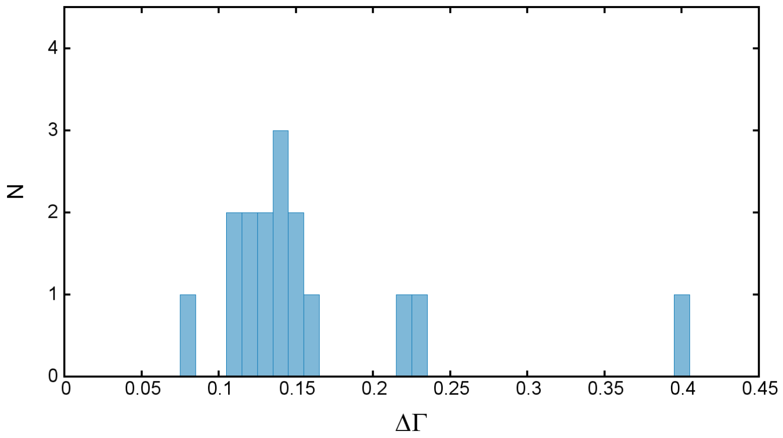

(a) Whole distribution of $\Delta\Gamma$

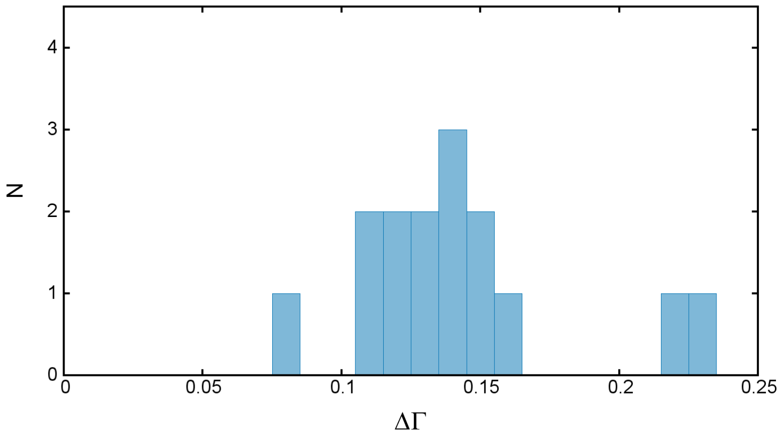

(b) Distribution of $\Delta\Gamma$ without Centaurus A

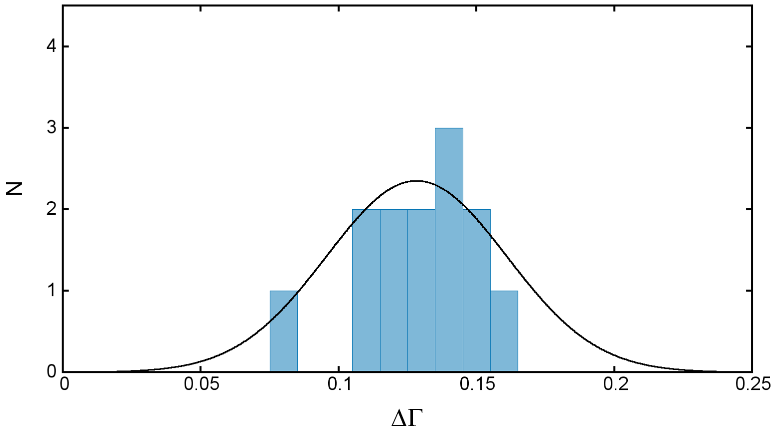

(c) Fitted gaussian curve over final distribuion (without Cen A, Mrk 915 and NGC 4593)

Figure 4.11: Distribution of $\Delta\Gamma$ for the FPMA detector

4.4 Comparison with other studies

So far only one cross-calibration analysis between *XMM-Newton* and *NuSTAR* was published (Madsen et al., 2017a). They performed a full analysis of the cross-normalisation constants between the satellites *Chandra*, *NuSTAR*, *Swift*, *Suzaku*, and *XMM-Newton* for 3C 273 and

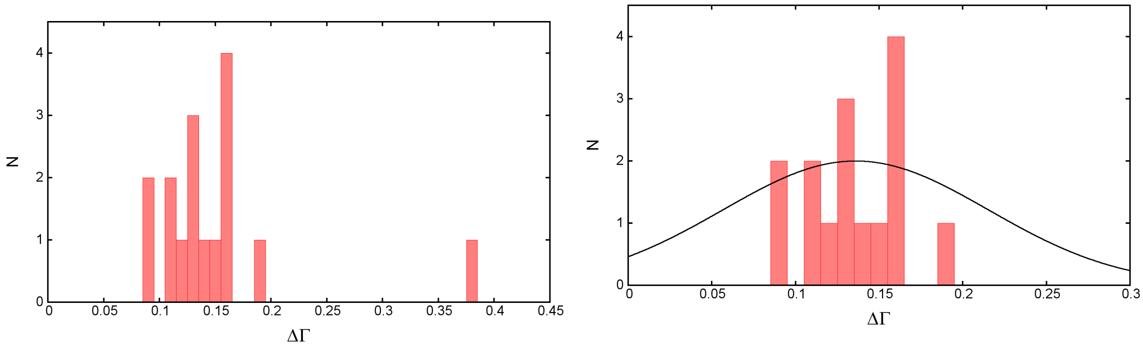

(a) Whole distribution of ΔΓ

(b) Fitted gaussian curve over final distribution (without Cen A)

Figure 4.12: Distribution of ΔΓ for the FPMB detector

Parameter	Instruments	This work	Madsen et al. (2017a)[2]
c	EPIC-pn/FPMA	1.05 ± 0.01	1.11 ± 0.03
	EPIC-pn/FPMB	1.09 ± 0.02	1.16 ± 0.02
$\Delta\Gamma$	EPIC-pn/FPMA	0.13 ± 0.03	0.10 ± 0.09
	EPIC-pn/FPMB	0.16 ± 0.03	0.01 ± 0.09

Table 4.8: Comparison of c and $\Delta\Gamma$ with Madsen et al. for 3C 273.

PKS 2155-304. Since 3C 273 was in the sample that we analysed, we can compare their and our results directly. They used a simple power-law and `tbabs` for absorption, very similar to our model for 3C 273 (see Table 4.3). However, they used a fitting range from 3 to 7 keV, while we used all data between 3 and 10 keV. Another difference lies in the data extraction for which we used SAS version 15.0.0 and Madsen et al. SAS version 14.0.0. The values of c and $\Delta\Gamma$ are given in Table 4.8. Although they did not include a power-law index comparison in the paper, they showed the values for Γ, being derived in individual fits, which we used for calculating the correspondent $\Delta\Gamma$. While the difference in the power-law slope matches for the FPMA detector, there is nearly no difference between the FPMB detector and EPIC-pn according to Madsen et al. (2017a). Additionally the cross-normalisation constants between the EPIC-pn and the FPM detectors found by Madsen et al. (2017a) are much larger than the values found in this work.

4.5 Outlook

Further studies are necessary for the progress of improving the cross-calibration between *XMM-Newton* and *NuSTAR*, since we could see that there can be quite different results even for the same source. The difference of $\Delta\Gamma \propto 0.1$ in the power-law slopes is found to be consistent over all the sources and observations, regardless of the model. An explanation can be a principal, energy dependent mis-calibration in either one or both of the instruments.

The cross-normalisation constant c reveals differences in the flux normalisations of both satellites and shows some variations for which the origin has yet to be determined.

Recently there was an observation of the Crab nebula by *NuSTAR* without its mirrors (Madsen et al., 2017b). They find the true intrinsic flux to be 12% higher than the flux measured in an observation that includes the *NuSTAR* optics. Observing the stray light from the Crab allowed

---

[2] Since c and $\Delta\Gamma$ were not given directly in the paper, we calculated c from the flux values and $\Delta\Gamma$ from the given power-law slopes.

Madsen et al. (2017b) to measure new detector absorption parameters, which resulted in an update of the detector absorption files in CALDB20160606.
The surveys of AGN and other astrophysical sources depend on the cooperation of different satellites, because radiation processes, e.g., synchrotron radiation, exist in broad spectral ranges, which can only be studied by many different instruments working together.

Chapter 5

Summary

In this Master's thesis I worked on two different projects both related to AGN.
First, I studied the derivation of equations describing synchrotron radiation. This non-thermal radiation process explains the emission originating from jets in the radio band. In order to gain a full self-absorbed spectrum, we needed to derive the emission and absorption coefficient and insert these in the radiative transfer equation. As integrals over Bessel functions are involved, one can solve the equation via numeric integrators or by using analytic approximations. The latter case is only possible for certain electron distributions. For electrons following an energy dependent power-law distribution, an analytic approximation is possible and was compared to the numeric result. However, there is an offset present, whose origin is possibly a numeric problem, but has yet to be determined.
Other numeric problems did occur, which were mostly due to the integration over several magnitudes in frequency ν. Comparing my results with equations from other papers or books, I found that, although they do not the same at first sight, they are all in agreement, except for the emission coefficient, where they differ in a factor of 1/2.
The second part of this thesis is a systematic study of simultaneous observations performed by the two X-ray satellites *XMM-Newton* and *NuSTAR*. The main advantage of simultaneous observations by these two spacecrafts is their overlap in the energy band from 3 to 12 keV, which allows to compare the calibration of both on-board instruments directly.
I used two methods to gain insights in the calibration differences, while the data I analysed came from AGN observations only. First, I compared the data of *NuSTAR*'s FPM detectors with the physical model, fitted to data from *XMM-Newton*'s EPIC-pn detector. The ratio values of this comparison revealed an energy dependent slope in the FPM spectra.
Then, in a more elaborate approach, I fitted simultaneously obtained spectra using physical models in the overlapping energy band from 3 to 10 keV and compared the flux normalisations of both instruments. I found the flux detected by EPIC-pn to be generally higher in comparison to the FPM detectors. Additionally, I compared the difference in the power-law slope parameter Γ and found the spectra obtained by *NuSTAR* to be generally steeper, indicating an energy dependent mis-calibration in one or both instruments.
Last, I compared my results with another paper, which treats a source also included in my AGN sample, and could establish a general agreement. Differences in the determined values might be due to slightly different models, a different energy range for the simultaneous fits, or a newer version of the data extraction software in my case.

Bibliography

Aartsen, M. G., Abbasi, R., Abdou, Y., et al. 2013, Physical Review Letters, 111, 021103

Abdo, A. A., Ackermann, M., Ajello, M., et al. 2011, ApJ, 736, 131

Antonucci, R. 1993, ARA&A, 31, 473

Antonucci, R. R. J. 1984, ApJ, 281, 112

Antonucci, R. R. J. & Miller, J. S. 1985, ApJ, 297, 621

Baade, W. & Minkowski, R. 1954, ApJ, 119, 206

Balbus, S. A. & Hawley, J. F. 1991, ApJ, 376, 214

Baldwin, J. A., Ferland, G. J., Korista, K. T., Hamann, F., & Dietrich, M. 2003, ApJ, 582, 590

Barthel, P. 1989a, Scientific American, 260, 20

Barthel, P. D. 1989b, ApJ, 336, 606

Beckmann, V. & Shrader, C. 2012, Active Galactic Nuclei (Wiley-VCH Verlag GmbH and Co. KGaA)

Bendo, G. J. & Joseph, R. D. 2004, AJ, 127, 3338

Bennett, A. S. 1962, MemRAS, 68, 163

Blandford, R. D. & Payne, D. G. 1982, MNRAS, 199, 883

Blandford, R. D. & Znajek, R. L. 1977, MNRAS, 179, 433

Blumenthal, G. R. & Gould, R. J. 1970, Reviews of Modern Physics, 42, 237

Bolton, J. G., Gardner, F. F., & Mackey, M. B. 1964, Australian Journal of Physics, 17, 340

Böttcher, M., Reimer, A., Sweeney, K., & Prakash, A. 2013, ApJ, 768, 54

Brenneman, L. W., Reynolds, C. S., Wilms, J., & Kaiser, M. E. 2007, ApJ, 666, 817

Bridle, A. H., Hough, D. H., Lonsdale, C. J., Burns, J. O., & Laing, R. A. 1994, AJ, 108, 766

Brinkmann, W., Siebert, J., Kollgaard, R. I., & Thomas, H.-C. 1996, A&A, 313, 356

Celotti, A., Padovani, P., & Ghisellini, G. 1997, MNRAS, 286, 415

Cohen, M. H., Cannon, W., Purcell, G. H., et al. 1971, ApJ, 170, 207

Corbin, M. R. 1995, ApJ, 447, 496

Curtis, H. D. 1918, Publications of Lick Observatory, 13, 9

Davidson, K. & Netzer, H. 1979, Reviews of Modern Physics, 51, 715

Day, G. A., Shimmins, A. J., Ekers, R. D., & Cole, D. J. 1966, Australian Journal of Physics, 19, 35

Dermer, C. D., Schlickeiser, R., & Mastichiadis, A. 1992, A&A, 256, L27

Doeleman, S. S., Fish, V. L., Schenck, D. E., et al. 2012, Science, 338, 355

Edge, D. O., Shakeshaft, J. R., McAdam, W. B., Baldwin, J. E., & Archer, S. 1959, MemRAS, 68, 37

Fanaroff, B. L. & Riley, J. M. 1974, MNRAS, 167, 31P

Fath, E. A. 1909, Lick Observatory Bulletin, 5, 71

Fürst, F., Müller, C., Madsen, K. K., et al. 2016, ApJ, 819, 150

García, J., Dauser, T., Lohfink, A., et al. 2014, ApJ, 782, 76

Ghisellini, G., Della Ceca, R., Volonteri, M., et al. 2010, MNRAS, 405, 387

Ghisellini, G. & Madau, P. 1996, MNRAS, 280, 67

Ghisellini, G., Maraschi, L., & Treves, A. 1985, A&A, 146, 204

Harrison, F. A., Craig, W. W., Christensen, F. E., et al. 2013, ApJ, 770, 103

Heckman, T. M. 1980, A&A, 87, 152

Ho, L. C., Filippenko, A. V., & Sargent, W. L. W. 1993, ApJ, 417, 63

Ho, L. C., Filippenko, A. V., & Sargent, W. L. W. 1997, ApJ, 487, 568

Hoffmeister, C. 1929, Astronomische Nachrichten, 236, 233

Hogg, D. E., MacDonald, G. H., Conway, R. G., & Wade, C. M. 1969, AJ, 74, 1206

Hoyle, F. & Fowler, W. A. 1963, MNRAS, 125, 169

Hubble, E. P. 1926, ApJ, 64

Jansen, F., Lumb, D., Altieri, B., et al. 2001, A&A, 365, L1

Kellermann, K. I., Condon, J. J., Kimball, A. E., Perley, R. A., & Željko Ivezić. 2016, The Astrophysical Journal, 831, 168

Kellermann, K. I., Sramek, R., Schmidt, M., Shaffer, D. B., & Green, R. 1989, AJ, 98, 1195

Kerr, R. P. 1963, Physical Review Letters, 11, 237

Khachikian, E. Y. & Weedman, D. W. 1974, ApJ, 192, 581

Kigure, H. & Shibata, K. 2005, ApJ, 634, 879

Krauß, F., Kadler, M., Mannheim, K., et al. 2014, A&A, 566, L7

Krauß, F., Wang, B., Baxter, C., et al. 2015, ArXiv e-prints

Krauß, F., Wilms, J., Kadler, M., et al. 2016, A&A, 591, A130

Laing, R. A. & Bridle, A. H. 1987, MNRAS, 228, 557

Lang, K. R. 1999, Astrophysical Formulae, Vol. 1 (Springer Verlag)

Lasota, J.-P., Abramowicz, M. A., Chen, X., et al. 1996, ApJ, 462, 142

Leavitt, H. S. & Pickering, E. C. 1912, HCOC, 173, 1

Lohfink, A. M., Reynolds, C. S., Jorstad, S. G., et al. 2013, ApJ, 772, 83

Lohfink, A. M., Reynolds, C. S., Miller, J. M., et al. 2012, ApJ, 758, 67

Lucchini, M., Tavecchio, F., & Ghisellini, G. 2017, MNRAS, 466, 4299

Madsen, K. K., Beardmore, A. P., Forster, K., et al. 2017a, AJ, 153, 2

Madsen, K. K., Forster, K., Grefenstette, B. W., Harrison, F. A., & Stern, D. 2017b, ApJ, 841, 56

Madsen, K. K., Fürst, F., Walton, D. J., et al. 2015, ApJ, 812, 14

Mannheim, K. 1993a, PhRvD, 48, 2408

Mannheim, K. 1993b, A&A, 269, 67

Mannheim, K. 1995, Astroparticle Physics, 3, 295

Mannheim, K. & Biermann, P. L. 1989, A&A, 221, 211

Mannheim, K. & Biermann, P. L. 1992, A&A, 253, L21

Maraschi, L., Ghisellini, G., & Celotti, A. 1992, ApJL, 397, L5

Marinucci, A., Matt, G., Kara, E., et al. 2014, MNRAS, 440, 2347

Martí-Vidal, I., Muller, S., Vlemmings, W., Horellou, C., & Aalto, S. 2015, Science, 348, 311

Matt, G., Marinucci, A., Guainazzi, M., et al. 2014, MNRAS, 439, 3016

Matthews, T. A. & Sandage, A. R. 1963, ApJ, 138, 30

McKinney, J. C. 2006, MNRAS, 368, 1561

McKinney, J. C., Tchekhovskoy, A., Sadowski, A., & Narayan, R. 2014, MNRAS, 441, 3177

Mortlock, D., Warren, S., Patel, M., et al. 2011, in Galaxy Formation, 88

Osterbrock, D. E. 1989, Astrophysics of gaseous nebulae and active galactic nuclei

Osterbrock, D. E. & Koski, A. T. 1976, MNRAS, 176, 61P

Osterbrock, D. E. & Martel, A. 1993, ApJ, 414, 552

Pacholczyk, A. G. 1970, Radio Astrophysics (W. H. Freeman and Company)

Padmanabhan, T. 2000, Theoretical Astrophysics, Vol. 1 (Cambridge University Press)

Parker, M. L., Komossa, S., Kollatschny, W., et al. 2016, MNRAS, 461, 1927

Penrose, R. 1969, Nuovo Cimento Rivista Serie, 1

Price, R. M. & Milne, D. K. 1965, Australian Journal of Physics, 18, 329

Pringle, J. E. 1981, ARA&A, 19, 137

Richards, G. T., Strauss, M. A., Fan, X., et al. 2006, AJ, 131, 2766

Rybicki, G. B. & Lightman, A. P. 1979, Radiative Processes in Astrophysics (John Wiley and Sons, Inc.)

Salpeter, E. E. 1964, ApJ, 140, 796

Scarpa, R. & Falomo, R. 1997, A&A, 325, 109

Scheuer, P. A. G. & Readhead, A. C. S. 1979, Nature, 277, 182

Schmidt, M. 1963, Nature, 197, 1040

Severgnini, P., Ballo, L., Braito, V., et al. 2015, MNRAS, 453, 3611

Seyfert, C. K. 1943, ApJ, 97, 28

Shakura, N. I. & Sunyaev, R. A. 1973, A&A, 24, 337

Shields, J. C. 1992, ApJL, 399, L27

Sikora, M., Begelman, M. C., & Rees, M. J. 1994, ApJ, 421, 153

Smith, M. G. 1975, ApJ, 202, 591

Smith, P. S., Schmidt, G. D., Jannuzi, B. T., & Elston, R. 1994, ApJ, 426, 535

Stuhlinger, M., Staubert, R., Wilms, J., Kreykenbohm, I., & Benlloch-García, S. 2004, MemSAI, 75, 527

Tavecchio, F., Maraschi, L., Sambruna, R. M., & Urry, C. M. 2000, ApJL, 544, L23

Terlevich, R. & Melnick, J. 1985, MNRAS, 213, 841

Ulrich, M.-H., Maraschi, L., & Urry, C. M. 1997, ARA&A, 35, 445

Urry, C. M. & Padovani, P. 1995, PASP, 107, 803

Vanden Berk, D. E., Richards, G. T., Bauer, A., et al. 2001, AJ, 122, 549

Verner, D. A., Ferland, G. J., Korista, K. T., & Yakovlev, D. G. 1996, ApJ, 465, 487

Weedman, D. W. 1977, ARA&A, 15, 69

Westfold, K. C. 1959, ApJ, 130, 241

Whitney, A. R., Shapiro, I. I., Rogers, A. E. E., et al. 1971, Science, 173, 225

Wilms, J., Allen, A., & McCray, R. 2000, ApJ, 542, 914

Wilms, J. & Kreykenbohm, I. 2015, Active Galactic Nuclei, Lecture, Lecture notes available at http://hydrus.sternwarte.uni-erlangen.de/~wilms/teach/agn1516/chapter0001.html

Wilms, J., Reynolds, C. S., Begelman, M. C., et al. 2001, MNRAS, 328, L27

Woltjer, L. 1959, ApJ, 130, 38

York, D. G., Adelman, J., Anderson, Jr., J. E., et al. 2000, AJ, 120, 1579

Zamorani, G., Henry, J. P., Maccacaro, T., et al. 1981, ApJ, 245, 357

Zel'dovich, Y. B. & Novikov, I. D. 1964, Soviet Physics Doklady, 9, 246

Acknowledgements

First and foremost I want to thank my supervisor Prof. Dr. Joern Wilms for his support, encouragement and advice. I am very grateful for the opportunity to attend the AGN conference 2016 at Garching, the IBWS conference 2017 at Karlsbad and Prof. Wilms' support for my traineeship at ESAC, whose project became part of this thesis.

I deeply want to thank Norbert Schartel and Maria Santos-Lleo for the wonderful and interesting time I had while working at ESAC. In addition, I want to thank all the trainees, who made the five months in Madrid so much fun, especially Alessandra, Kjell, Harry, Aleksi and Vedad.

Then, of course, I am very grateful to be part of the Remeis community, without which the Remeis observatory would not be such a welcoming and pleasent working place. Sincere thanks are given to all the Remeisen. I want to thank Matthias Kühnel and Ralf Ballhausen for their help with the *NuSTAR* data extraction and give a big thank you to Thomas Dauser, Sebastian Falkner and Javier García for their help during the preparation of my first conference talk. At this point I also want thank my office mates for hilarious conversations and apologise for my over-use of the word "Bieberkacke". I am looking forward to many years more of Remeis skiing and overturning during the annual canoeing, as well as (spontaneous) barbecues and pool parties.

Somehow, public outreach became important to me during the last year, probably also because of Simon Kreuzer. I am very grateful that he suggested to give a lecture about multiwavelength astronomy together at a "Schülerakademie", because it was a great experience and a lot of fun.

A big thank you to Basti, Tommy and Tobi for improving my thesis through helpful comments and fancy plot ideas.

Last but not least I want to thank my family and friends for their support.

This thesis has made use of ISIS functions (ISISscripts) provided by ECAP/Remeis observatory and MIT (http://www.sternwarte.uni-erlangen.de/isis/). In this thesis I use observations obtained with XMM-Newton, an ESA science mission with instruments and contributions directly funded by ESA Member States and the USA, NASA, as well as data from the NuSTAR mission, a project led by the California Institute of Technology, managed by the Jet Propulsion Laboratory, and funded by NASA. This work has made use of the NuSTAR Data Analysis Software (NuSTARDAS) jointly developed by the ASI Science Data Center and the California Institute of Technology.

Erklärung

Hiermit bestätige ich, dass ich diese Arbeit selbstständig und nur unter Verwendung der angegebenen Hilfsmittel angefertigt habe.

Bamberg, den 22.09.2017

Andrea Gokus